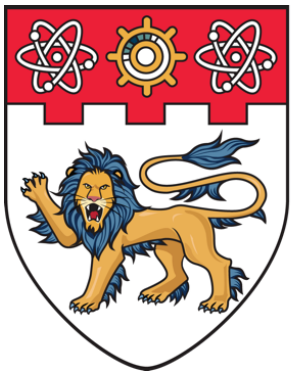

NANYANG TECHNOLOGICAL UNIVERSITY
SINGAPORE

OPTICAL STUDY OF EXCITONIC COMPLEXES IN TRANSITION METAL DICHALCOGENIDES MONOLAYERS

DI BAO

SCHOOL OF PHYSICAL AND MATHEMATICAL SCIENCES

2020

OPTICAL STUDY OF EXCITONIC COMPLEXES IN TRANSITION METAL DICHALCOGENIDES MONOLAYERS

DI BAO

SCHOOL OF PHYSICAL AND MATHEMATICAL SCIENCES

A thesis submitted to the Nanyang Technological University in partial fulfilment of the requirement for the degree of Doctor of Philosophy

2020

Statement of Originality

I hereby certify that the work embodied in this thesis is the result of original research done by me except where otherwise stated in this thesis. The thesis work has not been submitted for a degree or professional qualification to any other university or institution. I declare that this thesis is written by myself and is free of plagiarism and of sufficient grammatical clarity to be examined. I confirm that the investigations were conducted in accord with the ethics policies and integrity standards of Nanyang Technological University and that the research data are presented honestly and without prejudice.

05/08/2020

. . . . . .
Date

. . . . . .
DI BAO

Supervisor Declaration Statement

I have reviewed the content and presentation style of this thesis and declare it of sufficient grammatical clarity to be examined. To the best of my knowledge, the thesis is free of plagiarism and the research and writing are those of the candidate's except as acknowledged in the Author Attribution Statement. I confirm that the investigations were conducted in accord with the ethics policies and integrity standards of Nanyang Technological University and that the research data are presented honestly and without prejudice.

05/08/2020

. . . . . .

Date

. . . . . .

Qihua Xiong

Authorship Attribution Statement

This thesis contains material from 1 paper published in the following peer-reviewed journal(s) / from papers accepted at conferences in which I am listed as an author.

Chapter 4 is published as Di Bao, Andrés Granados del Águila, T. Thu Ha Do, Sheng Liu, Jiajie Pei and Qihua Xiong. Probing momentum-indirect excitons by near-resonance photoluminescence excitation spectroscopy in WS_2 monolayer. *2D Materials* **7**, 031002 (2020). DOI: 10.1088/2053-1583/ab817a

The contributions of the co-authors are as follows:

- Prof. Qihua Xiong and Dr. Andrés Granados del Águila started the project, conceived and designed the experiments.
- Sheng Liu prepared the TMD micro-sized semiconductor layers.
- Dr. Andrés Granados del Águila and I performed the optical measurements at the School of Physical and Mathematical Sciences.
- Dr. Andrés Granados del Águila and I analyzed, interpreted the data and wrote the manuscript. Dr. T. Thu Ha Do and Dr. Jiajie Pei intensively discussed on the data and the manuscript.

05/08/2020

Bao Di

. . . . . .

Date

. . . . . .

DI BAO

Abstract

Transition metal dichalcogenides (TMDs) monolayers such as MX_2 (M = Mo, W; X = S, Se) feature strong exciton properties and spin-valley physics. As a result of strong quantum- and dielectric confinement in single atomic layer of TMD materials, the photoexcited electrons and holes are tightly bound via Coulomb interaction to form excitonic complexes such as charged excitons (trions), biexcitons that offer great opportunities to study many-body physics. However, the distinct electronic band structure and possible many-particle components lead to complicated excitonic features especially in the photoluminescence spectra of W-based monolayers. Their possible origins and compositions need to be further explored.

In this thesis, we investigate the excitonic structures of TMDs monolayers via optical spectroscopy. With near-resonance photoluminescence excitation spectroscopy, multiple scattering processes between excitons and phonons carrying non-zero wavevector are revealed, indicating the presence of indirect excitons whose constituent electrons and holes locate at different valleys. The momentum-indirect transition in WS_2 monolayers matches the energies of lower energy features in the PL spectrum, suggesting their possible origin from the recombination of electrons and holes in different valleys. Such transitions require additional electrons in order to conserve momentum, which could be provided by free electrons via the formation of charge states. The encapsulation of WS_2 monolayer with hexagonal boron nitride (hBN) greatly reduces the PL linewidth and enables the observation of fine structures of the lower-energy features. By electrostatic doping to the hBN-encapsulated WS_2 monolayer, we observe a Fermi edge singularity-like transition in the reflectance and PL spectra, reflecting distinct interactions between excitons and Fermi electrons under different electron densities. The Fermi edge singularity may indicate a transition from a fermion-like charged state to a boson-like particle (exciton-plasmon).

Due to the inversion symmetry breaking, there are two energy-degenerate but inequivalent valleys (K and $K^{'}$). This degeneracy can be broken by applying a magnetic field, leading to a valley Zeeman splitting. The different energy splittings of the excitonic features in a magnetic field arise from several contributions, including spin magnetic moment, valley magnetic moment and atomic orbital magnetic moment. By examining the valley Zeeman splitting of different excitonic features of the hBN-encapsulated WS_2 and MoS_2 monolayers, information regarding the band configuration and valley magnetic

moment of the electrons and holes that form the excitonic states is revealed.

Our findings presented in this thesis gain critical insights into the excitonic structures and many-body physics, leading towards a complete understanding of optical and electronic properties of TMDs monolayers.

Acknowledgement

With the accomplishment of this thesis, my journey as a Ph.D. student will come to an end. The journey of my PhD research is full of difficulties, but finally I have become a better and stronger person. No matter good or bad experiences, they are the essential ingredients that help me grow. I would thank all the people who have provided their invaluable help along this journey.

First of all, I would like to sincerely thank my supervisor - Professor Qihua Xiong, who has taught me precious personal qualities. One of the most profound things I learn from him is that we should never be afraid of difficulties and should try the best to overcome them, by which means we can grow rapidly to become an excellent researcher. It requires courage and perseverance which I have improved a lot after four-years studies. I am also thankful for his encouragement to explore physics that I am interested in. Within Prof. Xiong's group, I have learned and managed to become an independent researcher.

Secondly, I would send my great appreciation to Dr. Andrés Granados del Águila, who has always motivated me in research and inspired me to be a great physicist. We have worked together throughout my Ph.D. time and he taught me a lot of details about optical setups and physical knowledge. Also, we have had lots of wonderful discussions, which were full of insights and imagination. I really enjoyed and learned a lot to work with him and appreciate him for being my good friend and colleague. I believe we will have more wonderful experiences in research and life in the future.

Next I would thank my colleague and friend Dr. Xue Liu. He has taught me a lot in sample fabrication and electrical measurements. We have had great collaborations and I will always admire his patience and kind personality. And I would also thank my colleague and friend Dr. Do Thi Thu Ha, who has helped me a lot in revising manuscripts and I learned a lot of writing skills from her.

I would also thank the current and previous group members including Dr. Cheefai Fong, Dr. Xingzhi Wang, Dr. Xin Lu, Dr. Sheng Liu, Dr. Jiajie Pei and so on, for their great help, training and suggestions during my Ph.D. period.

Last but not least, I would thank my parents, grandparents, and all the families for their long-term and unconditional support, and my lovely girlfriend for her accompanying when I was upset. Their care and love have always driven me forward in my life. This thesis is dedicated to them.

Table of Contents

List of Figures

List of Tables

Chapter 1

Introduction

1.1 Optical and Electronic Properties of Semiconductors

Crystalline solids feature periodic arrangements of atoms and could be divided into three categories: metal, semiconductor and insulator. Semiconductor and insulator distinguish themselves from metals by the existence of energy gaps or forbidden energy region in their electronic band structure. A lot of efforts have been devoted to studying semiconductors for their optoelectronic applications in modern information industry as well as many fundamental physical phenomena that are different from the cold atom system due to their unique band structures. Here we start with the general quantum mechanical description of the electronic band structure.

1.1.1 Electronic Band Structure

As crystalline solids, semiconductors have the most important symmetry that is the invariance under translations called translational symmetry. According to the Bloch's theorem, the wave functions of the electron states could be written as:

$$\psi_k(\boldsymbol{r}) = u_k(\boldsymbol{r})e^{(i\boldsymbol{k}\cdot\boldsymbol{r})}, \tag{1.1}$$

where $u_k(\boldsymbol{r})$ is the periodic function of the lattice, $e^{(i\boldsymbol{k}\cdot\boldsymbol{r})}$ denotes the plane-wave with wavevector $\boldsymbol{k}$ [1]. The motion of an electron is described by a time-dependent Schrödinger equation:

$$i\hbar\frac{\partial}{\partial t}\Psi(\boldsymbol{r},t) = \hat{H}\Psi(\boldsymbol{r},t), \tag{1.2}$$

where $\hbar$ is the reduced Planck constant. The Hamiltonian operator is composed of the kinetic energy and the potential energy $\hat{H} = \hat{\boldsymbol{p}}^2/2m + \hat{V}$, where m is the electron mass. By separating $\Psi(\boldsymbol{r},t)$ into the spatial and temporal parts $\Psi(\boldsymbol{r},t) = \psi(\boldsymbol{r})T(t)$, we can introduce Equation (1.1) into (1.2) and solve the equation independently, from which the

eigenvalue of energy $E(\boldsymbol{k})$ is obtained as a function of crystal plane-wave momentum k (that is the so-called electronic band structure). Due to the translational symmetry of the crystal, the Bloch function described by $\boldsymbol{k}$ can be extended to any wavevector $\boldsymbol{k} + n\boldsymbol{G}$, where n is an integer, $\boldsymbol{G}$ denotes the reciprocal lattice vector. To facilitate the discussion and minimize the calculation cost, people usually discuss the band structure within the first Brillouin zone.

In addition, differing from the free electrons in vacuum, the conduction and valence band electrons have different effective masses, resulting from the interaction between electrons and periodic lattice potential. Specifically, the effective masses of electrons can be associated with the conduction band and valence band dispersion near the extrema in a parabolic approximation by:

$$E_c(\boldsymbol{k}) = E_g + \frac{\hbar^2 \boldsymbol{k}^2}{2m_e^*}, \tag{1.3}$$

$$E_v(\boldsymbol{k}) = -\frac{\hbar^2 \boldsymbol{k}^2}{2m_h^*} \tag{1.4}$$

where E_g is the bandgap, m_e^* and m_h^* the effective masses of the electron and hole in the conduction band and valence bands [1]. From Equations (1.3) and (1.4), we can estimate the value of m_e^*/m_h^* by deducing the curvature of the band dispersion near the extrema, where normally critical points are located in the Brillouin zone.

1.1.2 Interband Absorption

As mentioned in the previous section, semiconductors have electronic band structures that are gapped by an energy E_g into two: conduction band and valence band. Without external excitations, all the electrons will occupy the valence band while the conduction band remains unoccupied. However, when an external excitation is applied, $e.g.$, light illumination with the photon energy larger than the bandgap ($\hbar\omega \geq E_g$), an electron in the valence band can absorb a photon and will be excited into the conduction band. This process is called interband absorption. Due to the small photon momentum, the band edge absorption is much more efficient in direct bandgap semiconductors, where the electron momentum almost does not change after being promoted to conduction band. However, for above-bandedge absorption, the transition requires the assistance of phonons (excitation of acoustic or optical phonons) to scatter the electron to its

dispersion of conduction band. As the opposite process, the electron in the conduction band decay via photon emission and return to the valence band, which is called interband luminescence.

For the direct absorption process near the band edge, the interband transition rate is calculated by Fermi's golden rule:

$$W_{i\to f} = \frac{2\pi}{\hbar}|M|^2 g(\hbar\omega), \tag{1.5}$$

where M is the transition matrix, $g(\hbar\omega)$ the density of states [1].

The transition matrix elements denote the effect of perturbation on the electrons due to light absorption, which reflect the oscillator strength of interband transition. It gives the probability of electrons that transit from initial state $|i\rangle$ to final state $\langle f|$ by:

$$M = \langle f|\, H'\, |i\rangle = \int \psi_f^*(\boldsymbol{r}) H'(\boldsymbol{r}) \psi_i(\boldsymbol{r}) d^3\boldsymbol{r}, \tag{1.6}$$

where H' is the Hamiltonian operator of light perturbation, $\boldsymbol{r}$ the electron position vector [1]. In a semi-classical approach, the interaction between the photons and the electrons is given by:

$$H' = -\boldsymbol{p}_e \cdot \boldsymbol{E}_{photon}, \tag{1.7}$$

where $\boldsymbol{p}_e$ denotes the electron dipole moment and equals to $-e\boldsymbol{f}$. The light wave is given by the form of plane waves:

$$\boldsymbol{E}_{photon}(\boldsymbol{r}) = \boldsymbol{E}_0 e^{i\boldsymbol{k}\cdot\boldsymbol{r}}, \tag{1.8}$$

then H' is thus:

$$H'(\boldsymbol{r}) = e\boldsymbol{E}_0 \cdot \boldsymbol{r} e^{i\boldsymbol{k}\cdot\boldsymbol{r}}. \tag{1.9}$$

According to Equation (1.1), the electron wave functions before and after photon absorption can be written as:

$$\psi_i(\boldsymbol{r}) = \frac{1}{\sqrt{V}} u_i(\boldsymbol{r}) e^{i\boldsymbol{k}_i\cdot\boldsymbol{r}} \tag{1.10}$$

$$\psi_f(\boldsymbol{r}) = \frac{1}{\sqrt{V}} u_f(\boldsymbol{r}) e^{i\boldsymbol{k}_f\cdot\boldsymbol{r}}, \tag{1.11}$$

where u_i, u_f are the envelope functions at valence band and conduction band, respec-

tively, and V is the normalization factor.

By introducing Equation (1.9), (1.10), (1.11) into (1.6) and consider the momentum conservation between the electron and the photon $\hbar\boldsymbol{k}_f - \hbar\boldsymbol{k}_i = \hbar\boldsymbol{k}$, we can get the matrix elements:

$$\begin{aligned} |M| &= \frac{e}{V}\int u_f^*(\boldsymbol{r})e^{-i\boldsymbol{k}_f\cdot\boldsymbol{r}}(\boldsymbol{E}_0\cdot\boldsymbol{r}e^{i\boldsymbol{k}\cdot\boldsymbol{r}})u_i(\boldsymbol{r})e^{i\boldsymbol{k}_i\cdot\boldsymbol{r}}d^3\boldsymbol{r} \\ &\propto \int_{unitcell} u_i^*(\boldsymbol{r})\boldsymbol{r}u_f(\boldsymbol{r})d^3\boldsymbol{r}. \end{aligned} \tag{1.12}$$

Secondly, the joint density of states $g(\hbar\omega)$ is given by [1]:

$$g(\hbar\omega) = \frac{2V}{(2\pi)^3}\int \delta[\hbar\omega + E_v(\boldsymbol{k}_v) - E_c(\boldsymbol{k}_c)]d^3\boldsymbol{k}. \tag{1.13}$$

In a simple parabolic electronic band for the direct interband transition, the law of energy conservation requires that:

$$\hbar\omega = E_g + \frac{\hbar^2k^2}{2m_e^*} + \frac{\hbar^2k^2}{2m_h^*}. \tag{1.14}$$

Here we define the reduced electron-hole mass μ by:

$$\frac{1}{\mu} = \frac{1}{m_e^*} + \frac{1}{m_h^*}, \tag{1.15}$$

so Equation (1.14) can be rewritten as:

$$\hbar\omega = E_g + \frac{\hbar^2k^2}{2\mu}. \tag{1.16}$$

To evaluate $g(E)$ for the band edge transition with $E = \hbar\omega$, the joint density of states read as:

$$g(\hbar\omega) = \frac{1}{2\pi^2}\left(\frac{2\mu}{\hbar^2}\right)^{3/2}(\hbar\omega - E_g)^{1/2}, \hbar\omega \geq E_g \tag{1.17}$$

So far we introduce the transition matrix M and joint electron-hole density of states, then the interband transition rate $W_{i\to f}$ can be calculated by substituting Equation (1.12), (1.17) into (1.5). The calculation for different materials has to be treated differently due to their unique atomic orbitals, which give rise to different electron Bloch states.

1.1.3 Interband Luminescence

As the opposite process of light absorption, the luminescence for a direct bandgap semiconductors happens when the excited carriers relax their excess energy (kinetic energy) towards the band extrema and then radiatively recombine, accompanied by the emission of one photon, as shown in 1.1.

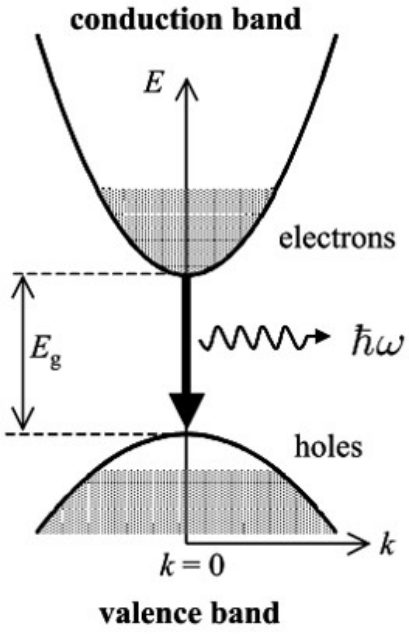

Figure 1.1: Schematic illustration of the interband luminescence in a direct bandgap semiconductor. The shading area represents the occupied states by electrons. [1]

The intensity at frequency ω can be similarly written as [1]:

$$I(\hbar\omega) \propto |M|^2 g(\hbar\omega) \times level\ occupancy\ factors. \tag{1.18}$$

After the system reaches the quasi-equilibrium, the electrons will obey the Fermi-Dirac distribution and the total number has to satisfy the following equation [1]:

$$N_e = \int_{E_g}^{\infty} g_c(E) f_e(E) dE, \tag{1.19}$$

$$f_e(E) = \frac{1}{exp(E - E_F^c)/k_B T + 1}. \tag{1.20}$$

At low carrier densities, the Fermi-Dirac distribution can be approximated by the Boltzmann statistics:

$$f(E) \propto exp\left(-\frac{E}{k_B T}\right). \tag{1.21}$$

Thus, the luminescence intensity can be evaluated by the following relation [1]:

$$I(\hbar\omega) \propto (\hbar\omega - E_g)^{1/2} exp\left(-\frac{\hbar\omega - E_g}{k_B T}\right). \tag{1.22}$$

However, for an indirect bandgap semiconductor, the luminescence process needs the absorption/emission of phonons to conserve momentum, as depicted in 1.2. Such process needs to consider the many-body interaction including carrier-phonon, carrier-photon or carrier-carrier interaction at high carrier densities, which is more complicated than the direct transition.

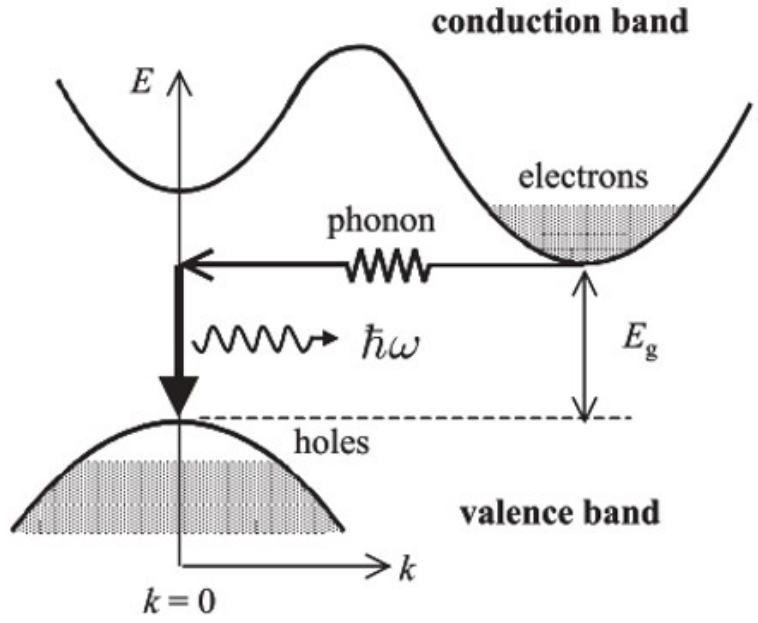

Figure 1.2: Schematic illustration of the interband luminescence in an indirect bandgap semiconductor. The luminescence process requires the assistance of phonons to conserve momentum. [1]

1.1.4 Excitons in Bulk Semiconductors

The interband transition lifts an electron to the conduction band, leaving a hole in the valence band. Such photo-excited electron and hole could interact with each other via Coulomb attraction, which creates a new type of quasiparticle, called excitons. Based on how strong the electron is bounded with a hole, excitons are classified into two types: the Wannier-Mott excitons and Frenkel excitons. As shown in Figure 1.3, the Wannier-Mott excitons are weakly bound electron-hole pairs. The envelope of exciton wave functions extends to several unit cells (see Figure 1.3). On the contrary, the Frenkel excitons are smaller, of the same order as the size of the unit cell. In general, the Wannier-Mott

exciton exists in most of the inorganic semiconductors while the Frenkel exciton does in organic semiconductors.

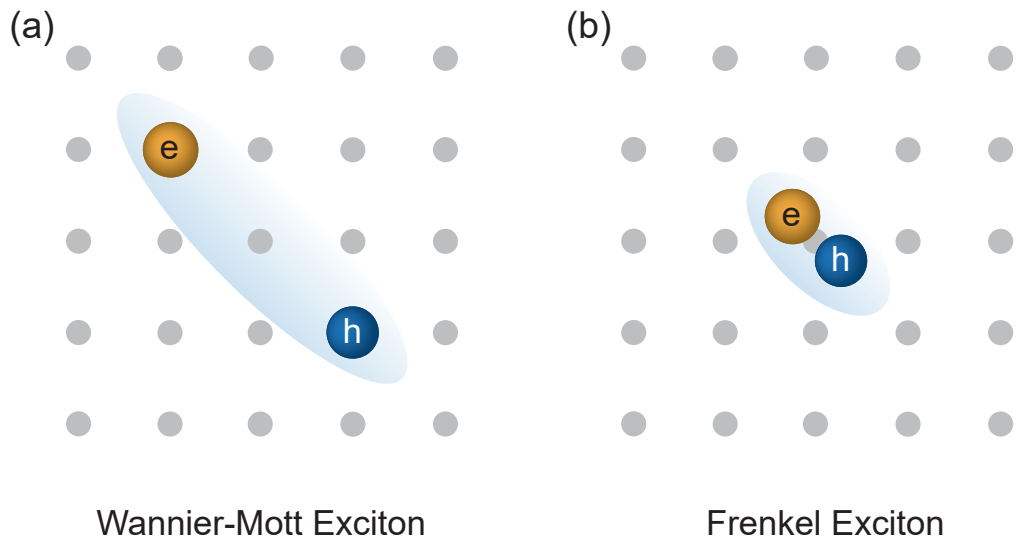

Figure 1.3: Two types of excitons. (a) the Wannier-Mott exciton. (b) the Frenkel exciton.

In analogy to the hydrogen atom, free excitons in a bulk semiconductor can be characterized by the exciton binding energy and Bohr radius, as given by:

$$E_b(n) = -\frac{\mu}{m_0}\frac{1}{\epsilon_r^{*2}}\frac{R_H}{n^2} = -\frac{E_{b,X}}{n^2}, \tag{1.23}$$

$$a_B(n) = \frac{m_0}{\mu}\epsilon_r^* n^2 a_H = n^2 a_X, \tag{1.24}$$

where the exciton reduced mass is $\mu = (1/m_e^* + 1/m_h^*)^{-1}$, the Rydberg energy $R_H = 13.6$ eV and Bohr radius $a_H = 5.29 \times 10^{-11}$ m of the hydrogen atom [18]. In the exciton case, they are replaced by the exciton binding energy $E_{b,X}$ and Bohr radius a_X. Same as the discrete energy levels of hydrogen atoms, the Coulomb attraction of excitons in semiconductors will lower down the energy of the system by E_b/n^2 for different exciton species. The exciton energy is given by:

$$E_X(n) = E_g - \frac{E_{b,X}}{n^2} + \frac{\hbar^2 \boldsymbol{k}_X^2}{2(m_e^* + m_h^*)}. \tag{1.25}$$

The existence of excitons plays an important role in light-matter interaction, leading to strong light absorption and emission. As shown in Figure 1.4, the dashed line gives the absorption profile of $(\hbar\omega - E_g)^{1/2}$ in a direct gap semiconductor. When the excitonic

effect is considered, it will introduce discrete energy levels within the bandgap, leading to strong excitonic absorption lines labeled by the quantum number n.

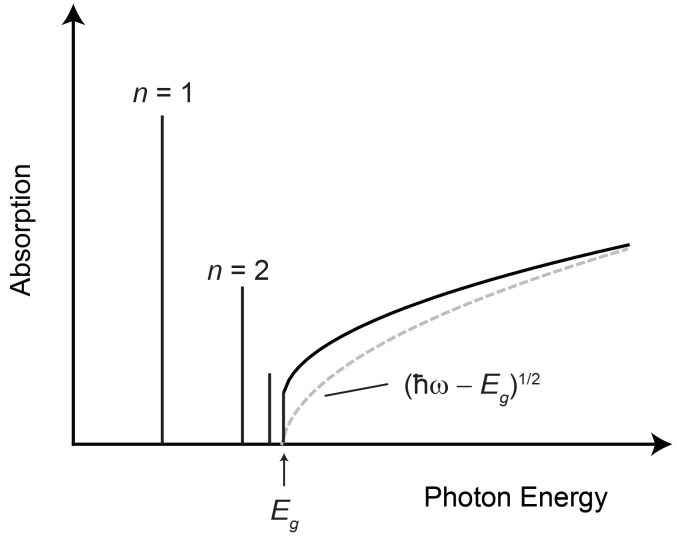

Figure 1.4: The schematic of an excitonic band edge absorption spectrum for a direct gap semiconductor. The dashed line is the expected absorption without exciton effect.

However, the formation of excitons requires their binding energy to be strong enough to overcome the thermal energy, which means $E_b \geq k_B T$, where k_B is the Boltzmann constant and T is the lattice temperature. If the binding energy is below the thermal energy, excitons will be dissociated via phonon scattering and thus only free carriers exist above the critical temperature ($E_b = k_B T$). The binding energy of excitons in a bulk semiconductor is typically several meV or tens of meV. With the development of techniques in material synthesis, people have found that, by introducing quantum confinement in the crystal dimensions, the exciton binding energy can be greatly enhanced. The excitons in a two-dimensional semiconductor shall be discussed in the next section.

1.1.5 Excitons in Two-dimensional Semiconductors

In two-dimensional semiconductors such as quantum wells, one dimension of the crystal size is reduced to only few unit cells, which is set as z-direction. As a result, the electrons and holes experience strong confinement in z-direction while move freely in the other two dimensions (set as xy-plane). The wavefunctions of electrons and holes shall be written as $\Phi(x, y, z) = \psi(x, y)\psi(z)$. In the xy-plane, the wavefunctions are taken as the same form of the Bloch functions of carriers in free motion (see Equation 1.1). In the $z-$direction, we consider the simplest case of infinite confining potential in

an L-thick well, the Schrödinger equation for the z-direction is written as:

$$-\frac{\hbar^2}{2m^*}\frac{d^2\psi(z)}{dz^2} = E_z\psi(z). \tag{1.26}$$

To satisfy the boundary condition ($\psi(z = L) = \psi(z = 0) = 0$), the equation should have a standing-wave solution with the form of

$$\psi_n(z) = \sqrt{\frac{2}{L}}sin(k_n z + \frac{n\phi}{2}), \tag{1.27}$$

where n denotes the quantum number and k_n = $n\pi/d$ is the quantized wavevector at z-direction. The eigen energy E_n corresponding to quantum number n is given by

$$E_n(z) = \frac{\hbar^2 k_n^2}{2m^*} = \frac{\hbar^2}{2m^*}(\frac{n\pi}{d})^2. \tag{1.28}$$

In addition to the quantized eigen energies at z-direction, the quantum confinement effect enhances the exciton binding energy as well since the wavefunctions of electrons and holes overlap more compared with the case in bulk crystal. The exciton energy in a two-dimensional structure is given by [18]:

$$E_X^{2D}(n) = E_{xy} + E_z + \frac{\hbar^2 k_X^2}{2(m_e^* + m_h^*)} - \frac{E_{b,X}}{(n - 1/2)^2}, n = 1, 2, 3... \tag{1.29}$$

The enhanced electron-hole interaction due to quantum confinement leads to larger exciton oscillator strength and binding energy, which makes excitonic features dominate in optical processes. Compared with conventional group III-V quantum wells, the layered-two-dimensional semiconductors are natural quantum-well-like materials that have even stronger excitonic features (with hundreds of meV exciton binding energy). In addition to the quantum confinement effect, the dielectric confinement is reported to be another important factor to boost the exciton behaviour in two-dimensional materials, which will be discussed later in Section 1.2.3.

1.2 Exciton Physics in TMDs Monolayers

Two-dimensional (2D) materials have attracted enormous attention due to their unique optical and electrical properties. In general, 2D materials are the atomic layer of their bulk counterpart, which interacts with the adjacent layers via van der Waals (vdWs) force. Typically, 2D materials have a morphology with sub-nanometer thickness ($e.g.$, graphene $\approx$ 0.35 nm), providing huge potentials for integration in optics and electronics. The study on 2D materials has attracted worldwide interest again since the graphene was first obtained by mechanical exfoliation in 2004, where its electronic properties were intensively investigated in the past decade. It shows gapless Dirac-like electronic structures, leading to ultrahigh carrier mobility and properties such as unusual tunneling, confinement and the integer quantum Hall effect [19]. Inspired by the finding of graphene as a semimetal, researchers are also motivated to explore semiconductors and insulators in the layered-material family. In 2010, researchers found group-VIB transition metal dichalcogenides (TMDs) MX_2 (M = Mo, W; X = S, Se) exhibit strong optical emission with electronic bandgaps in the visible light region ($\sim$ 1.7-2.0 eV) when thinning down to monolayers [3,4]. In addition, the unique spin and valley properties stimulate appreciable interest to explore their potential applications in spintronics and valleytronics. In the following, I will briefly review those properties on TMDs monolayers.

1.2.1 Electronic Band Structure and Optical Properties in TMD Monolayers.

The electronic band structure of TMDs monolayers are largely determined by their lattice structure. For the bulk TMDs crystals, there are three different stacking orders for the layered structures, $e.g.$, 1T, 2H (see Figure 1.5d) and 3R (see Figure 1.5e) [2]. The 1T phase for group-VIB TMDs is not stable. For the 2H and 3R phases, they share the identical building block, that is, the monolayer. The monolayer is composed of three atomic planes, of which the top and bottom planes are the chalcogen atom and the middle one is the metal atom. These three atomic layers form a 2D hexagonal lattice, as shown in Figure 1.5a. For the 2H-phase bulk crystal, a unit consisting of two monolayers, where the adjacent monolayers are 180° rotation of each other, is repeated (see Figure 1.5d). For the 3R phase, the unit is composed of three layers, where the neighboring layers are translation of each other (see Figure 1.5e) [2]. Theoretical study has predicted that 2H

stacking is more stable than the 3R stacking [20].

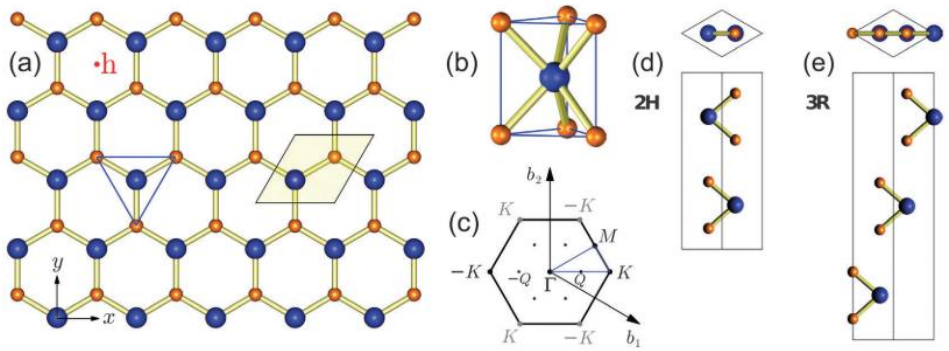

Figure 1.5: (a) Top view of TMDs monolayers. The blue and orange circles denote M and X atoms (M= Mo, W; X= S, Se), respectively. (b) Trigonal structure of a unit cell for the crystals. (c) The first Brillouin zone. b_1 and b_2 are the reciprocal lattice vectors. (d) The top and side view for 2H stacking order. (e) The top and side view for 3R stacking order. [2]

Figure 1.6 shows the calculated MoS_2 electronic band structures ranging from bulk to monolayer [3]. According to the calculation, bulk MoS_2 is an indirect bandgap semiconductor with the minimum of conduction band located at Λ point (at the half point of K and Γ) while the maximum of valence band located at Γ point in the Brillouin zone. As the size shrinks, the energies of several band extrema regarding the Λ and Γ points, evolves in opposite ways. In particular, the energy of conduction band extremum at Λ point increases and the energy of valence band extremum at Γ point decreases, resulting in a transition from indirect bandgap at Λ/Γ points to direct bandgap at K/K points when thinning down to monolayers. This property is later found to apply to all the group-VIB TMDs monolayers.

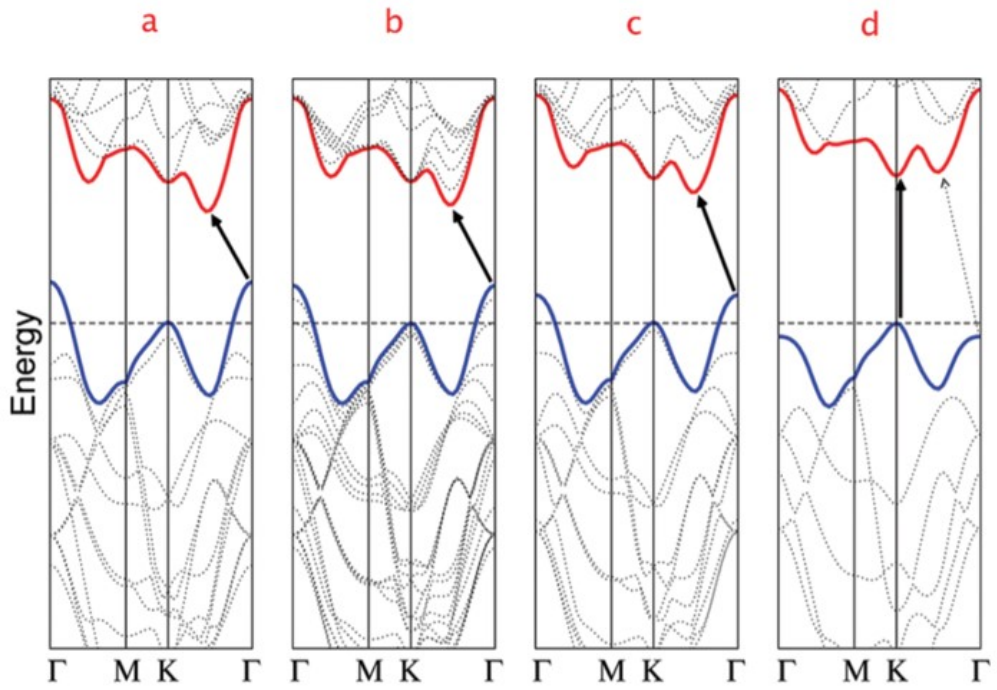

Figure 1.6: Calculated MoS_2 band structures of different thickness. (a) bulk, (b) quadrilayer, (c) bilayer and (d) monolayer. [3]

As a result of the transition in electronic band structures, optical properties including light absorption and emission will be significantly enhanced in the direct gap monolayer semiconductors. Figure 1.7 shows the PL spectra of mono- and bilayer MoS_2 [4]. The monolayer PL emission is much stronger than that of the bilayer. The inset in Figure 1.7 also gives the layer-dependent quantum yield, which suggests that the indirect to direct bandgap transition strongly facilitates the light emission efficiency.

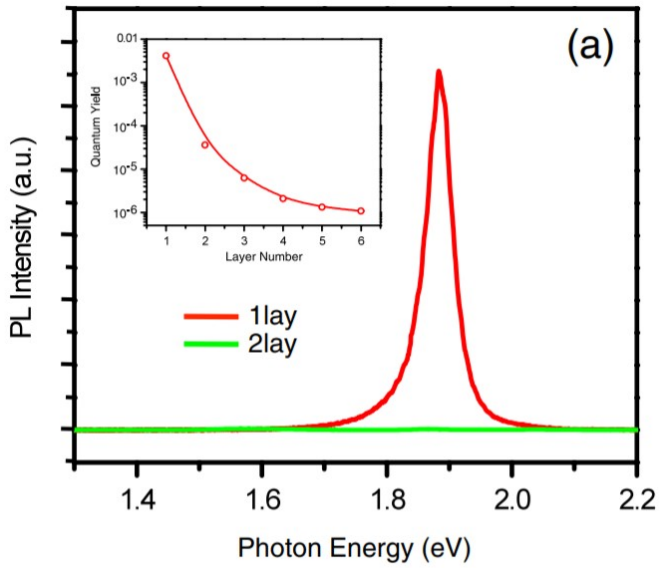

Figure 1.7: Layer-dependent PL spectra of MoS_2. PL spectra of mono- and bilayer. Inset: the quantum yield of MoS_2 of different layers. [4]

1.2.2 Coupled Spin and Valley Physics and Valley-dependent Optical Selection Rule

In addition to the enhanced PL emission, unique properties such as spin and valley physics arise from the structural symmetry and electronic band structure in TMDs monolayers. To start with, I will first introduce the structural symmetry in TMDs monolayers. TMDs monolayers have the hexagonal lattice structure similar to graphene but with different adjacent atoms as shown in Figure 1.8 [5].

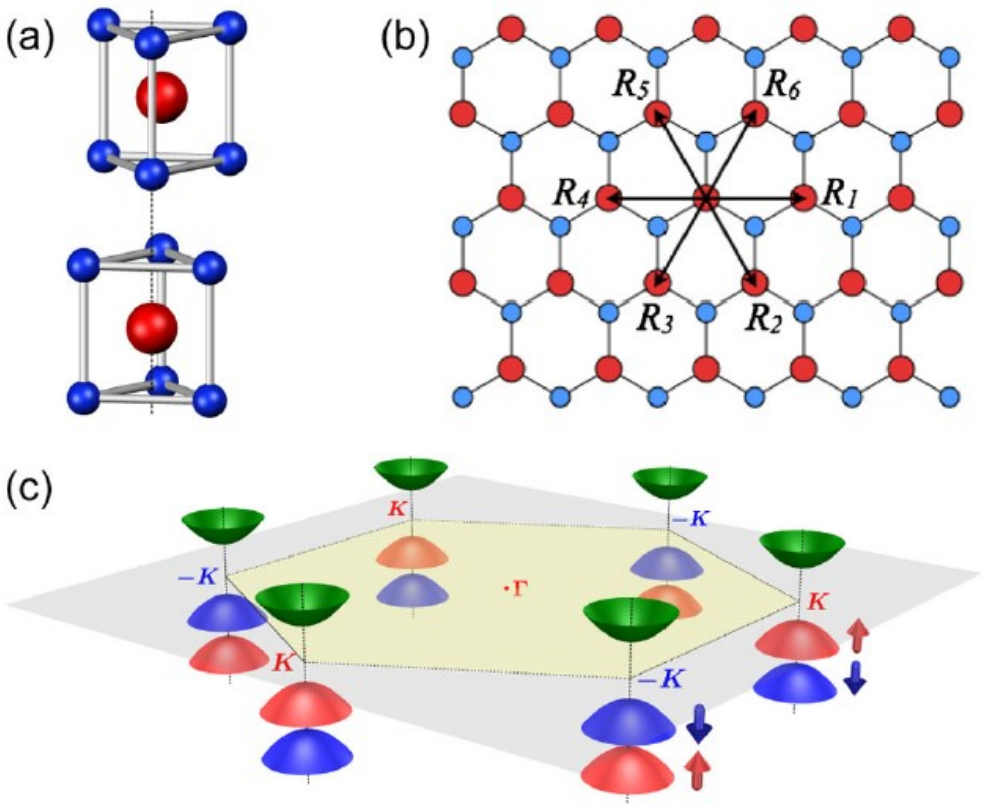

Figure 1.8: Structure of MoS_2. (a) The unit cell of bulk $2H$-stacking MoS_2, where inversion symmetry holds but is absent in monolayers. (b) The hexagonal lattice structure of MoS_2 monolayers. $\boldsymbol{R}_i$ are the vectors connecting nearest Mo atoms. (c) The Brillouin zone and band structure at the K points. The blue and red arrows denote opposite electron spins. [5]

In the bulk $2H$-stacking MoS_2, the unit cell has an inversion center located in the middle plane (see Figure 1.8(a)), but it is broken in the monolayers. The inversion symmetry breaking leads to six energy-degenerate band edges located at the K points (see Figure 1.8(c)). Taking into account the spin-orbital interaction, first-principles calculations have predicted large spin-splitting in the valence band edges ($\sim$ 148, 183, 426 and 456 meV for the MoS_2, $MoSe_2$, WS_2 and WSe_2 monolayers, respectively) at K points while the energy splittings of conduction band edges at K points are much smaller (tens of meV) [21]. Another important symmetry called time-reversal symmetry requires that the spin signs of the band edges at different adjacent K valleys must be opposite [5], as shown in Figure 1.9. In other words, the spin indices of the both conduction band and valence band edges (spin up and spin down) are locked with the valley indices (K or K'). This spin-valley locking leads to unique valley-selective optical selection rules as described in Figure 1.9.

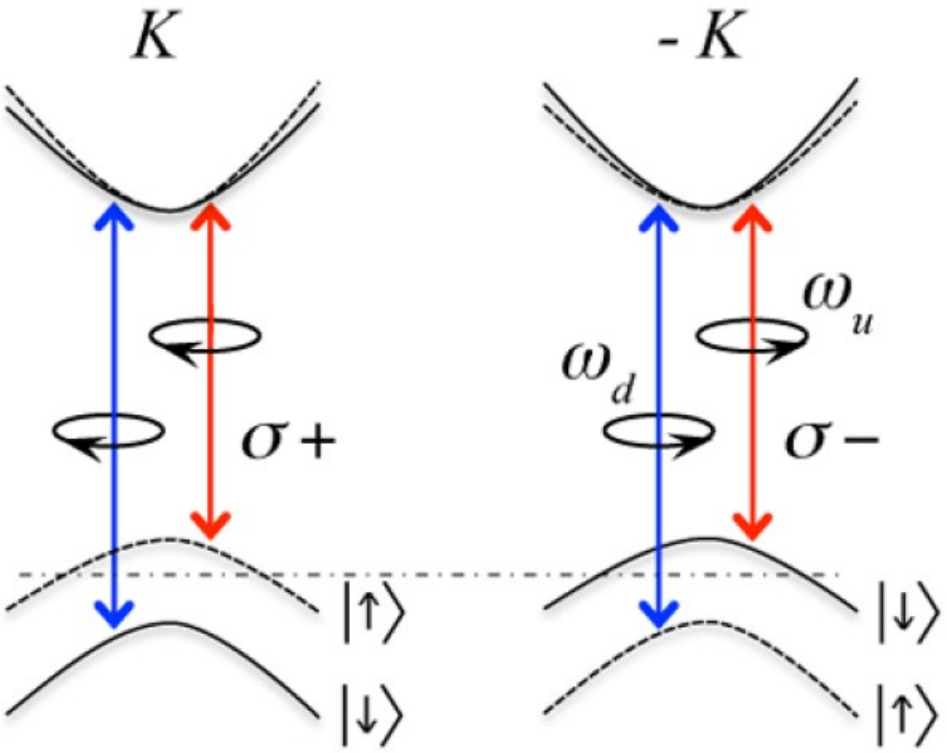

Figure 1.9: Valley-selective optical selection rules. The schematic shows the spin-split conduction and valence band edges at K and $K^{'}$ points. The dashed (solid) curves represent bands with spin-up (down) pointing to the out-of-plane direction. The interband transition at K ($K^{'}$) valley requires the absorption/emission of a photon with left-handed $\sigma+$ (right-handed $\sigma-$) circular polarization. [5]

The interband transition at K ($K^{'}$) valley requires the absorption/emission of a photon with left-handed σ^{+} (right-handed σ^{-}) circular polarization. This property enables us to selectively generate carriers with various combination of valley and spin indices by using light with different circular polarizations and energies [5, 22]. To characterize the valley polarization of carriers, one can define degree of valley polarization (DVP) by $|(I_{\sigma^{\pm}} - I_{\sigma^{\mp}})/(I_{\sigma^{\pm}} + I_{\sigma^{\mp}})|$, where $I_{\sigma^{\pm}}$ denotes the detected PL intensity of left-handed + (right-handed -) circular light. The property of creating carriers with certain spin and valley index via optical injection makes TMDs monolayers promising candidate for spintronics and valleytronics.

1.2.3 Valley Excitons: Bright and Dark Exciton

Besides the unique electronic band structure and spin-valley locking in TMDs monolayer, the atomically-thin thickness of monolayers leads to strong quantum confinement for carriers, giving rise to prominent excitonic features in optical processes. Figure 1.10

shows the real space schematic of excitons in 3D bulk and 2D monolayer [6].

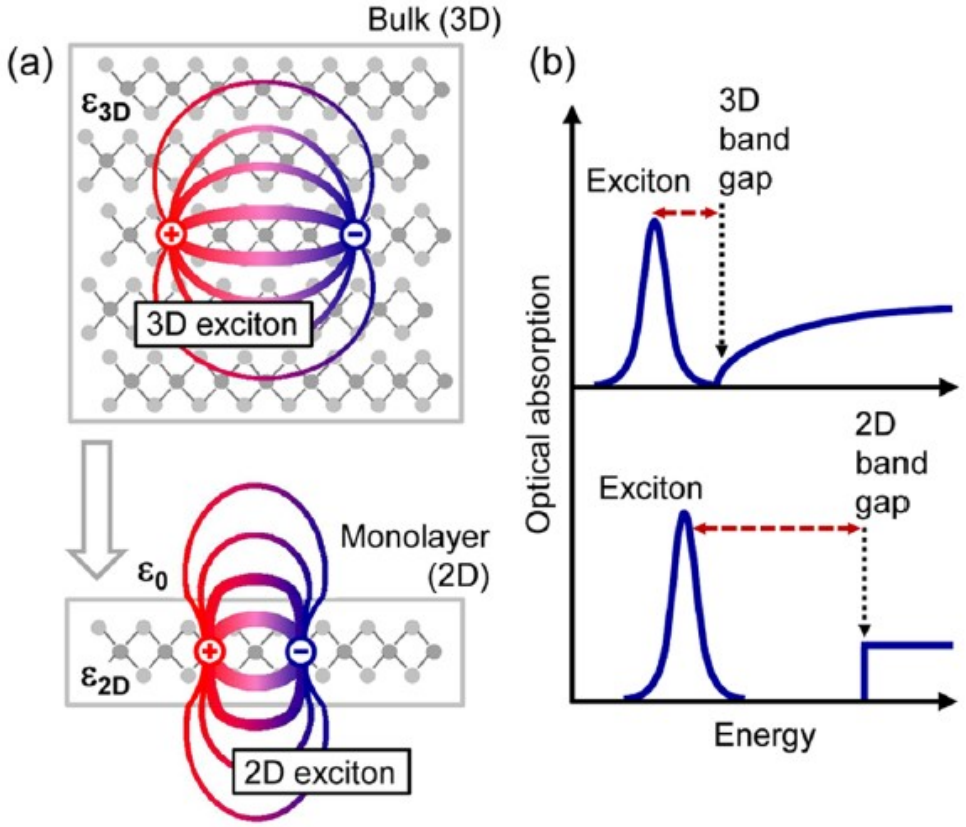

Figure 1.10: Strong confinement in 2D monolayers. (a) The real space schematic of excitons in 3D bulk and 2D monolayer. The dielectric environments are characterized by the vacuum permittivity ϵ_0, ϵ_{3D} for bulk and ϵ_{2D} for monolayer. (b) The change of electronic and excitonic band features in optical absorption. The transition from bulk to monolayer will increase both the band gap and the exciton binding energy. [6]

In the 2D limit, the exciton wave functions that exist in 3D bulk lattice will extend outside of the lattice, leading to a reduced dielectric screening effect. In addition to the spatial quantum confinement, such "dielectric confinement" is another important factor to cause the significant enhancement of Coulomb interaction between electrons and holes, which facilitates the formation of strongly bound excitons. The strong excitonic effect also reflect in the observation of Rydberg-series excitonic states in WS_2 monolayer [6]. As shown in Figure 1.11 [6], the spectrum shows the reflectance contrast derivative of the WS_2 monolayer. The ground state (AX) and its higher Rydberg-series states of A exciton labeled by their quantum numbers (1s, 2s, 3s...) are clearly resolved, from which a binding energy of 0.32 eV is extracted. This value is much larger than the binding energy of conventional semiconductors (such as GaAs with $E_b \approx 5$ meV [23]) and makes excitons in TMDs monolayers stay even at room temperature.

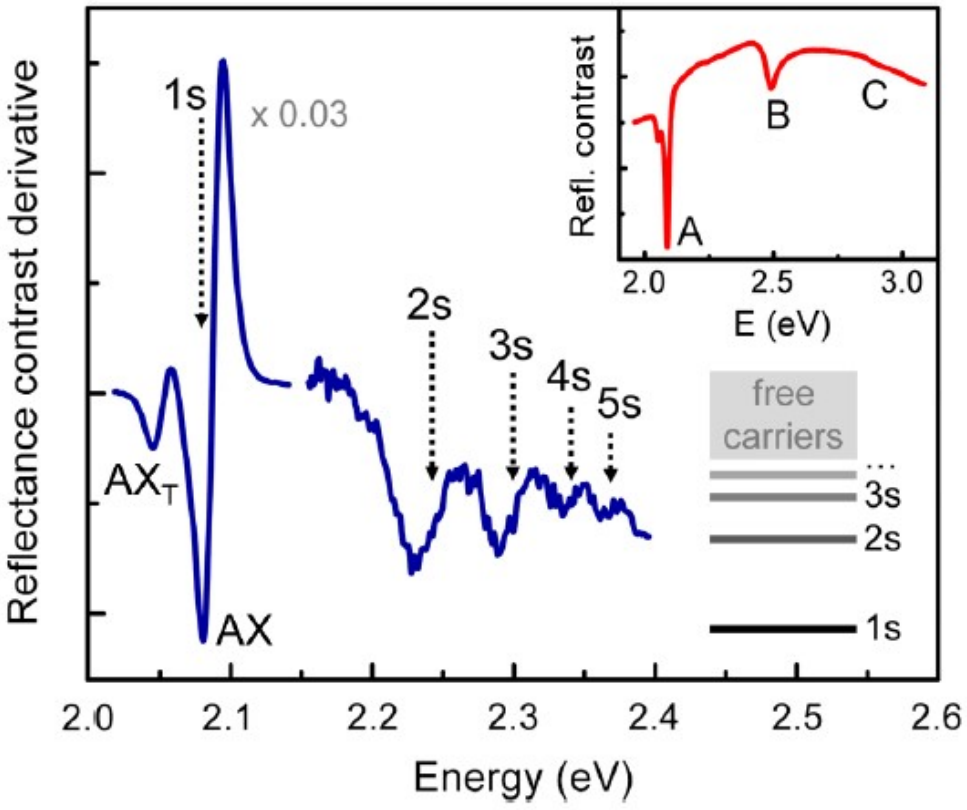

Figure 1.11: Rydberg-series excitonic states in WS_2 monolayer. The spectrum shows the reflectance contrast derivative ($(d/dE)(\Delta R/R)$) of the WS_2 monolayer. The ground state (AX) and its higher Rydberg-series states of A exciton are labeled by their quantum numbers (1s, 2s, 3s...). The inset shows the original reflectance contrast $\Delta R/R$ spectrum, in which the A, B and C transitions can be resolved. [6]

The optical selection rule allows a spin-like transition while forbids the spin-unlike transition by the law of conservation of angular momentum. As a result, the excitons can be classified into two types: the optically allowed (bright) and the forbidden (dark) ones as shown in Figure 1.12 [7]. Theoretical work has calculated for the four TMDs monolayers for the dark-bright splitting for both A and B transitions, in comparison with experimental results shown in Table 1.1. For the A transition, the bright exciton band lies energetically lower in Mo-based monolayers while higher in W-based monolayers than the dark excitons. The different dark-bright energy separation in Mo- and W-based monolayers will strongly alter their optical yield, especially at low temperatures [24].

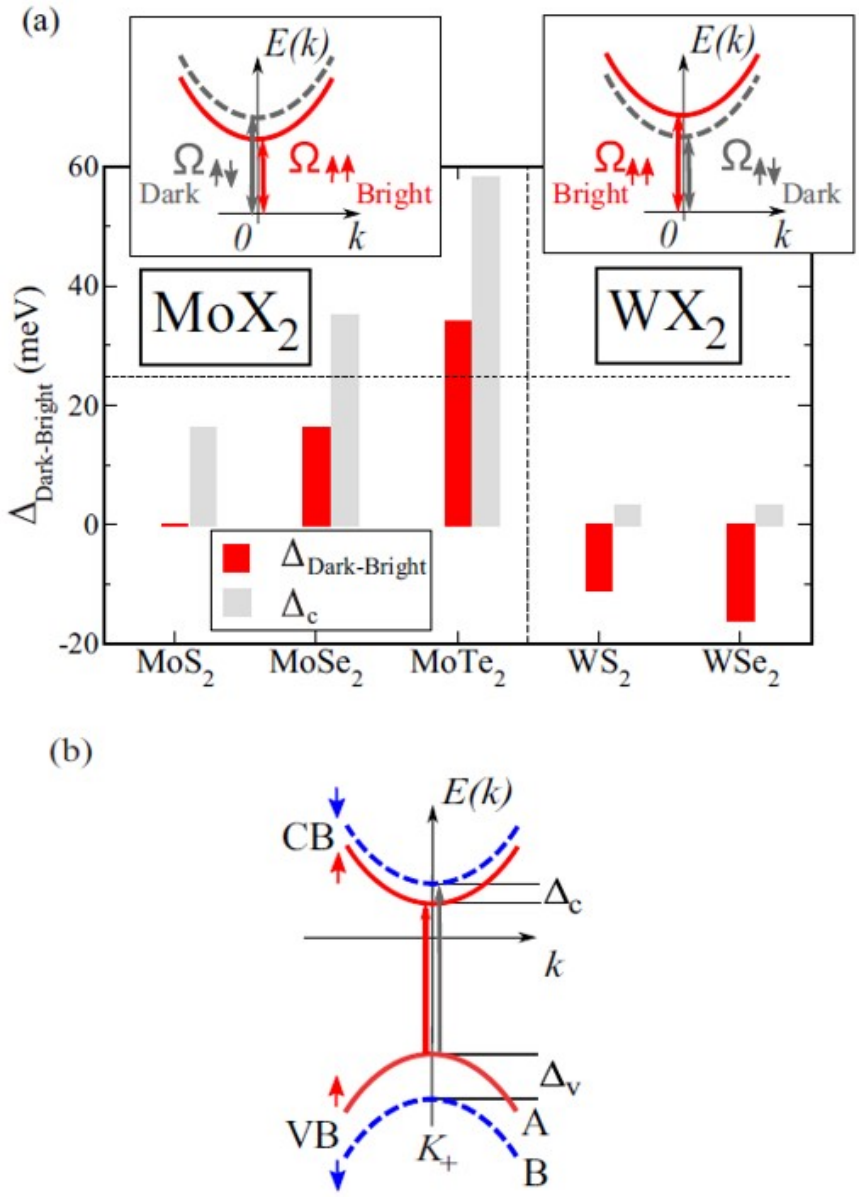

Figure 1.12: Bright and dark excitons in TMDs monolayers. (a) Calculated dark-bright energy splitting of the ground A excitons in MoX_2 and WX_2 monolayers (red bars). The energy of bright excitons is set to zero, in comparison with the spin-split energy of conduction band Δ_c (grey bars). The insets show the exciton representation for MoX_2 and WX_2. (b) Schematic of interband transition for MoX_2 monolayer in the K valley, where the red arrow means the optically-allowed transition while the grey arrow denotes the optically-forbidden transition. [7]

Table 1.1: Calculated energy splitting of Δ_{B-A} ground A and B excitons, and $\Delta_{dark-bright}$ splitting for TMDs monolayers, in comparison with experimental results. The values in parentheses are obtained from G_0W_0-PBE calculations, in comparison with the G_0W_0-HSE calculations. [7]

Monolayer	Δ_{B-A} (eV)		$\Delta_{dark-bright}$ (meV)	
	G_0W_0-HSE	Expt.	A excitons	B excitons
MoS_2	0.18 (0.16)	0.16 [25]	0 (-5)	-24 (-20)
$MoSe_2$	0.24 (0.21)	0.22 [26]	16 (11)	-45 (-37)
$MoTe_2$	0.33 (0.30)	0.26 [27]	34 (25)	-30 (-9)
WS_2	0.45	0.38 [28]	-11	-6
WSe_2	0.49	0.43 [29]	-16	-37

1.2.4 Charged Valley Excitons and Many-body Physics in TMDs Monolayers.

Beside the neutral exciton states, charged exciton states such as trions can be formed by the strong spatial and dielectric confinement. In principle, a trion is a hydrogen-ion-like particle consisting of a neutral exciton (X) and an extra charge. Depending on the type of extra charge, the trion can be negative trion X^- (for an electron) or positive trion X^+ (for a hole). The trion states also play important roles in optical transitions, which relies on the extra charge densities and can be tuned via electrostatic doping. Figure 1.13 shows the reflectance contrast and PL spectra in $MoSe_2$ monolayer [8].

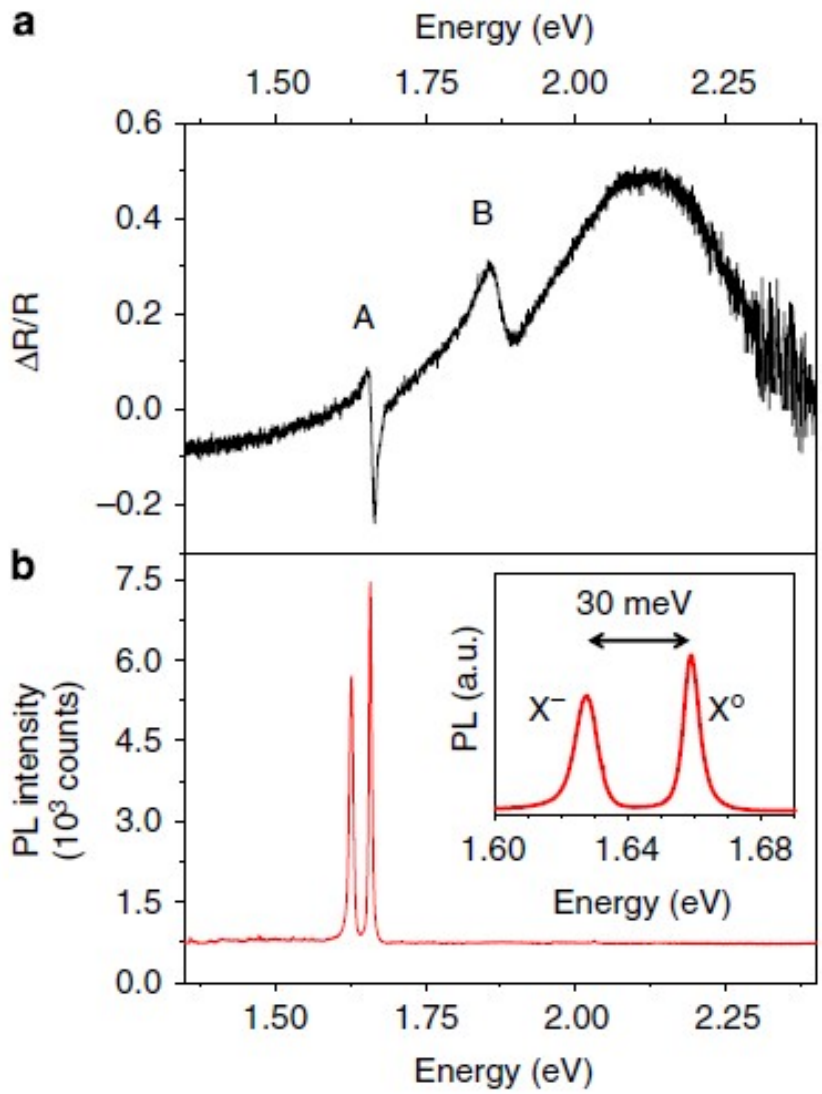

Figure 1.13: Reflectance contrast and PL spectra of monolayer $MoSe_2$ at 20 K. (a) Reflectance contrast spectrum shows the A and B resonances. (b) PL spectrum shows the emission features from neutral A exciton X^0 and negatively-charged exciton (X^-). The inset gives the binding energy of charged exciton of $\sim$ 30 meV. [8]

The absorption features of A and B excitons are clearly resolved in Figure 1.13(a) while trion state X^- is resolved in the emission spectrum with a binding energy of $\approx$ 30 meV. Further, it is shown in Figure 1.14 that the neutral exciton and its charged states can be tuned via electrostatic doping [8].

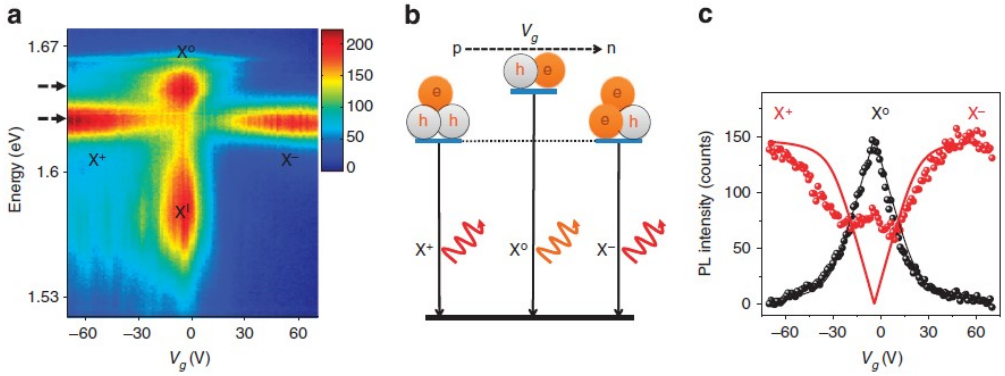

Figure 1.14: Electrostatic control of neutral exciton and trions, (a) 2D mapping of PL spectra as a function of bottom gate voltage. (b) Schematic of the gate-dependent exciton and trions. (c) Extracted intensities (at dashed arrows in (a)) of exciton and two types of trions as a function of bottom gate voltage V_g. [8]

At $V_g \approx 0$, the neutral excitons dominate the emission process while the emission of positive (negative) trions are enhanced by hole (electron) doping, as illustrated in Figure 1.14(b). The extracted intensities of excitons and trions (see Figure 1.14(c)) indicate the transition of neutral excitons into trions with carrier doping, which serves as an efficient way to modulate many-body interactions in TMDs monolayers.

The representation of trions stands well for moderate carrier-doping density. However, with the increase of carrier-doping density (electrons for example), the lattice will be filled by the "sea" of electrons. This "electron sea" could polarize the lattice and strongly interact with the lattice phonons in polar semiconductors, which alters the electronic band structure. In this sense, people tend to use the concept "polaron" to describe this new type of quasi-particle caused by the strong interaction of electrons and lattice phonons. M. G. Kang *et al.* have reported the observation of Holstein polarons in a surfaced doped MoS_2 monolayer by using angle-resolved photoemission spectroscopy (ARPES) [9]. Several theoretical works have predicted that, under strong electron-phonon coupling strength, electrons in a parabolic band (see Figure 1.15(b)) will be scattered by phonons to form e + $n$ph continua, where n is the involved phonon number. These continua state will mix with the parabolic band and make it separate into a series of subbands, accompanied by gap opening and flattening of the dispersion at the phonon-scattered energy $-n\Omega_0, n = 1, 2...$ (see Figure 1.15(c, e) [9].

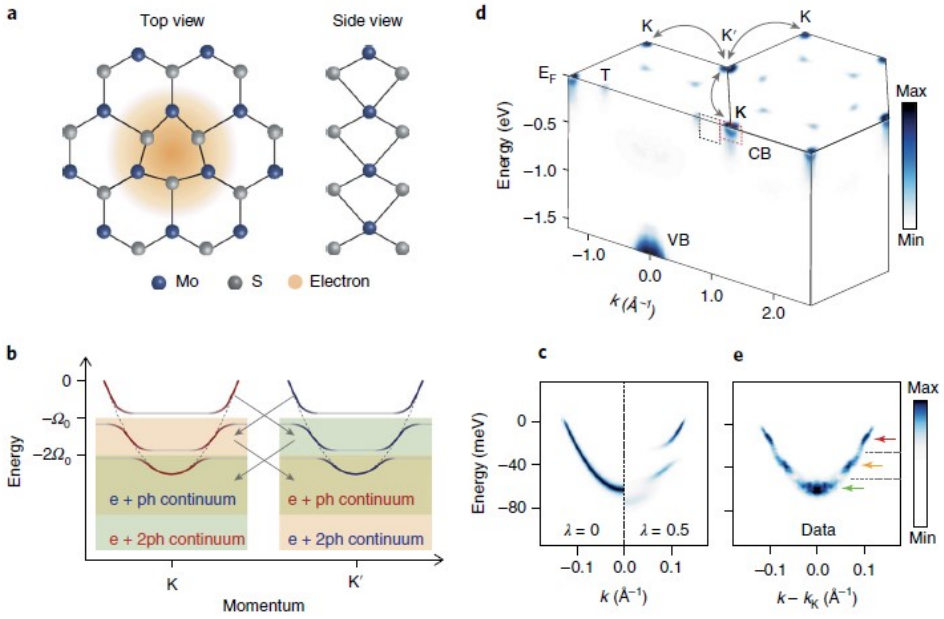

Figure 1.15: Holstein polaron of MoS_2 monolayer. (a) Representation of a polaron (an electron surrounded by phonon could cause by lattice deformation) in MoS_2 monolayer. (b) Energy spectra of Holstein polarons arising from a strong coupling between the $K^{'}$ and K valleys mediated by zone-edge phonons (the arrows denote intervalley scattering). The dashed lines represent the original electron bands in a non-interacting situation. The red and blue lines show the polaron dispersion caused by strong electron-phonon coupling. It shows a band renormalization as well as a series of flat dispersions separated by phonon energy Ω_0 in the continuous band. (c) The simulated dispersion of polarons with zero ($\lambda = 0$) and intermediate ($\lambda = 0.5$) electron-phonon interaction. (d) 3D plot of ARPES spectra measured for MoS_2 doped with Rb atoms at 80 K. (e) High-resolution ARPES spectra taken near the conduction band of K point. The dashed lines represent the energy position of the gaps; the red, yellow and green arrows indicate a series of subbands due to the electron-phonon coupling. [9]

Besides the change of dispersion spectra for electrons, a polaron that drags phonon clouds becomes heavier, with a mass-enhancement factor of $m^*/m_0 \approx 3$ as depicted in Figure 1.16(a). These findings suggest that the intervalley coupling of polarons between $K/K^{'}$ in the exchange of acoustic phonons may be crucial in the formation of Cooper pairs (see Figure 1.16(b)) and could also gain insights into carrier mobility and dynamics in valleytronics.

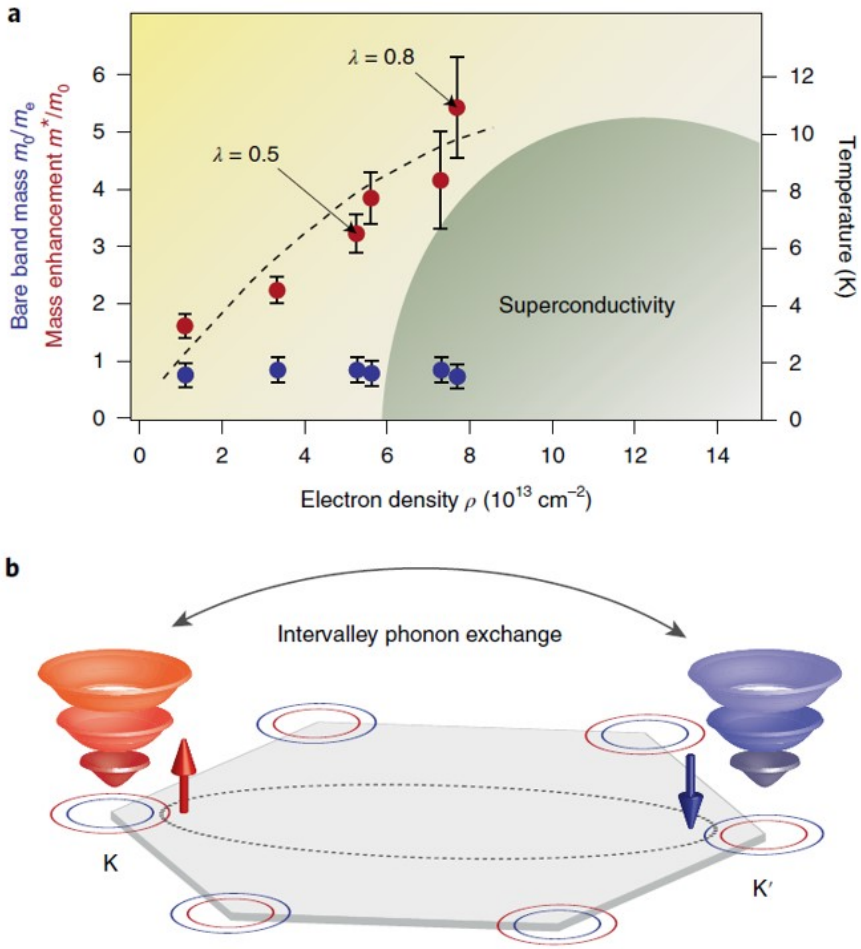

Figure 1.16: Electron-phonon coupling strength and superconductivity. (a) Effective mass of polarons (red circles) and bare bands (blude circles) as a function of electron intensity. The green region shows the superconducting region of MoS_2 [10]. (b) Valley dependent polarons with opposite spin are coupled *via* the exchange of phonons (bipolaronic coupling). [9]

Overall, the strongly bound excitons as well as their different spin-configuration and valley properties make TMDs monolayers the ideal platform to study excitonic physics. Besides the neutral excitons, charged exciton states (trions) are also formed. Carrier doping to monolayers could tune the system from weak coupling (trion) into strong coupling (polaron) regimes, where we can study the many-body physics such as the rich optical and transport properties of these valley-dependent excitonic trions or polarons.

1.3 Motivation

Low-temperature optical spectroscopy has revealed the PL spectra for Mo-based and W-based monolayers, as shown in Figure 1.17 [11]. In general, the Mo-based monolayers show simple emission features. Taking the spectra of $MoSe_2$ and WSe_2 monolayer on SiO_2/Si substrate for example, the $MoSe_2$ spectra can resolve two features that are attributed to the neutral exciton X_A and its negatively-charged state X^-. However, the WSe_2 spectra show additional features below the X_A and X^-, which is much more complicated compared with Mo-based compounds. It indicates different formation mechanisms of the excitonic states in W-based monolayer, which is related to its distinct electronic band structures. However, the origins of these additional emission features in W-based monolayers remain ambiguous and their relationship with the electronic band structures needs to be further explored.

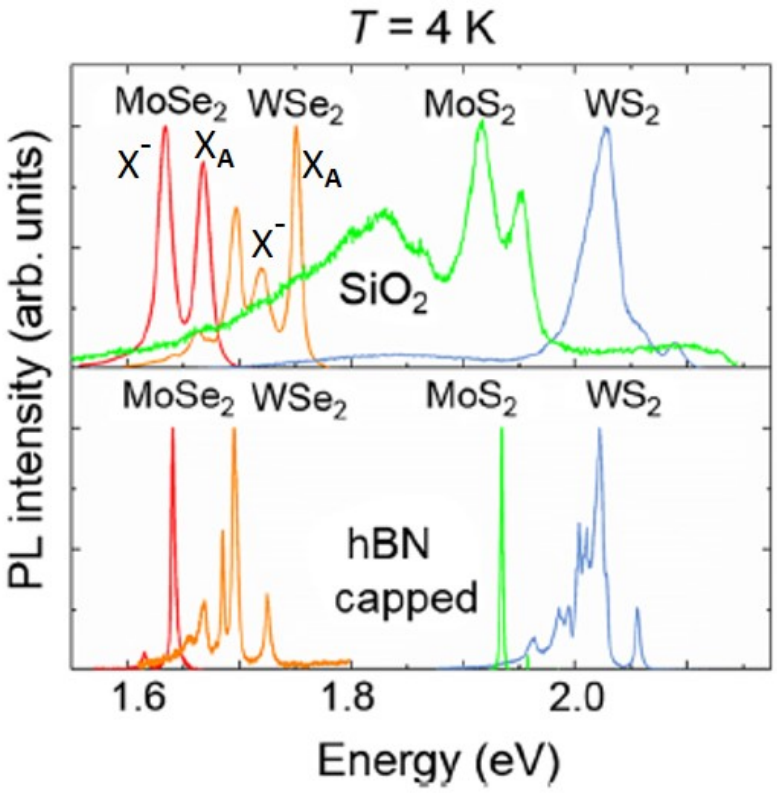

Figure 1.17: Low-temperature PL spectra for $MoSe_2$, MoS_2, WSe_2, WS_2 monolayers on SiO_2 and encapsulated by hBN [11].

Herein, our motivation is to understand the complex excitonic features in W-based monolayers and their carrier dynamics in optical processes including exciton formation, relaxation and decay, in which the exciton-phonon, exciton-charge and exciton-exciton

scattering processes play important roles. On the other hand, the change of dielectric environment could change the linewidth broadening and renormalize the electronic bandgap of TMDs monolayers (see the spectra of hBN-capped samples in Figure 1.17). Thus, by employing such techniques, we aim to fabricate samples with higher optical quality, which allows us to reveal more detailed emission structures that could not be observed in monolayers on SiO_2/Si substrate.

In addition, we are also motivated to study the optical properties of excitonic features in TMDs monolayers under external control such as electrostatic doping and magnetic field. Carrier doping can tune the exciton from neutral state to charged state, which helps identify the complicated features in W-based compounds that is under debate in many studies. It also enables us to gain insights into the underlying carrier dynamics and many-body physics. By applying magnetic field, we are able to destroy the valley degeneracy, examine the valley polarization and extract important physical parameters such as g-factors for the excitonic species. These studies will advance the fundamental understanding of excitonic physics in TMDs monolayers.

1.4 Organization of the Thesis

The organization of the thesis is arranged as follows: In Chapter 1, I will introduce the fundamental knowledge of electronic band structure, interband optical transition and the concept of excitons. It is followed by the review of TMDs monolayers including the electronic band structure, lattice structure, symmetry, unique spin-valley physics and valley-dependent optical selection rules. Finally, I will discuss the excitons and their charged states, and then explain the motivation of my Ph.D. work.

In Chapter 2, I will introduce the optical spectroscopic techniques that have been used in the thesis such as reflectance measurement, photoluminescence excitation (PLE) spectroscopy and polarization-resolved photoluminescence measurements. In addition, the theory of resonant Raman spectroscopy will be introduced that is useful to probe exciton-phonon interactions in TMDs monolayers.

In Chapter 3, I will describe the processes to fabricate high-quality samples including mechanical exfoliation to obtain TMDs monolayers, heterostructure fabrication by stacking layers and electron beam lithography (EBL) used for making field-effect transistor (FET) devices.

In Chapter 4, I will present the investigations on probing the momentum-indirect

transition in WS_2 monolayers that could explain for the low-energy features in the photoluminescence spectrum of W-based compounds. Under near-resonant excitation condition, multiple scattering processes between excitons and phonons carrying non-zero wavevector are revealed, indicating the presence of indirect excitons whose constituent electrons and holes locate at different valleys, beside the well-understood direct excitons with their electrons and holes located at the same valley.

In Chapter 5, I will present the results of electrical control on the optical absorption and emission of excitons and their charged states in a high-quality hBN-encapsulated WS_2 heterostructure. The heterostructure shows much narrower emission linewidth compared to bare monolayers on SiO_2/Si substrate, which enables us to resolve more details on their excitonic emission features. In addition, via electrostatic doping, we observe the evolution of PL spectra from a relatively neutral state to the Fermi edge singularity, where the existence of photoexcited electron-hole pairs changes from as charged states to exciton-plasmon quasiparticles. The Fermi edge singularity may indicate a transition from the fermion-like particles to boson-like particles, which changes the interactions between photoexcited electron-hole pairs and the highly-dense Fermi gas in the TMDs monolayers.

In Chapter 6, I will discuss the results of magnetic control on the emission features up to 30 T for hBN-encapsulated WS_2 and MoS_2 heterostructures. Under magnetic field, the valley degeneracy in TMDs monolayers will be broken. Thus, we will compare their valley polarization combined with polarization-resolved PL. Moreover, by tracking the energy shift with the magnetic field, we extract the g-factors for different excitonic states and could gain information on their compositions in terms of spin and valley configurations. Our results gain critical insights into the magneto-photoluminescence of different trion species in TMDs monolayers, leading towards a complete understanding of the optical and electronic properties of TMDs monolayers in the magnetic field.

In Chapter 7, all the findings will be summarized and an outlook for further research on TMDs monolayers will be discussed such as interlayer spin and valley transfer of charges in a heterostructure, that provides new possibilities to control carriers' spin and valley properties.

Chapter 2

Optical Spectroscopy

The optical properties of the TMDs monolayers were investigated via steady-state spectroscopy techniques. In this chapter, I will first introduce the experimental setup used for reflection, polarization-resolved photoluminescence measurements. Combined with multiple laser excitation energies, photoluminescence excitation spectroscopy (PLE) technique is used to study the emission features, from which we can look into the underlying absorption and relaxation processes. As a special case, when the laser energy is in near resonance with the electronic band transition, the intensity of Raman scattering will be greatly enhanced, from which important electron-phonon scattering processes can be resolved.

2.1 Experimental Setup

General steady-state optical spectroscopy includes absorption (A), reflection (R) and photoluminescence (PL) spectroscopy. The intrinsic optical transitions that depend on the electronic resonances can be detected by the mentioned techniques.

Figure 2.1 shows the schematic illustration of the setup for steady-state reflection and PL measurements. In general, the setup consists of the excitation and detection system. For the reflection measurements, the sample is excited by a white light source that covers a broadband wavelength range ($e.g.$, a quartz tungsten halogen lamp). For the PL measurements, the sample is excited by lasers with linear polarization. The wave vectors of the excitation and detection light are denoted by $\boldsymbol{k}_{exc}$ and $\boldsymbol{k}_{det}$, respectively. The excitation light beams are focused onto the sample surface by a microscope objective. A variety of objectives are available including 10×, 50× and 100×. The choice of objectives depends on the sample size and laser spot size needed for the measurements. In the back-scattering configuration as described in Figure 2.1, the scattered light is collected in the opposite direction ($\boldsymbol{k}_{det}$) through the same objective, which collects both the PL signals as well as the reflected and scattered laser light from the sample surface.

To sort the signals out and protect the detector from intense laser intensity, proper optical filters are needed in front of the entrance slit of the spectrometer to remove the strong laser background. The filters could be long-pass, short-pass or notch filters. After passing through the optical filter, the signals are focused onto an entrance slit by a lens and then directed to a dispersive grating that can spatially separate light of different wavelengths. Multiple blaze gratings are available including 150 grooves/mm, 300 grooves/mm, 600 grooves/mm and 1800 grooves/mm, depending on the blaze wavelength, wavelength resolution or spectral range that is needed for the measurements. For example, all the measurements in this thesis are within the range of visible light, from which we should choose blaze wavelength accordingly. For the wavelength resolution, a 300 grooves/mm grating has a resolution of $\sim$ 0.11 nm while a 1800 grooves/mm grating has a resolution of $\sim$ 0.02 nm. On the contrary, the 300 grooves/mm grating can acquire a spectral range of $\sim$ 110 nm within a single window, which is more efficient for broad spectral measurements, compared to 1800 grooves/mm grating that has a spectral range of $\sim$ 16 nm. Therefore, one needs to choose the proper grating accordingly.

When the signals are sorted out by wavelength, it is reflected by a mirror and finally detected by a charged-coupled-device (CCD) detector, which is cooled by liquid nitrogen to reduce the dark currents and achieve a better signal-to-noise ratio. In addition, the sample can be mounted inside the cryostat cooled by a continuous flow of either liquid nitrogen (77 K) or helium (4.2 K), depending on how much the temperature is needed for the measurement. To perform the polarization-resolved PL measurements, two polarizer sets consisting of a linear polarizer (LP) and a quarter waveplate ($\lambda/4$) are needed to generate and detect circularly-polarized excitation and signal light, respectively.

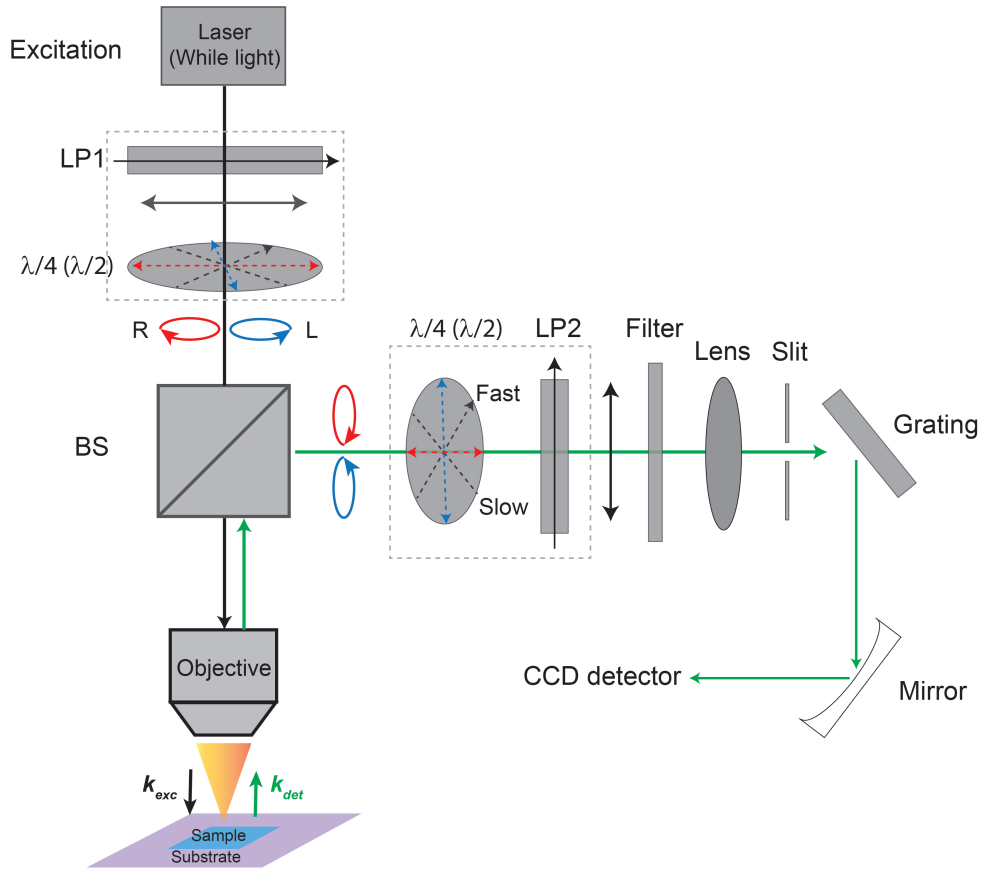

Figure 2.1: Schematic illustration of the set up for reflection, polarization-resolved PL measurements. For the reflection measurement, the excitation is from unpolarized white light sources. For PL measurements, the excitation comes from linearly-polarized lasers. The light beams are focused onto the sample surface *via* microscope objectives. The signals are collected by the same objective and sent into a spectrometer, in which the signal is dispersed by a grating and detected by a CCD detector. The directions of the excitation and detection are indicated by $\boldsymbol{k}_{exc}$ and $\boldsymbol{k}_{det}$. For polarization-resolved measurements, a polarizer set consisting of a linear polarizer (LP) and a quarter waveplate ($\lambda/4$) is used to generate or detect circularly-polarized light, indicated by 'R' for right-handed polarization and 'L' for left-handed polarization.

2.1.1 Triple-grating Spectrometer for Near-resonance Measurements

When the laser excitation is extremely close to the PL signals, it is difficult for normal filters to remove the reflected laser beam, thus making it difficult to detect the PL signal. To overcome such problem, the triple-grating spectrometer configured in subtraction mode was invented so as to detect optical signals that are extremely close to the laser excitation. As shown in Figure 2.2, the triple-grating spectrometer literally has three gratings, among which two gratings (Grating 1 and 2) together with the Slit 2 work as a bandpass filter to allow a window of light with wavelength in the range

of λ_1 and λ_2 to pass. Finally, Grating 3 disperses the signal in the window onto the CCD detector. By calibrating the Grating 1 and 2, we are able to approach the limit with λ_1 or $\lambda_2 \approx \lambda_e xc$ so that the laser light is excluded in the collected signal. The triple-grating spectrometer enables us to perform near-resonance PL measurements and detect low-frequency phonon mode.

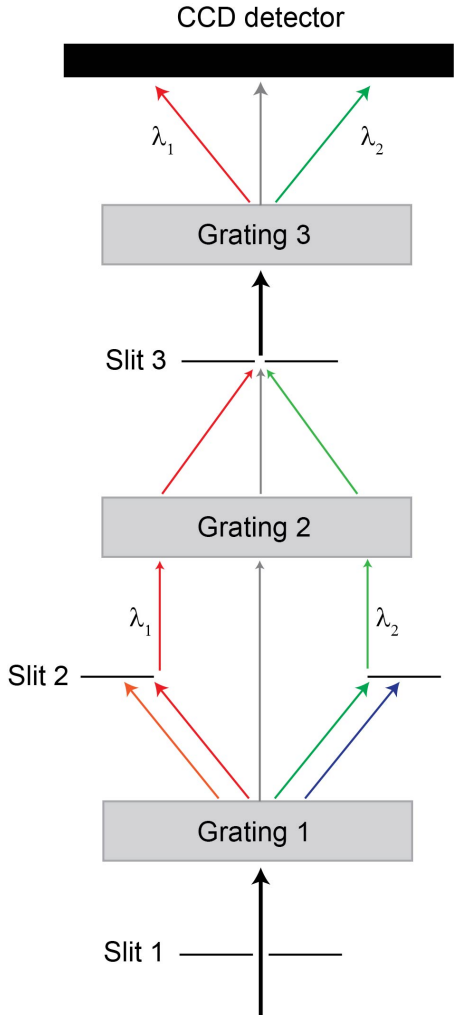

Figure 2.2: Schematic illustration of a triple-grating spectrometer. Grating 1 and 2 together with the Slit 2 work as a bandpass filter to allow a window of light with wavelength in the range of λ_1 and λ_2 to pass.

2.2 Photoluminescence Excitation Spectroscopy

As a specific type of photoluminescence technique, photoluminescence excitation (PLE) spectroscopy is used where the energy of the excitation light is varied and the typical emission feature of the material is monitored. After the light absorption, the photoexcited carriers will relax towards lower energy states and reach a quasi-equilibrium with the lattice temperature, during which multiple scattering processes happen such as

carrier-carrier and carrier-phonon interaction. One would expect that the carriers will "forget" how they are created rapidly after the relaxation process, that is, the information on the absorption. However, the PL emission intensity I_{em} is related with the excitation intensity I_{exc} given by:

$$I_{em} = P_{abs} P_{rel} P_{em} I_{exc}, \tag{2.1}$$

where P_{abs}, P_{rel}, P_{em} denote, respectively, the absorption probability of an incident photon, the probability that the carriers will relax to the emission states, and the probability of radiative recombination for those states. P_{em} can be assumed as a constant while P_{rel} mainly depends on the kinetic energy of carriers after excitation. In high-quality sample, the photoexcited carriers relax their energy mainly via carrier-carrier, carrier-phonon scattering processes instead of being trapped by defects or nonradiative recombination. Typically the relaxation processes occur on subpicosecond and picosecond time scales, which are significantly shorter than the radiative lifetime of the PL emission (tens of picoseconds or even longer). Therefore, P_{rel} can be regarded as unity and independent of the kinetic energy of carriers. In this sense, the PLE can be correlated with absorption spectra as

$$I_{em}(\hbar\omega) \propto P_{abs}(\hbar\omega). \tag{2.2}$$

Figure 2.3 shows the PLE spectra for TMDs monolayers [12]. The PLE spectra are monitored by the integrated A exciton emission in the PL spectra at each excitation energy. In general, the profiles of the PLE spectra follow their absorption profiles ($\Delta R/R$). Therefore, PLE spectroscopy is a useful technique to study the electronic transitions of materials with low absorption by measuring the relatively strong PL emission instead.

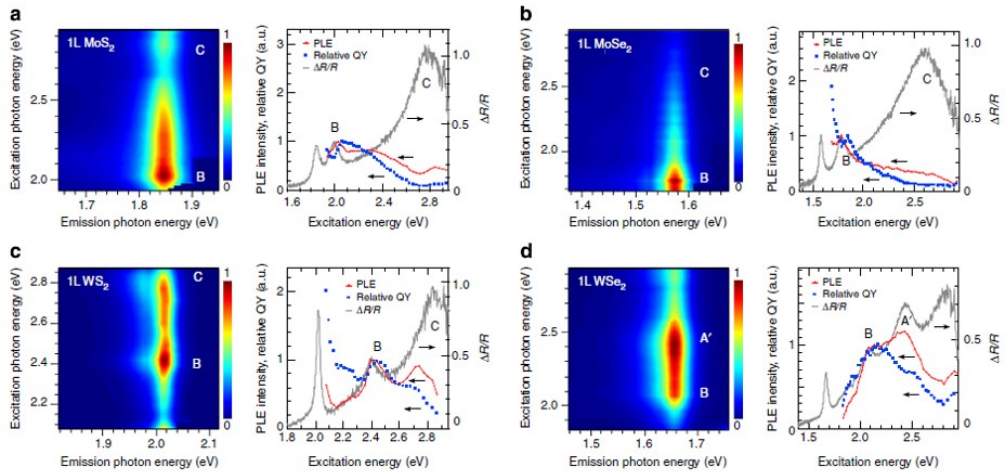

Figure 2.3: PLE spectra for TMDs monolayers. PLE intensity map (left panel), PLE spectra and differential reflectance spectra (right panel) for monolayer (a) MoS_2, (b) $MoSe_2$, (c) WS_2 and (d) WSe_2. The relative quantum yields (QY) of emission are also calculated for comparison. The PLE spectra are monitored by the integrated A exciton emission in the PL spectra at each excitation energy. All the PLE spectra are normalized by the B exciton peak. [12]

2.2.1 Near-resonance Excitation

When the excitation energy is tuned to be in near resonance the electronic band transition, the PLE spectra will be greatly changed, from which important electron-phonon scattering processes can be resolved. It is also referred as resonant Raman spectroscopy. Herein, I will review the quantum mechanics used to describe the microscopic theory of such scattering processes.

In principle, the scattering processes involve the states of three systems: incident photons (with energy $\hbar\omega_i$) and scattered photons ($\hbar\omega_s$), electrons in the material, the phonons involved in the scattering. The scattering process undergoes three steps: (i) the incident photons excite semiconductors into a virtual state by creating electron-hole pairs, which is denoted by the electron-radiation interaction Hamiltonian H_{eR}. (ii) The electrons (or holes) are scattered by phonons into another state via electron-phonon interaction, denoted by Hamiltonian H_{e-ph}. (iii) The scattered electron-hole pairs radiatively recombine and emit the scattered photons. The scattering probability for the transition from the initial state $\langle i|$ to the final state $|f\rangle$ can be calculated via the

Fermi's golden rule by [18]:

$$P_{ph}(\omega_s) = \left(\frac{2\pi}{\hbar}\right) \left| \sum_{n,n'} \frac{\langle i| H_{eR}(\omega_s) \left|n'\right\rangle \left\langle n'\right| H_{e-ph} |n\rangle \langle n| H_{eR}(\omega_i) |i\rangle}{[\hbar\omega_i - (E_n - E_i)][\hbar\omega_i - \hbar\omega_0 - (E_{n'} - E_i)]} \right|^2 \times \delta[\hbar\omega_i - \hbar\omega_0 - \hbar\omega_s], \tag{2.3}$$

where n and $n^{'}$ denotes all the intermediate states, $\hbar\omega_0$ the phonon energy, E_i the initial state energy, E_n the energy of intermediate electronic states. The term $\delta[\hbar\omega_i - \hbar\omega_0 - \hbar\omega_s]$ represents the energy conservation of Raman scattering. It is noted that the electrons do not change after the scattering process. Therefore, the final state $|f\rangle$ should be identical to the initial state $\langle i|$, which has been replaced in Equation 2.3.

The scattering probability provides the information of electron-radiation interaction, electron-phonon interaction and the electronic band structure. However, due to too many intermediate states, Equation 2.3 is difficult to calculate. It becomes feasible only if by tuning the incident photon energy to resonate with the electron interband transition resonance, which involves only one or small number of states. Under resonant condition, Equation 2.3 can be approximated by:

$$P_{ph}(\omega_i) \approx \left(\frac{2\pi}{\hbar}\right) \left| \frac{\langle i| H_{eR}(\omega_s) |a\rangle \langle a| H_{e-ph} |b\rangle \langle b| H_{eR}(\omega_i) |i\rangle}{(E_0 - \hbar\omega_i)(E_0 - \hbar\omega_s)} \right|^2, \tag{2.4}$$

where E_0 denotes the energy of electronic resonance. To avoid the divergence of Equation 2.4, it needs to introduce a damping term into the electronic state E_a by $E_a - i\Gamma_a$ due to its radiative and nonradiative decay processes, where the damping term Γ_a is related to a finite lifetime τ_a by $\Gamma_a = \hbar/\tau_a$. Thus, the scattering probability is given by:

$$P_{ph} \approx \left(\frac{2\pi}{\hbar}\right) \left| \frac{\langle i| H_{eR}(\omega_s) |a\rangle \langle a| H_{e-ph} |b\rangle \langle b| H_{eR}(\omega_i) |i\rangle}{(E_0 - \hbar\omega_i - i\Gamma_0)(E_0 - \hbar\omega_s - i\Gamma_0)} \right|^2. \tag{2.5}$$

In principle, the probability of scattering events in resonance with excitons depends on the exciton oscillator strength and its lifetime. Therefore, to measure the scattered photon intensity as a function of the incident photon energy near the exciton resonance, we are able to extract important information about excitons such as the exciton energy, oscillator strength and exciton lifetime.

Chapter 3

Sample Fabrication

Since the graphene was first obtained in 2004 [30], mechanical exfoliation has been widely used to fabricate atomically-thin 2D materials. By using standard dry transfer technique, different 2D materials can be stacked together to form heterostructures which exhibit novel optical properties. By fabricating a TMDs monolayer field-effect transistor (FET) device with electron beam lithography (EBL), the charge density or the Fermi level of electrons in the TMDs monolayer can be tuned via electrostatic doping. In this chapter, all the fabrication processes used throughout this thesis will be described.

3.1 Mechanical Exfoliation

The structures of 2D crystals are formed with stacking layers that interact with their adjacent ones via van der Waals (vdW) forces. This feature enables us to exfoliate layers from its bulk counterpart by simply using adhesive tapes as shown in Figure 3.1. The first step is to press the adhesive tape against the 2D crystal to attach the top layers. Next, the tape is lifted to exfoliate few layers off the 2D crystal and then pressed against the substrate (SiO_2 for example). After peeling off the tape, bottom layer could be left on the substrate. It is noted that good crystallinity of the 2D crystal is the key factor to exfoliate large monolayers instead of breaking them into pieces.

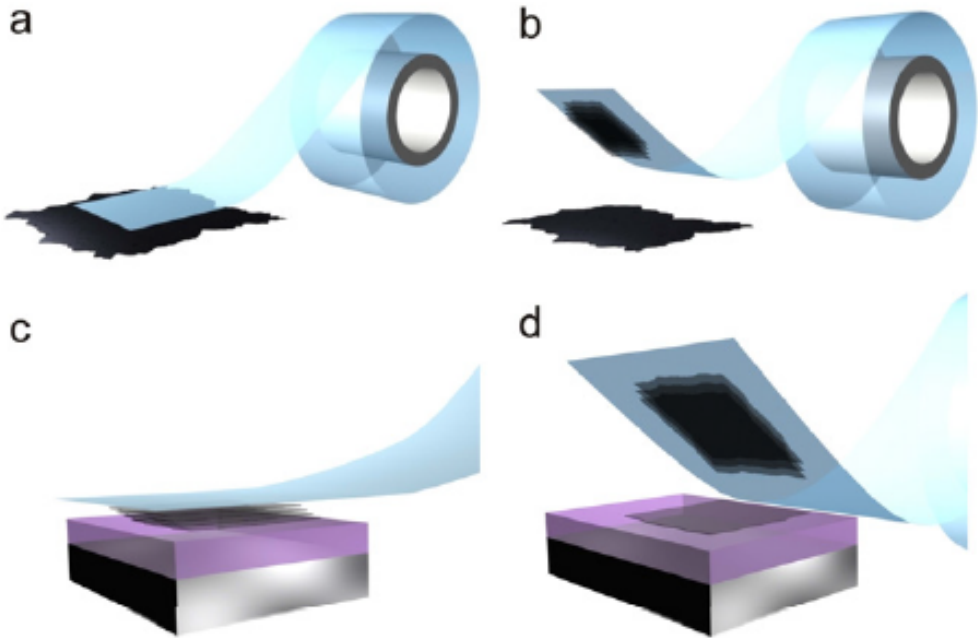

Figure 3.1: Mechanical exfoliation of 2D crystals. (a) Adhesive tape is pressed against the 2D crystal to attach the top layers. (b) Lift the tape to exfoliate few layers off the 2D crystal. (c) Press the tape with few layers against the substrate. (d) After peeling off the tape, bottom layer could be left on the substrate. [13]

To distinguish whether the layer is monolayer or not, some simple skills are needed for identification. A common practice is to identify monolayers via the optical contrast under an optical microscope, especially on Si substrate capped with SiO_2 layer. Figure 3.2(a) shows the optical image of exfoliated monolayer WS_2 and its bulk crystal on a Si substrate with 285 nm-thick SiO_2 layer. The shallow-blue monolayer clearly distinguishes itself from its colorful bulk counterpart and the deep-blue substrate. This practice is an experimental skill, which can serve as a preliminary test. For MoX_2 and WX_2 compounds (X= S, Se), it is further confirmed by its fluorescence image. When thinning down to monolayer, the TMDs monolayers being studied experience a transition from indirect bandgap to direct bandgap, giving rise to strong light emission upon external excitation. As shown in Figure 3.2(b), the region labeled WS_2 monolayer shows strong red-light emission while its bulk counterpart does not when excited with a UV lamp.

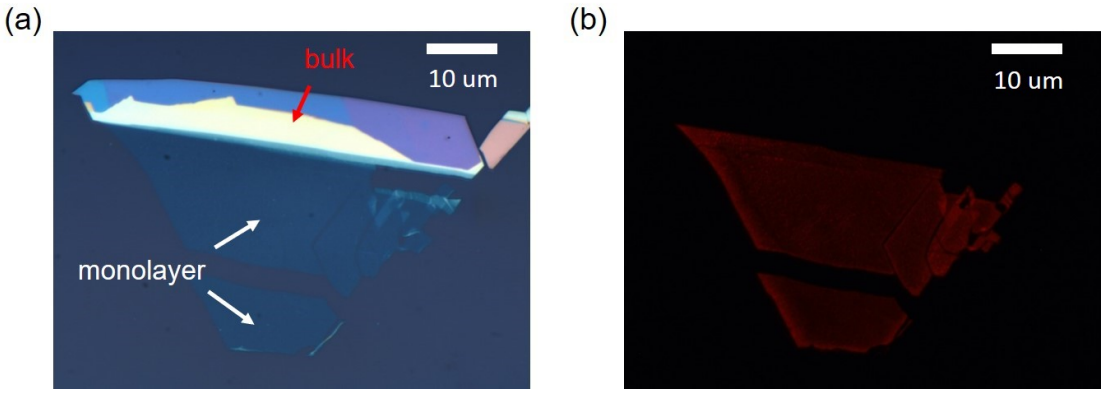

Figure 3.2: Identification of monolayers. (a) Optical image of exfoliated monolayer WS_2 and its bulk crystal on a Si substrate with 285 nm-thick SiO_2 layer. (b) Fluorescence image of WS_2 excited by a UV lamp.

This technique applies to good visible-light emitters for convenient confirmation. Other techniques such as atomic force microscopy (AFM) and Raman spectroscopy are also available ways to identify the thickness of exfoliated layers, which can apply to the general 2D materials.

3.2 Dry Transfer of Two-dimensional Materials for Fabricating Heterostructures

The fabrication of heterostructures achieves the design of artificial lattice structure by stacking 2D materials. It requires the deterministic transfer of mono- or few layers that are obtained by mechanical exfoliation. The most-widely-used method is the all-dry transfer that relies on viscoelastic stamps [14]. Figure 3.3(a) shows the schematic of the setup for dry transfer. It consists of a microscope for monitoring the sample position and a stamping stage for controlling the sample position during the transfer process.

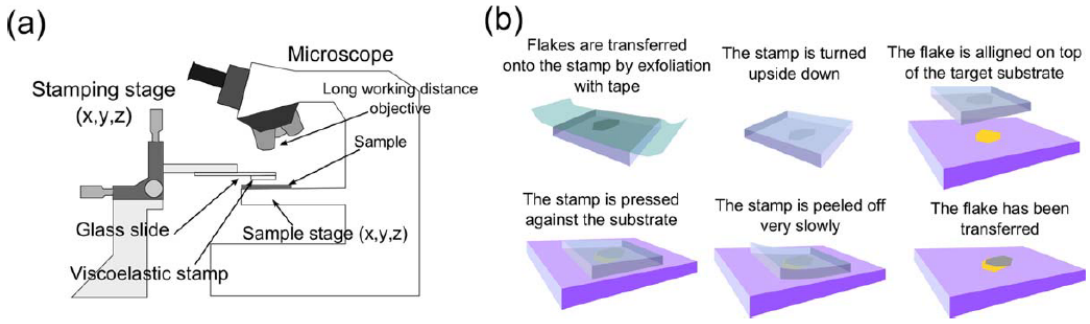

Figure 3.3: Dry transfer setup and processes. (a) Schematic illustration of the setup for dry transfer. It includes a microscope for monitoring the sample position and a stamping stage for controlling the sample position. (b) Diagram of process to transfer exfoliated flakes onto a designated location. [14]

The transfer process, as shown in Figure 3.3(b) [14], can be divided into the following steps: First, flakes on the tapes are transferred onto one side of the stamp (Polydimethylsiloxane, a transparent polymer stamp used in our case); The stamp is turned upside down and sticks to a glass slide; The flake is aligned and pressed against the target substrate monitored under the microscope; Then, the stamp is peeled off very slowly to avoid breaking the flake, leaving the flake on top of the substrate. To make the high-quality heterostructure, it is important to avoid contamination of the sample surface during the transfer process. The dry-transfer technique is used in this thesis to fabricate the hBN-encapsulated WS_2 and MoS_2 monolayer, which will be shown in Chapter 5.

3.3 Device Fabrication

To tune the charge density in 2D materials, field-effect transistor (FET) devices are fabricated for both hBN-encapsulated WS_2 and MoS_2 monolayer via the electron beam lithography (EBL). In our FET device, we choose the back-gate device with 285 nm SiO_2 layer as the insulating layer, which gives a weak leakage current. The device fabrication process is summarized in Figure 3.4.

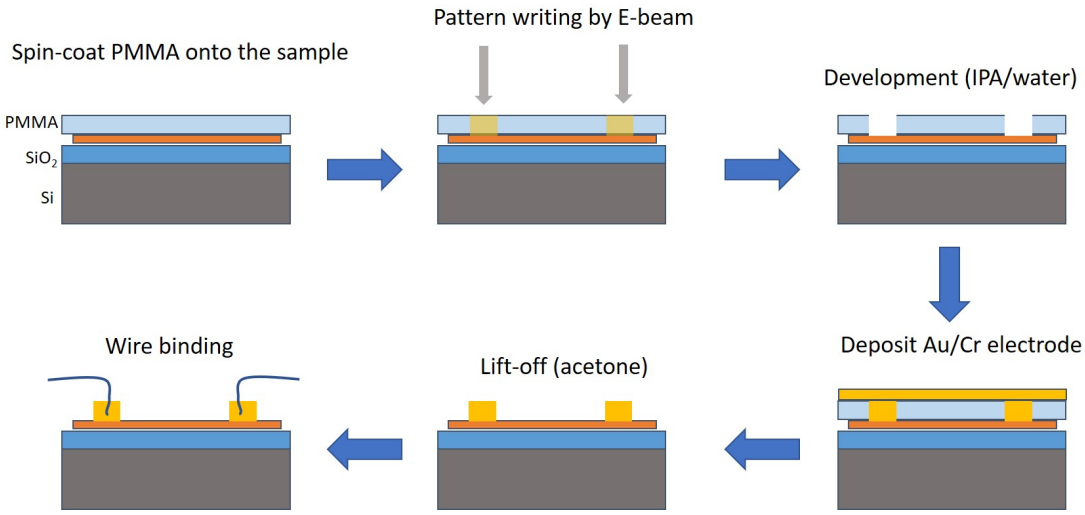

Figure 3.4: Schematic of FET device fabrication process.

After the transfer of exfoliated flakes onto the Si substrate with 285 nm SiO_2 layer, a PMMA resist is spin-coated onto the substrate and sample surface at 4000 rpm for 60 seconds. Then, it is baked on a hot plate (180 °C) for 5 minutes. The next step is the EBL exposure. It is separated into two steps. The first step is to write the marker to locate the sample. After the e-beam exposure, the sample is developed for 40 seconds in the developer solution (a mixture of methyl isobutyl ketone (MIBK) and Isopropyl alcohol (IPA) water by the ratio of 3 : 1. It is rinsed by IPA and blown dry with a nitrogen gun. To locate the relative position of the flakes and the marker, it needs to take photos of the sample image under a microscope for the reference of EBL exposure in the next step. The second step is to write the electrode pattern on the flakes, followed by the same development process. Then the sample is placed into a thermal evaporator to deposit metal materials for the electrode. The materials are chosen as 50 nm Au and 5 nm Cr for better electrical contract with the flakes. Finally, the sample is put into acetone solution to lift off the PMMA layer for ∼30 minutes.

Chapter 4

Probing Momentum-Indirect Excitons by Near-Resonance Photoluminescence Excitation Spectroscopy in WS_2 Monolayer

4.1 Introduction

Atomically thin layers of group-VI transition metal dichalcogenides (TMDs) such as MX_2 (M = Mo, W; X = S, Se) and hexagonal lattice feature prominent exciton properties and spin-valley physics. As a result of strong quantum- and dielectric confinement in single atomic layer of TMD materials, the photoexcited electrons and holes are tightly bound via Coulomb interaction to form excitons with the binding energy of hundreds meV [6, 31–35]. The large exciton binding energies reinforce the stability of exciton complexes such as charged excitons (trions) [8,25,36,37] and biexcitons [37–39] that offers great opportunities to study many-body physics. In addition, the inversion symmetry breaking in TMDs monolayers gives rise to the energy-degenerate but non-equivalent $K/K^{'}$ valleys, which are coupled with electron spins [5]. This unique spin-valley coupling enables the use of light helicity to selectively excite valley excitons at K or $K^{'}$ valley [5], making TMD monolayers ideal candidates for opto-valleytronic applications [5, 21, 40].

The presence of neutral excitons and trions has been widely observed in previous optical studies on TMD monolayers [3, 8, 25]. The substitution of the metal element M, $e.g.$, W into Mo, reverses the energetic order of the optically allowed (bright) and optically forbidden (dark) states at the $K/K^{'}$ valley [24]. In particular, W-based monolayers harness the dark exciton band lying at lower energy than the bright band, leading to the poor emission efficiency at low temperature [38]. Instead, the photoluminescence spectrum of WX_2 monolayer is dominated by several features arising at the low-energy side of the exciton energies, which is currently under intense debate among defects,

bound excitons and biexcitons [37, 38]. For example, the strongest peak that lies below the charged exciton (trion) was previously assigned to biexciton emission [37, 38]. However, the discrepancy lies in that the PL intensity of that peak shows a sub-quadratic increase with excitation power and the binding energy ($\sim$52 meV) [38] is much larger than the theoretically predicted value $\sim$20 meV [41–45]. In addition, the energies of lower energy features in WX_2 monolayers coincidently match the calculated momentum-indirect exciton transitions, which arises from the recombination of electrons and holes in different valleys [46–52], suggesting a more complicated nature of these low-energy peaks. Therefore, a detailed investigation on the exciton dynamics of WX_2 material is needed.

In this chapter, by using photoluminescence excitation spectroscopy, we probe the momentum-indirect transition in WS_2 monolayers that could explain the low-energy features in the photoluminescence spectrum of W-based compounds. Under near-resonant excitation condition, multiple scattering processes between excitons and phonons carrying non-zero wavevector are revealed, indicating the presence of indirect excitons whose constituent electrons and holes locate at different valleys, beside the well-understood direct excitons with their electrons and holes located at the same valley. Furthermore, we find that phonon scattering contributes to valley depolarization during hot exciton relaxation. Our results advance non-trivially the fundamental understanding of the photoluminescence spectra of W-based monolayers that can shed light to intrinsic exciton properties in TMD monolayer semiconductors.

4.2 Sample and Optical Characterization of WS_2 Monolayer.

The high-quality monolayers of WS_2 were prepared by mechanical exfoliation onto a Si/SiO_2 substrate and extensively characterized by optical spectroscopy at cryogenic temperatures (T = 20 K). Figure 4.1(a) shows the reflectance-contrast spectrum, in which, three sharp resonances are clearly resolved. Specifically, the features arising at $\sim$2.09 eV and $\sim$2.50 eV are attributed to A-exciton (X_A) and B-exciton (X_B) whose constituent electrons and holes are excited at K or $K^{'}$ valleys in the Brillouin zone [3,4,21,31]. The energy splitting of $\sim$400 meV between A and B originates from the spin-splitting of the valence band at K and $K^{'}$ points [4, 21, 31]. In addition, the energy structure observed

at ∼2.06 eV is ascribed to a charged exciton state (trion), which is formed by the neutral A-exciton and a free charge (electron or hole) [8, 25, 36, 37].

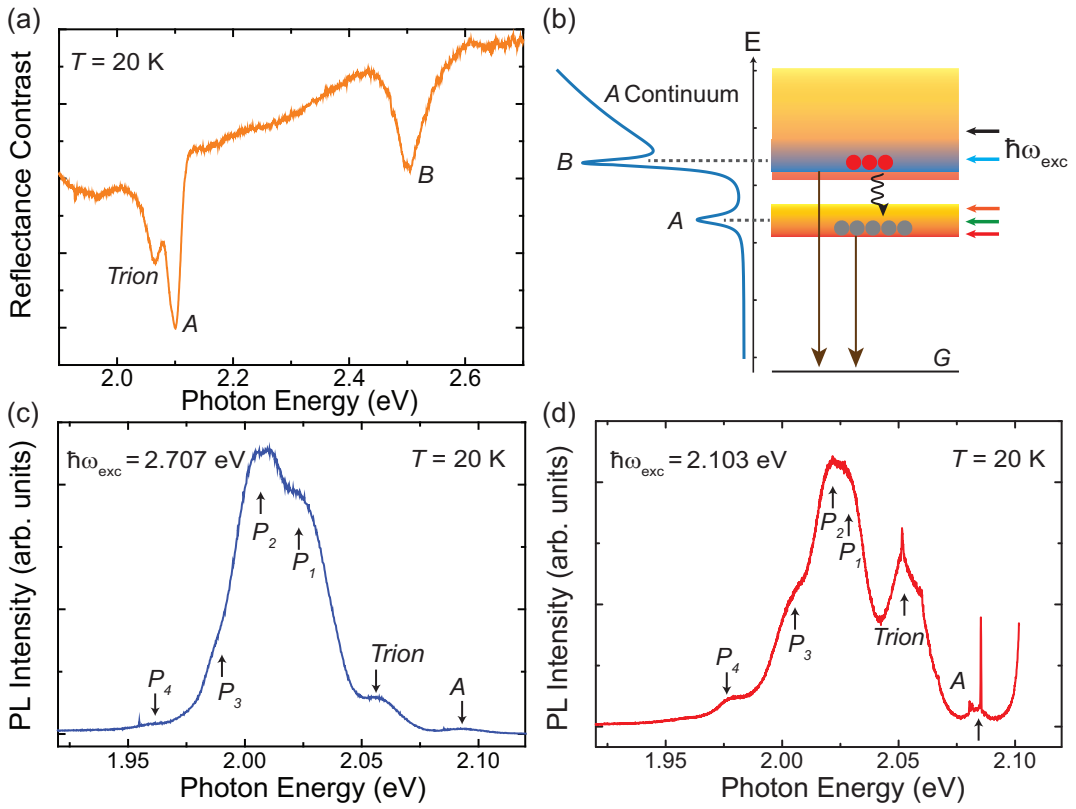

Figure 4.1: Optical characterization of WS_2 monolayer. (a) Reflectance contrast spectrum. Three resonances corresponding to trion, A-exciton and B-exciton are clearly resolved. (b) Schematic energy diagram illustrating the absorption energy positions of A-exciton, B-exciton and continuum of A. The photo-generated carriers/excitons can relax to the lower-energy states via phonon scattering (wavy arrow) or directly recombine (straight arrows). The exciton formation, relaxation and recombination were monitored by varying the laser-excitation energy across the electronic bands (coloured arrows). Representative photoluminescence spectra taken with the excitation energies of (c) (off-resonance) 2.707 eV and (d) (near-resonance) 2.103 eV.

A schematic diagram of the energy structure of WS_2 monolayer is illustrated in Figure 4.1(b). The energy positions of A-exciton and B-exciton are taken from the reflectance measurement. The continuum band of A-exciton is located at ∼2.44 eV [6], which is close to the energy of B-exciton. The existence of different electronic states around the energy of A-exciton and B-exciton suggests nontrivial exciton behaviors, especially under near-resonant excitation conditions. For example, with excitation energies of ∼2.5 eV (see the black arrows in Figure 4.1(b)), excitons can be directly generated at B resonance or free carriers are created at the continuum of A. In the first case, B-excitons

can either radiatively recombine in a so-called hot luminescence process [3, 53–55], or relax non-radiatively to X_A^Γ (A-exciton with zero center-of-mass momentum). On the other hand, when free carriers are generated at the continuum of A, an electron and a hole can relax and later bind together to form exciton at A to result in photoluminescence. Alternatively, when the excitation energy is well below 2.45 eV (see the red, green, orange arrows in Figure 4.1(b)), X_A^Γ excitons are directly generated and later radiatively recombine. Here the exciton formation, relaxation and recombination processes in WS_2 are intensively investigated by varying the excitation energy across the resonances.

Figure 4.1(c) presents the low-temperature photoluminescence spectrum under $\hbar\omega_{\mathrm{exc}}$ = 2.707 eV excitation. Several optical features are resolved, including the radiative recombination of the neutral A-exciton ($\sim$2.09 eV) and the charged state trion ($\sim$2.06 eV). The energy positions are in good agreement with the reflectance contrast spectrum shown in Figure 4.1(a). Interestingly, the PL spectrum is dominated by very intense features (P_i) at the low-energy side of the trion, where the light-absorption is negligible. The origin of the peaks P_i (especially P_1 and P_2) is currently under debate, which will be discussed later in this chapter. On the other hand, when the excitation energy is tuned close to the resonance A ($\hbar\omega_{\mathrm{exc}}$ = 2.103 eV), additional sharp features are resolved on top of A-exciton. The behaviors of these emission features are carefully monitored while varying the excitation energy from 2.103 to 2.707 eV across the A and B resonances.

4.3 PLE with Near-Resonant Excitation of A Excitons.

In the case of the A resonance, up to eighteen excitation energies from a continuous tunable laser ranging from 2.103 to 2.173 eV are used to excite the WS_2 monolayer, as shown in Figure 4.2. In the vicinity of A resonance, sharp features labeled by X_1 to X_8 are resolved on top of A-exciton with the linewidth of $\sim$0.4 meV. The origin of these peaks arises from the exciton-phonon scattering events, as will be discussed in this section.

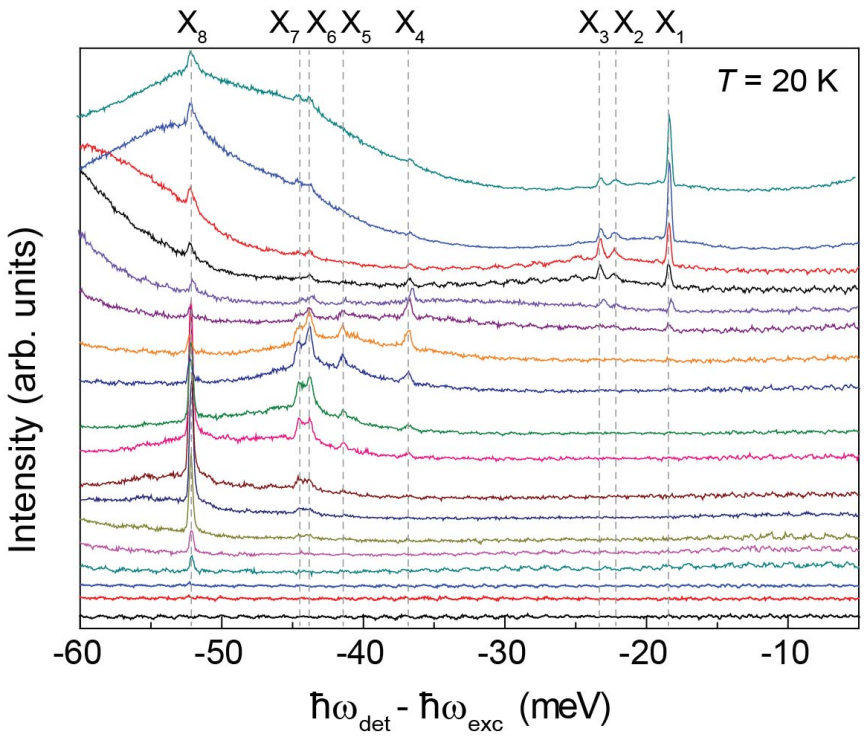

Figure 4.2: Photoluminescence spectra with excitation near A-excitons. Eighteen excitation energies from a continuous tunable laser ranging from 2.103 to 2.173 eV (from up to bottom) are used to excite the WS_2 monolayer. The spectra are plotted relative to the laser excitation energy. Sharp features labeled by X_1 to X_8 are resolved on top of A-exciton with the linewidth of $\sim$0.4 meV.

4.3.1 Identification of Exciton-Phonon Scattering Processes.

Figure 4.3(a) shows PL spectra acquired with selected excitation energies of 2.103 eV, 2.111 eV, 2.125 eV and 2.136 eV. All the spectra are plotted relative to the energy position of the zero phonon line of X_A^Γ (ZPL X_A^Γ), which corresponds to the direct transition of excitons with zero center-of-mass momentum and is independent of excitation energy. On the other hand, the narrow features clearly shift while changing the excitation conditions. For instance, while changing $\hbar\omega_{\text{exc}}$ closer to the A resonance, from 2.136 eV (top panel) to 2.111 eV (middle panel), the peak marked by blue arrow (later identified as $2LA(M)$) shifts in accordance with the excitation. The rigid shift of the peak position with excitation energy together with the narrow linewidth approaching the resolution limit, are typically observed in scattering processes between carriers/excitons and phonons that is usually referred to as resonant Raman scattering [18]. We, therefore, attribute these features to near-resonant scattering events between exciton and different phonon modes of monolayer WS_2, which exhibit much richer information than previous non-resonant Raman study [56–58].

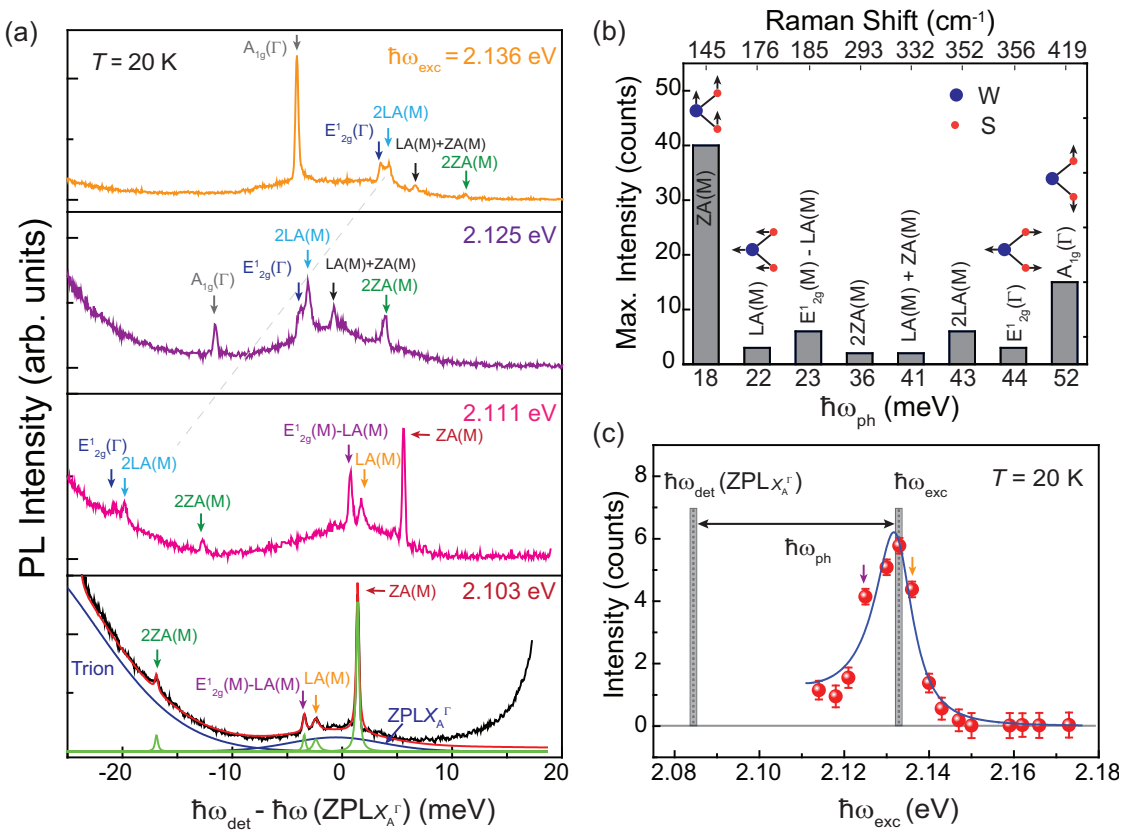

Figure 4.3: Photoluminescence excitation spectroscopy near A resonance in WS_2 monolayer. (a) Selected low-temperature (T = 20 K) PL spectra obtained with different excitation energy. The sharp features are labeled according to the energies of the different phonon modes that are involved in the exciton-phonon scattering event. The dashed-line illustrates the evolution of the $2LA(M)$ mode as the excitation energy varies, taken as a representative example. In the bottom panel, an illustrative fitting procedure to the PL lineshape (black solid-line) is shown. Voigt functions are used to model each of the different peaks, where the blue solid-curve centred at zero represents the ZPL X_A^Γ. Green solid-lines indicate scattering events between excitons and phonons, while red solid-curve is the cumulative fitting of all curves. (b) The identified phonon energies and their maximum intensity over all excitations. The typical lattice vibrational modes are depicted where blue (red) circles represent W (S) atoms. Arrows indicate the direction of atomic motion for each vibration mode. (c) The obtained excitation intensity profile of $2LA(M)$ mode is shown as a representative case. The orange and purple arrow indicate the excitation energy position of 2.136 eV and 2.125 eV used in (a). The solid curve is the fitting to the profile by using Equation (1). The data points are plotted with excitation energies ranging from 2.114 eV to 2.173 eV, as in this energy range the resonance condition is achieved between $2LA(M)$ phonons and neutral X_A^Γ excitons.

In total, we identify up to eight modes from Figure 4.2, whose energies match well with recent resonant Raman studies [59–61] and theoretical calculations [62] as listed in Table 4.1. The first-order optical modes $A_{1g}(\Gamma)$ and $E^1_{2g}(\Gamma)$ are located at the Brillouin

Table 4.1: Phonon Modes Identification

Peak	Phonon modes	Phonon Energy (meV)	Raman shift (cm^{-1})
X_8	$A_{1g}(\Gamma)$	52	419
X_7	$E^1_{2g}(\Gamma)$	44	356
X_6	2LA(M)	43	352
X_5	LA(M) + ZA(M)	41	332
X_4	2ZA(M)	36	293
X_3	$E^1_{2g}(M)$ - LA(M)	23	185
X_2	LA(M)	22	176
X_1	ZA(M)	18	145

zone center (Γ-point), while the first-order acoustic modes $LA(M)$ and $ZA(M)$ are located at the edge (M-point) of the Brillouin zone. The other four modes are assigned to the linear combinations of different first-order M-point phonons.

4.3.2 Dependence on Excitation Energy of Exciton-Phonon Scattering Intensity.

In addition to the energy shift, the scattering intensity of the all phonon modes also varies drastically with the excitation energy. The lineshape of the PL spectrum has been fitted as shown in the bottom panel of Figure 4.3(a) (2.103 eV excitation). For the fittings, we used Voigt functions to model each of the different peaks, where blue solid-lines refer to excitonic resonances. The Voigt function is given by the convolution between a Lorentzian function and a Gaussian function: $V(\omega;\omega_0,\sigma,\gamma_0) = A\int_a^b G(\omega' - \omega_0;\sigma)L(\omega-\omega';\gamma_0)d\omega'$, $G(\omega;\sigma) = \frac{1}{\sigma\sqrt{2\pi}}exp(-\frac{\omega^2}{2\sigma^2})$, $L(\omega;\gamma_0) = \frac{\gamma_0}{\pi(\omega^2+\gamma_0^2)}$. Specifically, the blue solid-curve centred at zero represents the ZPL X^Γ_A. Green solid-lines indicate scattering events between excitons and phonons, while red solid-curve is the cumulative fitting of all curves. From the fitting, the intensities of individual features are extracted (all the spectra are normalized by excitation power). The fitting procedure is repeated for all the spectra, from which the maximum of scattering intensity for each phonon mode among all excitation energies is given in Figure 4.3(b). Figure 4.3(c) shows the intensity profile of a representative scattering event involving the $2LA(M)$ mode as a function of excitation energy (the complete evolution of strongest $ZA(M)$ mode is not available due to limited excitation wavelength). The intensity profile of the exciton-phonon scattering

events can be well reproduced by using Equation 4.1 [18] :

$$P \propto \left(\frac{2\pi C^2}{\hbar}\right) \frac{1}{|(\hbar\omega_{\mathrm{ZPL}} - \hbar\omega_{\mathrm{exc}} - i\Gamma_{\mathrm{ZPL}})(\hbar\omega_{\mathrm{ZPL}} - \hbar\omega_{\mathrm{det}} - i\Gamma_{\mathrm{ZPL}})|^2} \tag{4.1}$$

where $\hbar$ is the reduced Planck constant, C is the amplitude of the resonant-scattering event, $\hbar\omega_{\mathrm{exc}}$ is the excitation photon energy, $\hbar\omega_{\mathrm{det}}$ the detected/scattered photon energy, $\hbar\omega_{\mathrm{ZPL}}$ the exciton resonance energy, Γ_{ZPL} is a damping constant that is related to the radiative lifetime of the exciton transition. The intensity of the scattering event is maximal at the resonant condition when the difference between the excitation laser and detection photon energy matches the phonon energy ($\hbar\omega_{ph}$), *i.e.*, $\hbar\omega_{exc} - \hbar\omega_{\mathrm{ZPL}_{\mathrm{X}_{\mathrm{A}}^{\Gamma}}} = \hbar\omega_{ph}$ ($\hbar\omega_{det} = \hbar\omega_{\mathrm{ZPL}_{\mathrm{X}_{\mathrm{A}}^{\Gamma}}}$). The fitting parameters are C and Γ_{ZPL}, while the resonance energies of excitons and phonons obtained from the modelling in Figure 4.3(a) are fixed. The extracted Γ_{ZPL} for other phonon modes are shown in Figure 4.4, which approximately have the same value of 4 mev. The fitting results in Γ_{ZPL} = (4$\pm$1) meV corresponding to an exciton radiative lifetime of $\sim$1 ps, which is in excellent agreement with experiments [63] and theoretical calculations [64, 65].

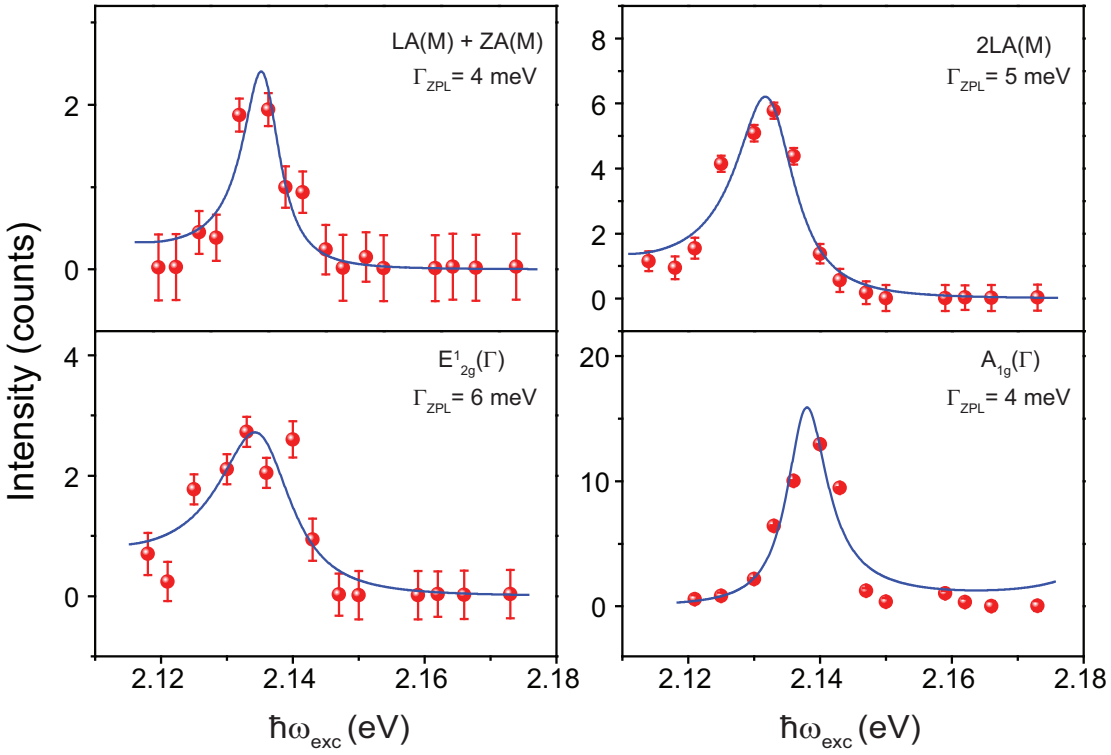

Figure 4.4: The intensity profile as a function of excitation energy for different phonon modes. The Γ_{ZPL} for each phonon mode is extracted from the fitting by Equation 4.1.

Moreover, the strongest scattering intensity among different phonon modes comes

from the scattering with zone-edge phonons (M-point) (see Figure 4.3(b)). Therefore, we highlight that most of the scattering features resolved in our optical spectra involve zone-edge phonons, suggesting that they originate from the collisions between real excitonic states and phonons.

4.3.3 Evidences of Indirect Excitons in WS_2 Monolayer.

Figure 4.5(a) demonstrates the exciton-phonon scattering processes in single-particle (left panel) and exciton (right panel) representations. Excitons are composed of electrons and holes, both of which can be scattered by phonons. The exciton momentum is defined by center-of-mass momentum $\hat{Q}^i_X$ given by the momentum difference between the electrons and holes $\hat{Q}^i_X = \hat{k}^i_e - \hat{k}^i_h$, while the phonon momentum is $\hat{q}^i_{\rm ph}$ (i corresponds to the position in the Brillouin zone). During the events of exciton-photon (light absorption) and exciton-phonon collisions, the momentum is conserved and obeys the relationship $\hat{k}_{\rm photon} = \hat{Q}^i_X + \hat{q}^i_{\rm ph}$.

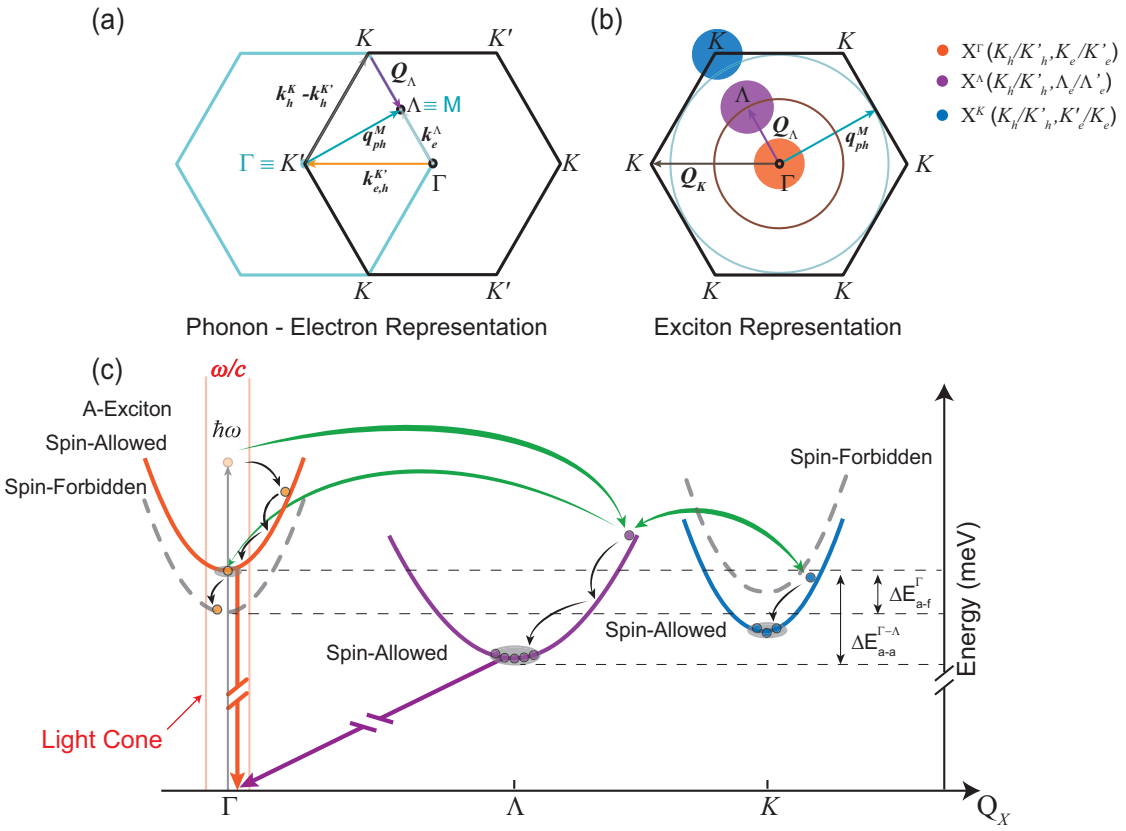

Figure 4.5: Exciton dispersion, formation, relaxation and recombination processes in WS_2 monolayer. (a) Electron-hole picture involving the scattering with M-point phonon. The black hexagon represents the free-particle Brillouin zone. The blue hexagon represents the phonon lattice. It has been shifted to match with the electronic $K^{'}$-valley, where direct photoexcitation takes place in WS_2 monolayer. With the assistance of M-point phonons, photoexcited electrons at $K^{'}$ (K) valley can be scattered into Λ or K $(K^{'})$ valleys, to bind with a scattered (or residing) hole at respectively K $(K^{'})$ or K' (K) valley to form excitons with nonzero wavevector ($\hat{Q}_X^{\Lambda}$ or $\hat{Q}_X^{K}$). (b) The hexagonal Brillouin zone of excitons. The wave vectors for each band are indicated. The coloured legend indicates the valley from where carriers originate to form excitons. (c) Exciton dispersion as a function of its center-of-mass momentum $\hat{Q}_X$. Exciton formation and relaxation are mediated by exciton-phonon scattering. In the electron-electron representation, the dashed curves represent the spin-forbidden (dark) excitons consisting of electrons and holes with opposite spin. The solid line represents spin-allowed (bright) excitons consisting of electrons and holes with the same spin. Green curved arrows indicate for intervalley scattering and formation of excitons. Black curved arrows indicated for intra-valley relaxation. Broken orange arrow represents the optically direct transition from Γ-point exciton band. Broken purple arrow represents the optically indirect transition from Λ-point exciton states. The indirect transition from K-point excitons has been omitted for clarity.

In monolayers TMDs, direct photoexcitation of electrons and holes takes place at K and $K^{'}$ valleys, generating $\hat{Q}_X^{\Gamma}$ excitons (see Figure 4.5). In the following, the generated

carriers are scattered by phonons, involving the zone-center (the Γ-point, $\hat{q}_{\mathrm{ph}}^{\Gamma} \sim 0$) and the zone-edge (the M-point, $\hat{q}_{\mathrm{ph}}^{M} \neq 0$) of the Brillouin phonon zone (see blue hexagon at Figure 4.5(a). Phonons at Γ-point ($\hat{q}_{\mathrm{ph}}^{\Gamma} \sim 0$) scatter the electron-hole pairs generated at the light cone into the zone-centre (Γ-point) of exciton dispersion (see orange symbol and parabola at Figure 4.5(b) and (c)). When only a single phonon mode is involved in the collision, either an electron or a hole is scattered after the photoexcitation. As both electrons and holes have similar effective masses ($m \sim 0.42\mathrm{m}_0$) [66, 67], their first-order phonon-scattering probability is likely comparable, in clear contrast to conventional semiconductors such as II-VI and III-V, in which the exciton scattering is normally dominated by lighter electrons [18]. More interestingly, phonons at the M-point have non-zero momentum ($\hat{q}_{\mathrm{ph}}^{M} \neq 0$), which implies that the virtually generated excitons are scattered out of the light cone to their dispersion at other high-symmetry points in their Brillouin zone to satisfy the momentum conservation $\hat{q}_{\mathrm{ph}}^{M} \sim -\hat{Q}_X$ (see bluish parabolas at Figure 4.5(c)).

We find that the first-order scattering of electron-holes pairs photoexcited at K or $K^{'}$ valleys takes place via two M-point phonons (see Figure 4.3(b)), suggesting that both electrons and holes are scattered to their dispersions. There are several pathways to form an exciton from these carriers in monolayer WS_2, depending on the exact valley where they reside after being scattered. Photoexcited electrons at $K^{'}$ (K)-valleys can be scattered into Λ (Λ$^{'}$)-valleys by one M-phonon because the momentum conservation is satisfied $\hat{k}_e^{K^{'}} - \hat{k}_e^{\Lambda} = \hat{q}_{\mathrm{ph}}^{M}$ (and $\hat{k}_e^{K} - \hat{k}_e^{\Lambda^{'}} = \hat{q}_{\mathrm{ph}}^{M}$). Furthermore, since Λ-valley is an energy minimal [68], the electrons preferentially reside on this band. In other way, the M-phonon could scatter the electron from K ($K^{'}$) to the $K^{'}$ (K) valley. In this case, $\hat{k}_e$-momentum is not strictly satisfied, lowering the probabilities for this scattering channel. For photoexcited holes at $K^{'}$ (K)-valleys, the situation is slightly different. By considering just momentum, they could be scattered to the Λ (Λ$^{'}$)-valley. However, this valley-extrema is hundreds of meV lower in energy that the $K^{'}$ (K)-valence band maxima. Therefore, in our near-resonant excitation conditions, this event is unlikely to take place. Most probably, M-point phonon modes scatter holes from $K^{'}$ (K) to the K ($K^{'}$) valley. Scattering events via M-point phonon modes have been proposed as being responsible for valley depolarization in TMDs [69]. Nonetheless, no direct experimental evidence was yet reported, while the sharp features we observed in Figure 4.3 provide strong evidence for the scattering between exciton and M-point phonons.

4.3.4 Exciton Formation Pathways in WS_2 Monolayer.

Following near resonant photoexcitation and subsequent phonon-scattering by Γ- or M-modes, electrons in monolayer WS_2 can reside at K-, $K^{'}$- and Λ-valleys, while holes can locate mostly at K- and $K^{'}$-valleys. After scattering by zone-center (Γ-point) phonons, tightly bound A-excitons are formed at the Γ-point ($X_A^{\Gamma}, \hat{Q}_X^{\Gamma} = \Gamma$, see Figure 4.5(b)) from photoexcited electrons and holes at the same K- or $K^{'}$-valley. On the other hand, owing to strong electrostatic interactions between electrons and holes in monolayer TMDs, whose large reciprocal Bohr radius $r_B \sim 0.8$ nm^{-1} is about one third of a typical lattice wavevector $k_l \sim 3$ nm^{-1}, the wavefunctions of electrons and holes located at different valleys can spatially overlap to form excitons at Λ-point. For example, after scattering by zone-edge (M-point) phonons, electrons at Λ-valleys bind with holes at the momentum-nearest K-valley to form momentum-indirect excitons at the Λ-point ($X^{\Lambda}, \hat{Q}_X^{\Lambda} = -\Lambda$). Moreover, electrons at the K-valley could bind with holes at the $K^{'}$-valley to form momentum-indirect excitons at the K-point ($X^K, \hat{Q}_X^K = K$).

4.3.5 Light Emission from Momentum-Indirect Transitions in WS_2.

Figure 4.5(c) shows a schematic structure of the lowest-energy exciton bands as a function of the center-of-mass momentum $\hat{Q}_X$. The location of the excitonic valleys, the dispersion of the parabolas and relative energies are reproduced from calculations for excitons in TMD monolayers [50, 51] and from our scattering features with phonons of non-zero wavevector (see Figure 4.3). In W-based monolayers, for $\hat{Q}_X = \Gamma$, two kinds of exciton branches exist due to different spin configurations of electrons and holes. When the electron and hole exhibit the same spin orientation, the resultant exciton transition is spin-allowed (orange solid parabola). In contrast, the opposite spin orientation of the constituent carriers gives rise to the spin-forbidden exciton band (grey dash parabola). For $\hat{Q}_X = K$ (K-valley), the spin configuration is opposite to the exciton at the Γ-valley. Specifically, the spin-forbidden band of X^K energetically lies above the spin-allowed branch. The energy splitting between allowed and forbidden spin-states ($\Delta E_{\mathrm{a-f}}^{\Gamma}$, so-called (spin) bright-dark splitting) varies for different compounds, being $\sim$50 meV as recently reported for W-based monolayers. [7, 50, 70–72] The spin order of each band is reversed in Mo-based monolayers. [7, 24, 70–73] For $\hat{Q}_X^{\Lambda}$ (Λ-valley), the calculated lowest-energy exciton branch is spin-allowed. Interestingly, the momentum-indirect exciton X^{Λ} lies energetically below the momentum-direct X^{Γ}, which is due to the larger

exciton effective mass at Λ-valley [50]. The energy separation between spin-allowed excitons at Γ- and Λ valleys ($\Delta E_{\mathrm{a-a}}^{\Gamma-\Lambda}$) in WS_2 monolayer has been calculated in the range of 70 to 100 meV. [46, 50] The formation of the excitons at Λ-valley is elucidated by the observation of first-order intervalley scattering events assisted by M-point phonons in our near-resonance experiments.

The spin-allowed X_A^{Γ} branch possesses a giant oscillator-strength that allows for a transient decay ($\sim$ 1 ps) of excitons. At the same time, the excitons decay into spin- or momentum-forbidden branches at lower energies of ∼50 meV [7, 50, 70–72] and ∼70 meV [50] respectively, from which the luminescence is nominally forbidden. The complexity of the excitonic landscape determines the light emission properties of two-dimensional W-based semiconductors. The lineshape of the PL spectrum in Figure 4.6 has been fitted by using Voigt functions to model each of the different peaks, where blue solid-lines refer to excitonic resonances, green solid-lines indicate scattering events between excitons and phonons, while red solid-curve is the cumulative fitting of all curves. The parameters obtained from the fitting to the PL spectrum are listed in Table 4.2. The PL spectrum exhibits several features whose origin is currently under intense debate. An overall consensus exists on the high-energy structures, attributed to radiative recombination of the neutral X_A^{Γ} (∼2.09 eV) and its charged state trion T_A^{Γ} (∼2.06 eV), whose energy separation is $\Delta E_{\mathrm{X_A^{\Gamma}-T_A^{\Gamma}}}$ ∼30 meV. However, the largest contribution to the PL spectrum comes from the energy structures lying 50-100 meV below A-exciton (P_1-P_4), at which the light absorption is negligible. They have been attributed to biexciton luminescence [37, 38, 74] and to localized exciton states [75–77]. Similar PL structures have been resolved in boron nitride encapsulated WS_2 (and WSe_2) monolayers, while only excitons and trions are present in MoS_2 (and $MoSe_2$) monolayers [11, 74] that strongly suggests the contribution of intrinsic exciton-states emission into the energy features below the A-exciton.

Table 4.2: Fitting parameters of spectrum with 2.103eV excitation in Figure 4.

Peak	Relative Energy to ZPL X_A^Γ (meV)	Area (counts)	FWFM (meV)
ZPL X_A^Γ	0	267	12
Trion	-30.0	7058	22
P1	-53.7	7441	17
P2	-64.5	12138	16
P3	-79.7	5236	19
P4	-105.3	706	11
ZA(M)	2	120	0.3
LA(M)	-1.9	20	0.6
$E_{2g}^1(M)$ - LA(M)	-2.9	13	0.3
2ZA(M)	-16.4	13	0.3
2LA(M)	-23.5	46	0.5
$E_{2g}^1(\Gamma)$	-24.4	22	0.4
$A_{1g}(\Gamma)$	-31.9	156	1.2

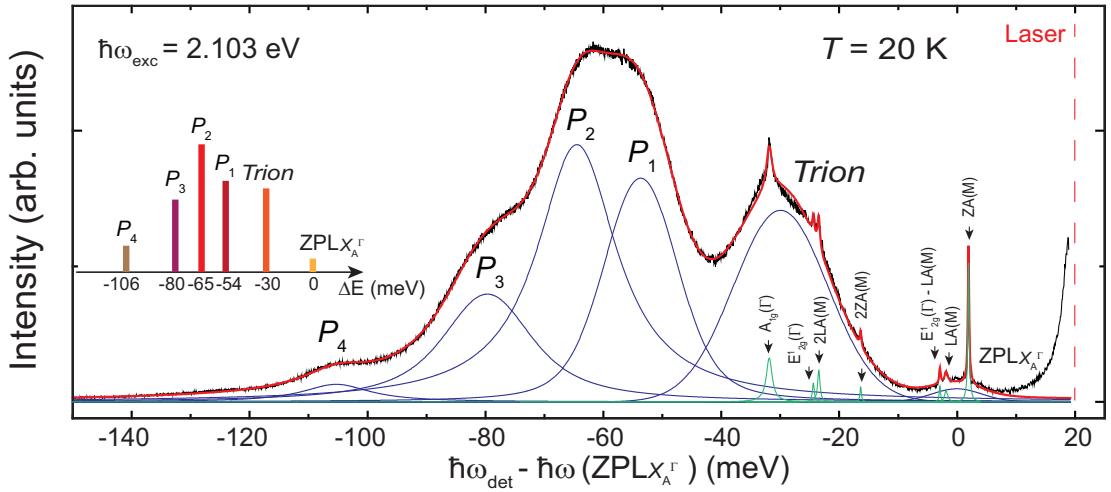

Figure 4.6: Multicomponent fitting of the low-temperature (T = 20 K) PL spectrum in WS_2 monolayer after near-resonant excitation. The PL energy is plotted relative to ZPL X_A^Γ. The raw PL spectrum is shown by the black solid-line, while the red-solid line is the global fitting by using multiple peaks with Voigt lineshapes, indicating for exciton-like (blue solid-lines) and exciton-phonon (green solid-line) scattering processes. The inset shows the relative energy of excitonic-like peaks with respect to the ZPL X_A^Γ. As obtained from the fitting, the height of the color bars indicates the relative contribution of each line to the total PL spectrum.

Our PLE experimental results, otherwise, provide evidence for the indirect nature of

the optical transition from P_1 to P_4. At low temperatures, most of the exciton population resides at the lowest-energy and momentum-indirect exciton at the Λ-point. This is confirmed by the observation of i) first-order scattering events with non-zero wavevector phonons and of ii) weak light emission from the zero-phonon-line X_A^{Γ} ($\mathrm{ZPL_{X_A^{\Gamma}}}$) in our near-resonant excitation experiments. For radiative recombination to take place from the indirect-X^{Λ}, the assistance of phonons, carrier doping or disorder scattering might provide additional momentum to the optical transition. For phonon-assisted recombination, different types and combinations of lattice vibrations might contribute [78], leading to various phonon-assisted features. As a result, several lines are expected at energies $\Delta E_{\mathrm{a-a}}^{\Gamma-\Lambda}$ $\sim$70 meV below the $\mathrm{ZPL_{X_A^{\Gamma}}}$. A peak at energy $\sim \Delta E_{\mathrm{a-a}}^{\Gamma-\Lambda} - n\Delta_{\mathrm{ph}}$ below the $\mathrm{ZPL_{X_A^{\Gamma}}}$, where $n\Delta_{\mathrm{ph}}$ is the energy of the n-phonon mode (n= 1, 2,...) assisting the optical transition.

For light emission arising from the indirect-X^{Λ}, the constituent electrons of these indirect excitons located at the Λ-points (see Fig. 4.5(a)) need to be scattered into the light cone at K- or $K^{'}$-valleys. There could be two possible scenarios. Firstly, with the assistance of zone-edge phonons, electrons at Λ-valleys can be scattered to $K^{'}$-valleys and then recombine with $K^{'}$-valley holes. Due to strong exciton-(zone-edge)-phonon coupling, it might give rise to several phonon replicas. Interestingly, the energy ΔE_1 = $E_{\mathrm{P_1}}$ - $E_{\mathrm{P_3}}$ and ΔE_2 = $E_{\mathrm{P_3}}$ - $E_{\mathrm{P_4}}$ is $\sim$26 meV (1LA(M) $\sim$26 meV) as can be observed in Figure 4.6, suggesting evidences for the phonon-assisted processes. Secondly, it is also possible that electrons at Λ-valleys are scattered to the nearest K-valley to recombine with resident K-valley holes via other type of phonons with non-zero momentum, which could lead to a different emission energy. A way to distinguish between the two recombination pathways would be by investigating the polarization response of the PL spectrum under near-resonant excitation and/or by external magnetic fields.

Interestingly, as reported in previous studies, different substrates could strongly alter the PL spectrum of TMDs monolayers [79–83] and, especially, are important for phonon behaviours of two-dimensional materials [80, 82–87]. Depending on the symmetry of the phonon mode, the substrate could modify both the vibrational energy and/or the electron-phonon coupling strength. It has been reported that the doping levels of the TMD monolayers could vary for different substrates, and such a change on the carrier concentration can influence the atomic motion, leading to slight variations in the phonon energy [80–84]. As a result, different carrier doping and/or substrates might lead to energy shifts of the PL resonances related to the phonon-assisted indirect-exciton X^{Λ}

and a change of the energy separation among their phonon replicas. Another scenario is the modification of the phonon amplitudes by the damping induced by the mismatch in the acoustic impedance between the monolayer and the substrate. It will be particularly relevant for out-of-plane modes. Theoretical and experimental studies have reported the increase in the acoustic phonon relaxation times and charge mobility by ten times for suspended graphene, as compared to graphene on top of silicon dioxide [85–87]. Therefore, we expect different substrates to have dissimilar interfacial interaction, leading to distinct phonon-phonon and electron-phonon coupling strengths. Consequently, the change in the phonon and carrier dynamics might alter the spectral weights of the phonon-assisted resonances.

On the other hand, electrostatic doping might lead to the formation of a negatively charged state of the indirect Λ-exciton or intervalley Λ-trion (T^{Λ}). In a simple scenario, the additional charge would locate at either K or $K^{'}$, depending on the spin-valley configuration (K or $K^{'}$) of the hole to which the Λ electron is bounded. The additional electron will lead to intervalley Coulomb scattering between carriers providing additional momentum and turn the optical transition brighter. The associated peak will appear at the energy of $\sim \Delta E_{\mathrm{a-a}}^{\Gamma-\Lambda} - \Delta_{\mathrm{T}^{\Lambda}}$ below the $\mathrm{ZPL}_{\mathrm{X}_{\mathrm{A}}^{\Gamma}}$. The binding energy $\Delta_{\mathrm{T}^{\Lambda}}$ of the intervalley Λ-trion will be smaller than that of T_A^{Γ}, as the the k-overlap between T^{Λ}-carriers might be smaller.

Therefore, besides the features below $\mathrm{ZPL}_{\mathrm{X}_{\mathrm{A}}^{\Gamma}}$ that have been attributed to luminescence from biexciton and localized states, we argue that a multitude of available radiative recombination pathways of the lowest-energy and indirect-exciton X^{Λ}, might contribute to the low-energy peaks (P_1 to P_4) in the photoluminescence spectrum of WS_2 monolayer. We highlight that multiple phonon-scattering processes could contribute into lines with similar energies, leading to super-linear power-dependence that is often observed in literature [38, 74]. Biexciton emission with a nonquadratic power-dependence ($I_{\mathrm{PL}} = P^{\alpha}$, α ~1.4) in WS_2 monolayers at energies of ~50 meV below $\mathrm{ZPL}_{\mathrm{X}_{\mathrm{A}}^{\Gamma}}$, which largely deviates from theoretical predictions [88], might be reconsidered.

A superlinear emission with excitation power could also be attributed to the increase of the PL quantum efficiency with the increase of excitation power. It is due to the coexistence of nonradiative decay pathways and a nonlinear increase of the radiative recombination efficiency. The nonlinearity could result from the increase of the relaxation rates or from the saturation of the nonradiative channels [89]. Within the drawn picture, it is very likely that the nonlinearity appears due to the saturation of the nonradiative recom-

bination channel of the indirect-exciton X^{Λ}. We believe that future power-dependent time-resolved PL experiments could distinguish the origin of the nonlinearity in the power law of the low-energy structures (P_1-P_4).

4.4 PLE With Near-Resonant Excitation of B Excitons.

Besides the excitation near A exciton, we also investigated the relaxation processes of excitons after resonantly creating B excitons. Specifically, we have monitored the spectral changes on the PL spectra as a function of the excitation photon energy, as shown in Figure 4.7. All the PL spectra are taken with the same excitation power. It can be found that the emission intensity of A exciton varies for different excitation energies. The integrated intensities of A exciton emission are extracted and plotted in Figure 4.9 (blue squares). The excitation intensity profile follows the absorption-like spectrum shown in Figure 4.1(a), showing a resonance at the energy of exciton B. The equivalent profiles suggest the efficient exciton relaxation from B to A.

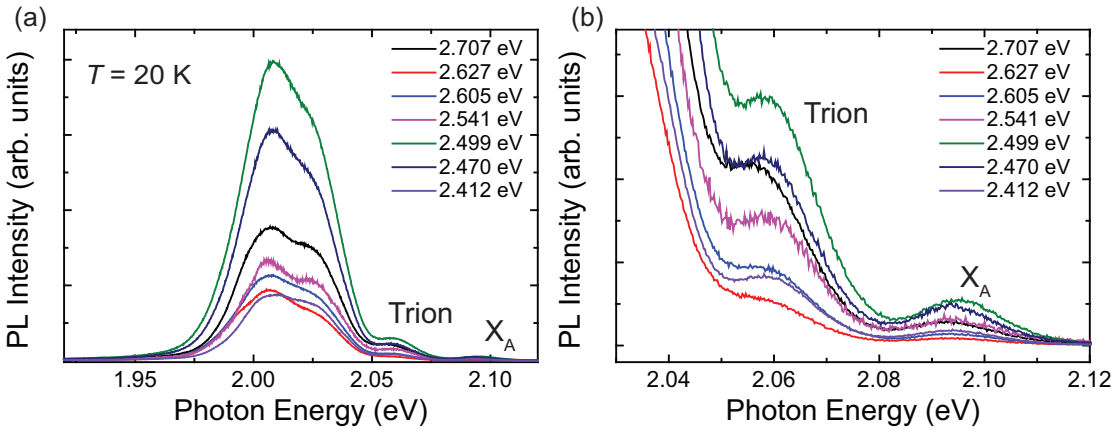

Figure 4.7: Photoluminescence spectra with excitation near B-excitons. (a) Full range PL spectra excited from 2.412 eV to 2.707 eV. (b) Zoon-in spectral range around A exciton emission.

In addition, polarization-resolved PL spectra are taken for four excitation energies as shown in Figure 4.8. Their associated degree of valley polarization (DVP), defined as $\mathrm{DVP} = (\mathrm{I}_{\sigma}^{\pm} - \mathrm{I}_{\sigma}^{\mp})/(\mathrm{I}_{\sigma}^{\pm} + \mathrm{I}_{\sigma}^{\mp})$ after $\sigma^{\pm}$ laser excitation, are calculated and plotted in Figure 4.9 (red circles).

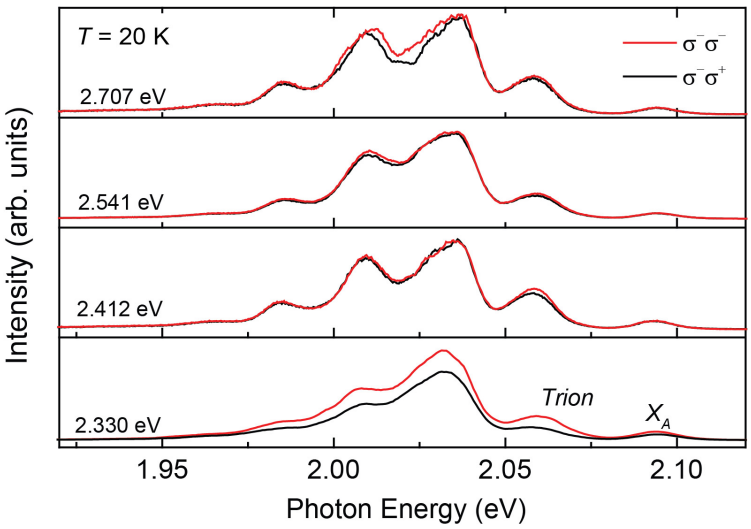

Figure 4.8: Polarization-resolved PL spectra in Monolayer WS_2 at 20 K. The red-color denotes the co-polarized excitation and detection while the black-color denotes the cross-polarized excitation and detection.

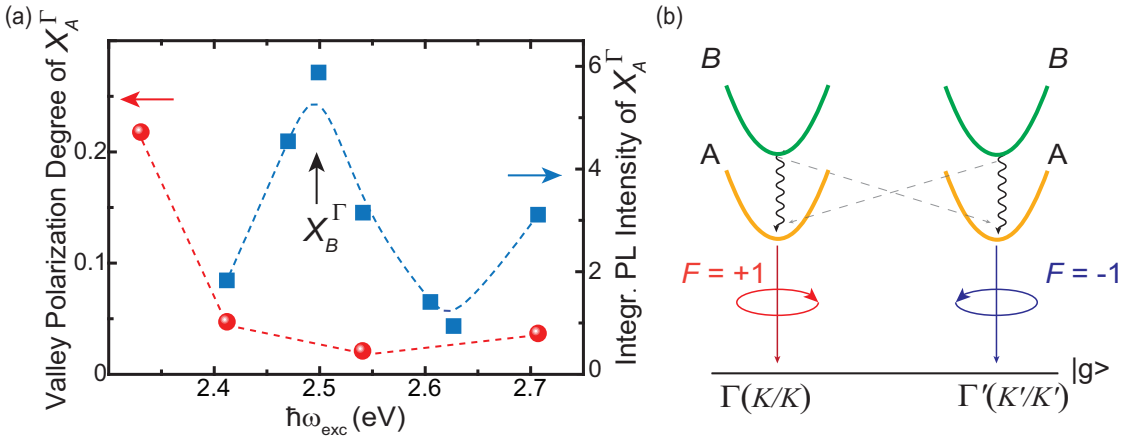

Figure 4.9: Exciton relaxation and valley depolarization under near-resonant excitation of B-excitons. (a) The extracted polarization degree and integrated PL intensity of A as a function of excitation energy. (b) Schematic of excitons relaxation in WS_2 monolayer. F denotes the valley degree of freedom. The generated excitons near B with $\mathrm{F} = +1$ could quickly relax its energy by intravalley scattering (the wavy arrow) to A with $\mathrm{F} = +1$; Relaxation can also happen by intervalley scattering (the dashed arrow) to X_A in the opposite valley with $\mathrm{F} = -1$, leading to the so-called valley depolarization.

In TMDs, A- and B-exciton bands are described by valley-pseudospins $\boldsymbol{\sigma_v}$, whose eigenvalues are $\sigma_v \pm 1$ indicating that electron-hole pairs are photoexcited at $K^{\pm}$ valleys, or alternatively, by a net angular momentum $F_v = \sigma_v$. Therefore, σ^+ (σ^-) polarized light selectively couples to valley A- and B-excitons $F_{\mathrm{K}+}$ ($F_{\mathrm{K}-}$), as schematically shown in Figure 4.9(b). Interestingly, in Figure 4.9(a) we observe that the photogenerated DVP is negligible under resonant excitation with B-excitons and it only increases with

employing lower laser energies. The lack of valley polarization during the fast cooling of B- to A-excitons strongly suggests that intra-valley and inter-valley relaxation are equally probable, causing the valley-pseudospin depolarization of the PL emission.

Intra-valley (inter-valley) processes involve the decay of holes from valence band B to A, while holes flip (preserve) spin and preserve (flip) valley-pseudospin during relaxation. Therefore, several phonons modes are involved in the process. For intra-valley relaxation, zone-center ($i.e.$, Γ-points) modes leading to a hole spin flip are more likely to be involved, while for inter-valley relaxation, zone-edge ($i.e.$, M-point) modes whose symmetry preserves the hole spin will dominate. As the PL emission is depolarized, hole scattering by zone-edge and zone-center phonons might be comparably efficient during the hot exciton relaxation. Therefore, the scattering of hot excitons with zone-edge phonons should be considered as a valley depolarization channel in addition to electron-hole exchange interaction [78].

4.5 Conclusion

In summary, by using near-resonant excitation experiments, we prove exciton-phonon scattering events with non-zero wavevector that provide strong evidence for the momentum-indirect nature of the optical bandgap in WS_2 monolayer. The scattering between carriers and zone-edge phonons creates excitons at different valleys, among which, the lowest-energy band is momentum-indirect. Our findings advance the understanding on the inherent bandgap nature of TMD monolayers and highlight that more efforts are required for a complete understanding of the complex photoluminescence spectrum reported on W-based compounds. In addition to biexciton and localized states, the low-energy emission features observed at low temperature could arise from momentum-indirect transitions. Moreover, further experiments are conducted on high-quality hBN-encapsulated TMD monolayers, as will be discussed in chapter 5. Such samples benefit the clear identification of the different PL resonances. Furthermore, by fabricating a back-gate FET device, the charge density could be tuned to clearly distinguish between charge- and phonon-assisted recombination pathways for momentum-indirect excitons. Finally, one could use magneto-optical spectroscopy to obtain g-factors that might vary across different valley excitons. These further experiments will shed light on the origin of the low-energy features observed in the low-temperature PL spectrum in W-based monolayer semiconductors.

Chapter 5

Observation of a Transition from Charged Indirect-Valley Excitons to Exciton-Plasmon Quasiparticles across the Fermi Edge Singularity in WS_2 Monolayer

Atomically-thin transition metal dichalcogenides (TMDs) feature strongly bound excitons and charged-states due to the strong quantum- and dielectric- confinement effects [6, 8, 25, 31–35]. Combined with their unique spin-valley locking properties [5, 21, 40], they have emerged as ideal platforms to study many-body physics and to explore potential applications in optoelectronic devices, quantum information processing and so on. Recently, there are tremendous studies on the low-temperature PL spectra of W-based monolayers reporting the special excitonic complexes below the neutral exciton emission such as spin-forbidden dark trion state (three particles) [90–92], biexcitons (four particles) [93–97], and charged biexcitons (five particles) [93–97]. All of those features appear at a low doping regime while disappear at elevated electron densities. However, with the Fermi level lifted into the conduction band in W-based monolayers, the spectral features change dramatically, while the understanding of the interaction between photoexcited electron-hole pairs and Fermi electrons remains mysterious yet. Moreover, as we proposed in Chapter 4, the low-energy features below the bright exciton in WS_2 monolayer could result from the momentum-indirect state, with the assistance of either charges or phonons. To confirm such assumptions, better samples with higher optical properties and tunable charge density are needed to perform further experiment.

In this Chapter, I will show the hBN-encapsulated WS_2 monolayer heterostructure with much narrower emission linewidth, which allows us to clearly identify new trion fine structures that are attributed to the charged momentum-indirect Λ-valley excitons. By fabricating the sample into a FET device, the Fermi level of the WS_2 monolayer can be efficiently tuned, during which both the reflectance and PL spectra change dramatically.

More interestingly, at high gate voltages (above 60 V), a feature called Fermi edge singularity is observed in the reflectance and PL spectra, which is ascribed to the exciton-plasmon quasiparticles. The change from the charged indirect Λ-valley excitons to the exciton-plasmon quasiparticles across the Fermi edge singularity could indicate a transition from fermion-like particles to boson-like particles. We demonstrate that the transition happens as a result of combined effect of short range and long range Coulomb potential induced by the Fermi electron gas. Our study provides essential insights into the different interaction mechanisms between the photoexcited electron-hole pairs and the two dimensional Fermi gas. These findings are crucial to understand the complicated PL spectra and many-body physics in TMDs monolayers.

5.1 Sample Characterization of hBN-encapsulated WS_2 Monolayer

The hBN-encapsulated WS_2 monolayer sample shows much different PL spectrum with the bare monolayer on the SiO_2/Si substrate, as shown in Figure 5.1. The differences feature three aspects. First of all, the energy of the neutral exciton X_A has red-shifted $\sim$30 meV from 2.079 eV of the bare WS_2 monolayer on the SiO_2/Si substrate to 2.064 eV of the encapsulated one, which is confirmed by both the reflectance spectra and PL spectra.

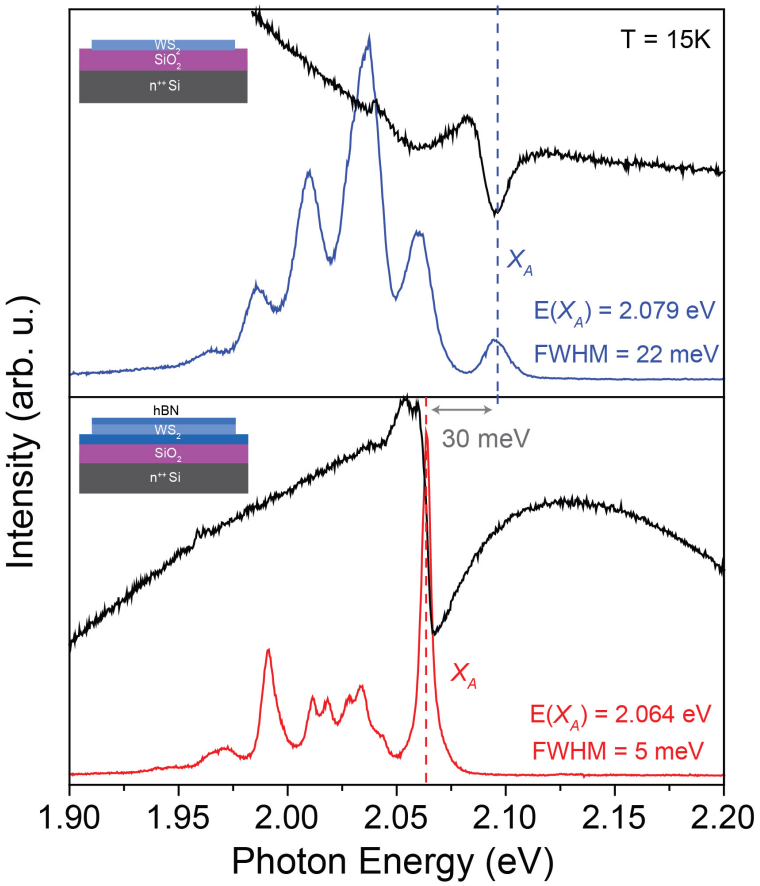

Figure 5.1: The comparison of low-temperature optical spectra for WS_2 on SiO_2/Si substrate and hBN-encapsulated WS_2 monolayer. (a) Reflectance spectrum and PL spectrum for WS_2 on SiO_2/Si substrate. (b) Reflectance spectrum and PL spectrum for the hBN-encapsulated WS_2 heterostructure. The PL spectra are taken with a 532 nm laser excitation at 15 K. The peak position and FWHM of neutral A exciton emission are given in the plot.

The energy shift is caused by the change of dielectric constants at both sides of the monolayer, leading to different dielectric screening effect. The Rydberg exciton states and the exciton binding can be calculated via the Keldysh model [98, 99] in the form of the 2D effective-mass Hamiltonian:

$$H = -\hbar^2\nabla_r^2/2\mu + V_{eh}(r), \tag{5.1}$$

where μ is the reduced exciton mass with $\mu = (m_e^{-1} + m_h^{-1})^{-1}$ and $V_{eh}(r)$ is the 2D nonlocally-screened Coulomb potential [99]. $V_{eh}(r)$ is given by:

$$V_{eh}(r) = -\frac{e^2}{8\epsilon_0\kappa r_0}\left[H_0(\frac{r}{r_0}) - Y_0(\frac{r}{r_0})\right], \tag{5.2}$$

where H_0 and Y_0 are the Struve function and the Bessel function, respectively. The r_0 denotes the screening length and κ the average dielectric constant of the top and bottom layer given by $\kappa = (\epsilon_{top} + \epsilon_{bot})/2$. The κ is ~2.5 for the WS_2 on the SiO_2/Si substrate while ~3.9 for the encapsulated sample. Equation 5.2 indicates that the larger κ leads to a reduced exciton binding energy. In addition, the A exciton shows a 30 meV red shift when κ changes from 2.5 to 3.9, indicating a shrinkage of the renormalized quasiparticle bandgap, as shown in Figure 5.2. To conclude, the increased dielectric constant leads to an enhanced dielectric screening effect, which is accompanied by a shrinkage of the exciton binding energy and quasiparticle bandgap.

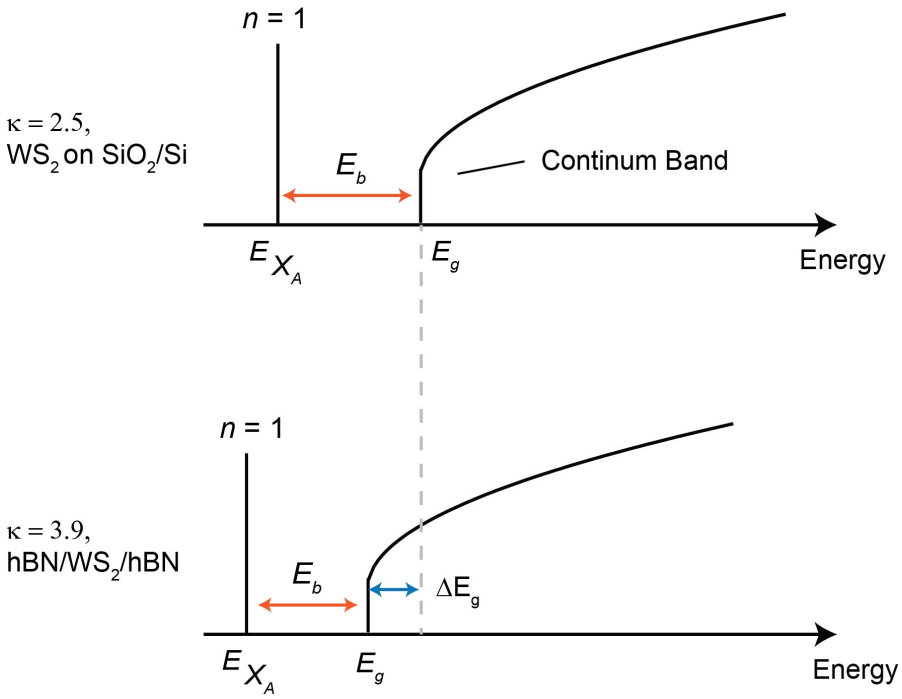

Figure 5.2: Dielectric environment induced electronic structure change. Schematic illustration of a change on the exciton binding energy and continuum band gap for (a) the WS_2 on SiO_2/Si substrate and (b) hBN/WS_2/hBN sample. The increased dielectric constant leads to an enhanced dielectric screening effect, which is accompanied by the shrinkage of exciton binding energy and quasiparticle bandgap.

Secondly, the hBN/WS_2/hBN sample has a much narrower linewidth with a full width half maximum (FWHM) of 5 meV compared to the WS_2/SiO_2/Si sample (FWHM = 22 meV). The atomically flat hBN layer can smooth the potential variation at the interface, which greatly reduces the inhomogeneous broadening. The encapsulated sample shows much higher optical quality that enables us to resolve more detailed excitonic structures in the PL spectrum.

Thirdly, the spectral weight of the neutral exciton X_A emission for the hBN/WS_2/hBN

sample dominates the whole spectrum while it shows a weak emission for the WS_2 on SiO_2/Si substrate compared to the lower-energy charged exciton complexes. While almost all of the exfoliated WS_2 monolayer by previous studies are intrinsic n-type semiconductors, our result suggests that the doping level in the hBN/WS_2/hBN sample can be greatly reduced. Therefore, it gives rise to the PL spectrum that approaches the one of intrinsically charge-free WS_2 monolayers. One of the reasons is that the hBN layer can act like a charge absorber to the electrons generated from localized states (or dopants) at the interface upon light excitation, and thus reducing the doping level. On the other hand, it is reported that, at a small exciton density, the hBN/WS_2/hBN sample exhibits an exciton-exciton annihilation (EEA) rate $(6.3\pm 1.7) \times 10^{-3}$ cm^2s^{-1}, being 2 orders of magnitude smaller than that of hBN/WS_2/SiO_2 sample due to the nonradiative exciton-exciton-annihilation-mediated recombination (see Figure 5.3) [15]. It gives us hints that different dielectric environments could change the relaxation and decay pathways of the exciton species, leading to dissimilar PL spectra, as we observed in Figure 5.1.

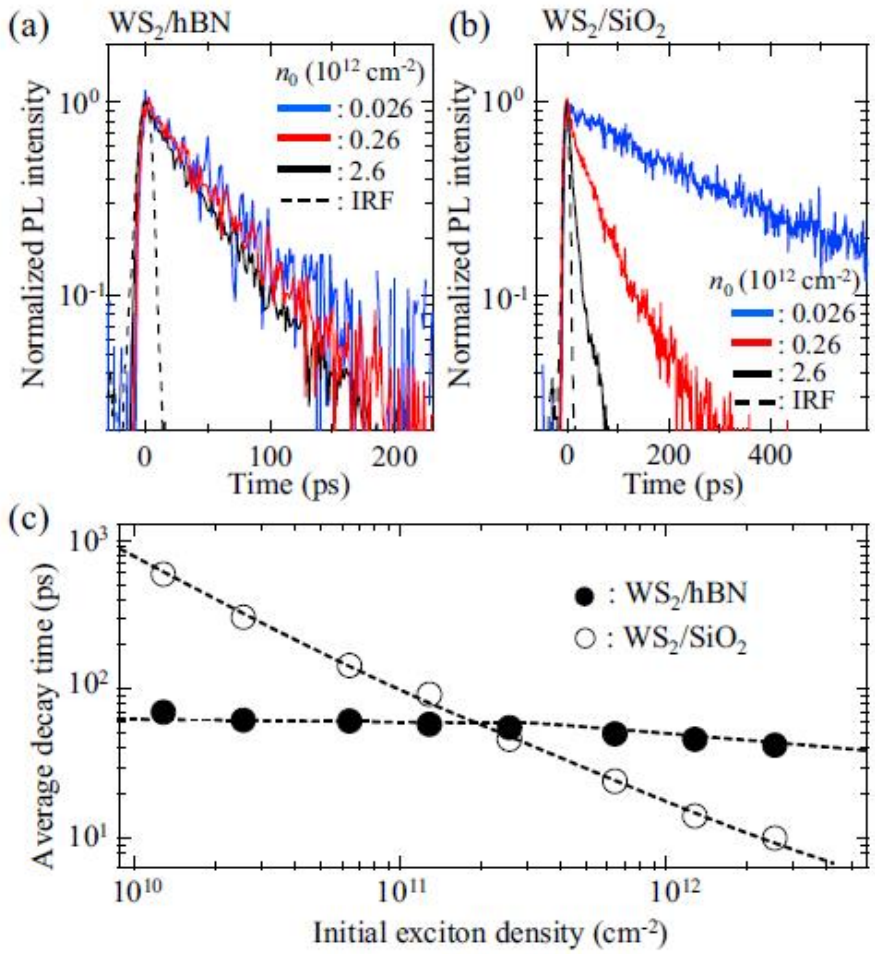

Figure 5.3: Time resolved exciton PL decay curves for (a) hBN/WS_2/hBN and (b) hBN/WS_2/SiO_2 at different exciton densities. The dashed curves show the instrumental response function (IRF). (c) Average decay times as a function of photo-excited exciton densities for hBN/WS_2/hBN (filled circles) and hBN/WS_2/SiO_2 (open circles). [15]

5.2 Spectral Analysis and Power Dependent Photoluminescence Spectra

Overall, by fabricating the hBN-encapsulated heterostructure, we have successfully reduced the inhomogeneous broadening of the linewidth and the doping level of WS_2 monolayer. Next, we performed further optical characterization on this sample to investigate the lower-energy excitonic complexes.

To resolve the different components in the complicated PL spectrum, it is fitted with multiple Gaussian functions, as shown in Figure 5.4(a). With the best fitting results, nine components are resolved in total, which corresponds to different excitonic features. Their peak positions are extracted in Table 5.1. The peak with the highest energy at

$\sim$2.063 eV is identified as the neutral exciton state X_A from the K/K transition in the Brillouin zone, whose energy matches its absorption resonance in Figure 5.1. The peaks at $\sim$2.033 eV and 2.027 eV are identified as the intervalley trion state (the so-called triplet state T^-) and intravalley trion state (singlet state S^-) states with the trion binding energies of $\sim$ 30 meV and 36 meV, respectively, as reported in previous studies for W-based monolayers [90, 93–97, 100–103]. The energy splitting between the triplet and singlet state Δ_{S-T} is $\sim$6 meV, arising from the exchange interaction δ between the excess electron and the electron-hole pair that have the spin configuration (see the inset in Figure 5.4(a)).

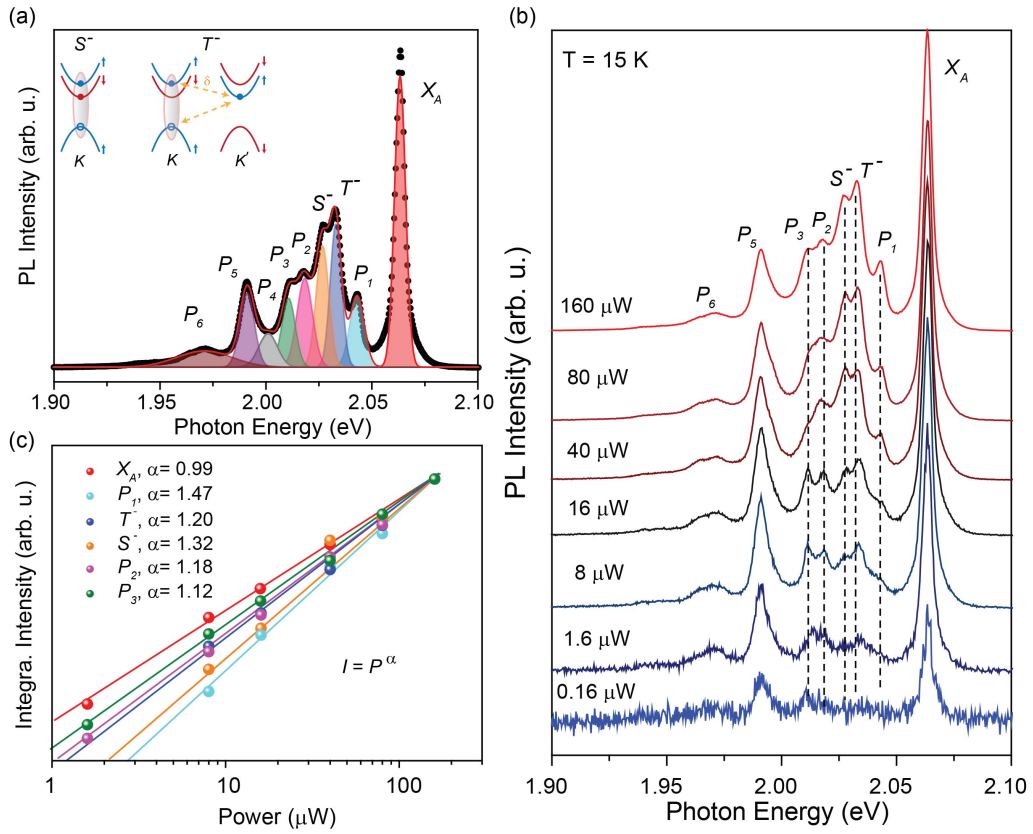

Figure 5.4: Power-dependent photoluminescence spectra. (a) Multi-peak fittings of the PL spectrum with Gaussian functions, in which nine peaks are resolved with different colors. The inset shows the valley configuration of the singlet and triplet trion states, in which the blue and red color denote the spin-up and spin-down band edges, respectively. The yellow arrows represent the exchange interaction δ between the electrons and the hole with the same spin. (b) Power-dependent photoluminescence spectra taken with a 532 nm laser. (c) Power law of the different components.

Table 5.1: Energy positions of different components

Peaks	X_A	P_1	T^-	S^-	P_2	P_3	P_4	P_5	P_6
Peak energy (eV)	2.063	2.043	2.033	2.027	2.018	2.011	2.001	1.991	1.971

To further confirm the origins of other components, power-dependent PL spectra are taken with the 532 nm excitation, as shown in Figure 5.4(b). The spectra are fitted by the same amount of peaks as Figure 5.4(a) shows. Figure 5.4(c) gives the power law plot of the integrated intensities for several peaks. For neutral exciton X_A, the intensity shows a linear dependence with the excitation power. The triplet T^- and singlet state S^- exhibit a power law of 1.20 and 1.32, respectively. Interestingly, the peaks P_1, P_2, P_3 also have a superlinear dependence with the power of 1.47, 1.18 and 1.12, while the P_4, P_5 and P_6 have a sublinear dependence. P_1 with a strong superlinear power-dependent behaviour has been observed by previous studies that is attributed to the biexciton emission with a binding energy of $\sim$ 20 meV [93–96, 104]. P_4 can be attributed to the localized state due to its saturation at high power excitation. The energy differences of $\Delta(P_2P_5)$ and $\Delta(P_5P_6)$ are equally 20 meV, which could be attributed to the phonon replicas as described in Chapter 4. While P_5 and P_6 both disappear at higher doping density, we shall focus on the behaviours of P_2 and P_3 in this work.

5.3 Gate Tunable Reflectance Spectra

In order to identify the nature of being charged states for the unknown peaks, we fabricated a back-gate heterostructure FET device to tune the charge density in WS_2 monolayer, as shown in Figure 5.5(a). Figure 5.5(b) gives the gate sweep curves across -60 V to 60 V. It shows a n-type conducting regime when it exceeds a threshold V_{th} around 40 V. To estimate the maximum of the gate voltage induced carrier density n_{2D}, a parallel-plate capacitor model $n_{2D} = C(V_g - V_{th})$ is used where C is the back-gate capacitance of $C = 1.2 \times 10^{-8}$ F cm^{-2} [25]. The maximum of the carrier density at 60 V is estimated as $n_{max} = 1.5 \times 10^{12}$ cm^{-2}.

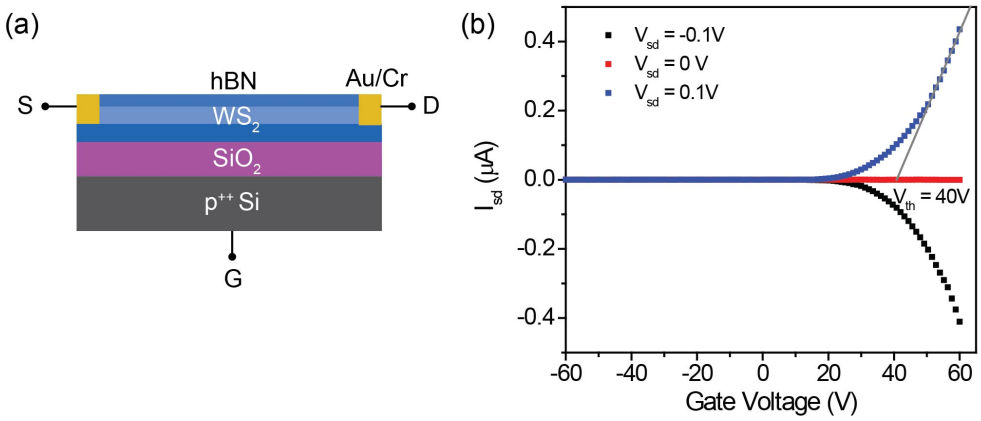

Figure 5.5: Gate sweep of the hBN/WS_2/hBN FET device. (a) The schematic illustration of the hBN/WS_2/hBN heterostructure FET device. (b) The source-drain current plot as a function of gate voltage. The threshold voltage V_{th} for the conducting regime is estimated to be 40 V.

Next we investigate the gate dependent reflectance spectra. Figure 5.6(a) shows the reflectance spectra mapping of our WS_2 heterostructure device with a white light excitation. The selected spectra at several voltages are presented in Figure 5.6(b). For V_g below $\sim$10 V, a dominant feature identified as neutral exciton X_A is clearly resolved. When the V_g exceeds $\sim$10 V, the feature X_A shows a clear blueshift and a vanishing amplitude until it disappears at $\sim$40 V. Such phenomenon could be explained through three mechanisms: elastic Coulomb scattering, Pauli blocking and screening of the Coulomb interaction [105]. The elastic scattering of excitons with free charge carriers reduces the exciton coherence lifetimes, thus leading to a broadened spectrum of the exciton transition. Pauli blocking and the screening of the electric fields by the free charges will induce a decrease of the exciton oscillator strength and binding energy [105]. Moreover, it is also pointed out that the screening of the repulsive interaction within electrons induces a decrease of the quasiparticle self-energy, which gives rise to the renormalization of the band gap to a lower energy [105]. The exciton transition, therefore, blue-shifts as the result of the joint effect of band gap renormalization and reduced binding energy [105].

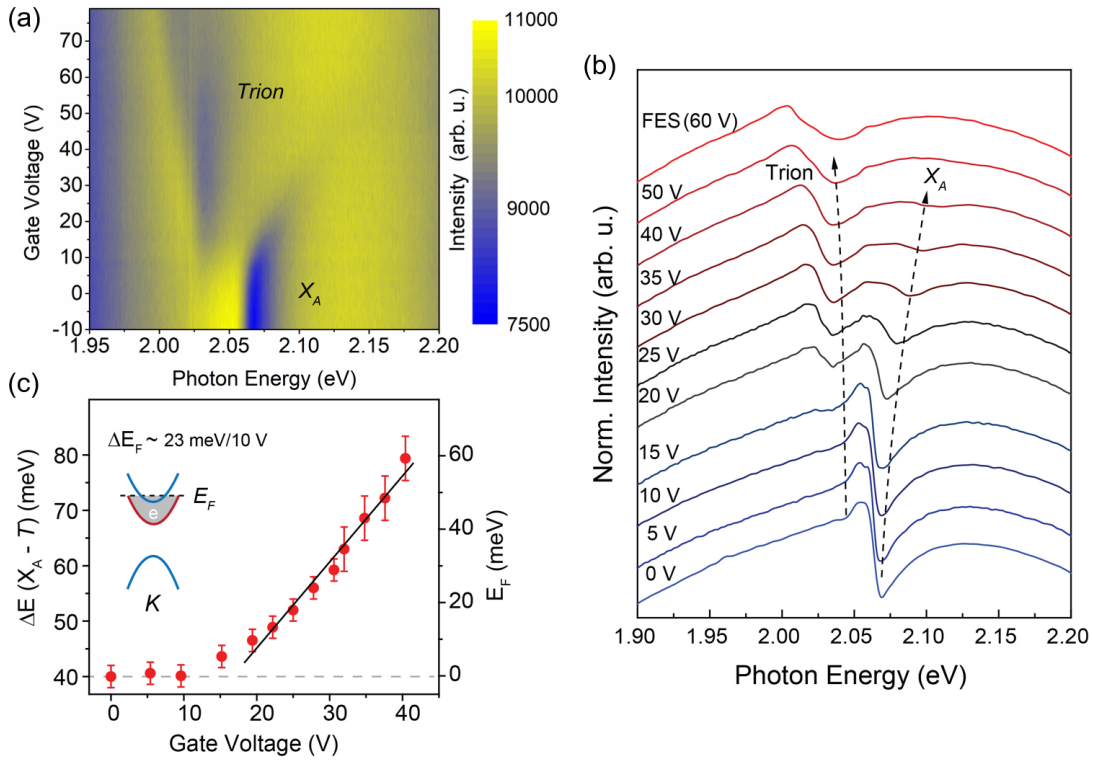

Figure 5.6: Gate-dependent reflectance spectra. (a) The reflectance spectra mapping of the WS_2 heterostructure device as a function of gate voltage V_g at 15 K. The color represents the reflectance intensity. (b) The selected reflectance spectra under specific gate voltages. The dashed lines show the evolution of the absorption features (X_A and Trion) from a relatively neutral state to the broad, asymmetric Fermi edge singularity (FES) due to the increasing electron doping. (c) The gate voltage induced Fermi energy change E_F relative to the conduction band bottom (defined as $E_F = 0$), which is estimated from the energy splitting between neutral exciton X_A and trion in the reflectance spectra. The dashed line denotes the zero-density trion binding energy. The inset shows the schematic illustration of the gate-induced electron doping effect in WS_2 monolayer, where the blue curves denote the spin-up bands and the red one denotes the spin-down band at K valley.

In the meantime, a lower-energy feature becomes observable and starts to dominate the spectra with $V_g \geq 10$ V, which is attributed to the creation of negatively charged excitons (trions) in the 2D system. When it reaches a higher density of two-dimensional electron gas ($n = 1.5 \times 10^{12}$ cm^{-2} at $V_g = 60$ V, estimated from the gate sweep), the trion feature is replaced by a broad, highly asymmetric dip called Fermi edge singularity, which is typically observed in quantum well structures that contains a two-dimensional electron gas [105–108]. Such phenomenon arises from intense scattering processes involving electrons near the Fermi level, which strongly alters the spectral shape [108].

The energy separation between the exciton X_A and trion feature defines the trion

binding energy $\Delta E(X_A - T)$, which represents the energy it takes to remove one of its two electrons. It almost increases linearly with the gate voltage when V_g is above 10 V(see Figure 5.6(c)), as was observed in previous reports [37, 105, 109]. Due to the electron doping in the 2D system, the Fermi energy, that can be considered as the kinetic energy of Fermi electrons, increases, leading to an increase of $\Delta E(X_A - T)$ as well. The relationship between $\Delta E(X_A - T)$ and the Fermi energy is given by $\Delta E(X_A - T) = E_{b0} + \alpha E_F$, where E_{b0} is the trion binding energy at zero density for free electrons, E_F is the Fermi energy relative to the bottom of the conduction band (defined as E_F = 0). A simple model can be used to estimate the gate-induced Fermi energy [105].

After photon absorption, excitons (X_A) are resonantly created in the system, which simultaneously binds a free electron in the system to form a trion. Later the trion will radiatively decay, emitting a photon E^T_{photon} and leaving a free electron with energy E^{kin}_e in the system. Energy conservation for the two processes requires:

$$E^T_{photon} + E^{kin}_e = E_{X_A} - E_{b0} + E^{kin}_T \tag{5.3}$$

where E^{kin}_T is the kinetic energy of trion. On the other hand, momentum conservation requires:

$$Q^T_{photon} + Q_e = Q_{X_A} + Q_e = Q_T \tag{5.4}$$

The momenta of emitted photon Q^T_{photon} and resonantly excited exciton Q_{X_A} are almost zero, which gives $Q_e = Q_T$. Due to the almost equal effective masses of the electrons and holes at band edges in TMDs monolayers, $Q_e = Q_T$ leads to the relationship of kinetic energies between the emitted photon and free electron by $E^{kin}_T \approx 1/3E^{kin}_e$. Therefore, the energy separation between exciton and trion $\Delta E(X_A - T)$ is given by

$$\Delta E(X_A - T) = E_{X_A} - E^T_{photon} = E_{b0} + \frac{2}{3}E^{kin}_e, \tag{5.5}$$

where the kinetic energy E^{kin}_e could be considered as the Fermi energy of the free electrons, which is relative to the conduction band minimum. According to this model, the binding energy of trions at zero free electron density is obtained as 40 meV and the estimated change of Fermi energy is plotted as a function of gate voltage in Figure 5.6(c). The increase of V_g by 10 V gives rise to an increase of Fermi energy by $\sim$23 meV at $V_g \geq 20$V.

5.4 Gate Tunable Photoluminescence Spectra

In the following we further investigate the evolution of excitonic features in PL spectra from the low doping regime to the Fermi edge singularity. Figure 5.7(a) shows the PL mapping at 15 K as a function of gate voltage with a 532 nm laser excitation. The PL spectra at several gate voltages are sorted out in Figure 5.7(b) for a comparison. The integrated intensities of individual features are extracted from multi-peak fittings of multiple spectra and plotted as a function of gate voltage in Figure 5.7(c).

In the mapping plot, several main features are clearly resolved. First of all, the neutral exciton X_A emission gradually vanishes until V_g exceeds 40 V, similar to what is observed in the reflectance measurement (see Figure 5.6(a)). This observation indicated a reduced oscillator strength of the exciton transition due to the Pauli blocking and screening of the Coulomb interaction. Secondly, the peak XX identified as biexciton emission vanishes quickly at $V_g = 10$ V because its binding energy ($\sim$20 meV) is too small to overcome the free charge screening. Thirdly, the emission from triplet T^- and singlet S^- trion states shows a non-monotonic evolution. Specifically, the emission intensity of T^- increases for $V_g \leq 30$ V and decreases for $V_g \geq 30$ V, which reaches the highest intensity at $\sim$30 V. While the singlet state S^- experiences the same change, it reaches maximum at $\sim$30 V with 5 V delay, as shown in Figure 5.7(c). It is ascribed to the combined result of increased trion population with higher electron doping and reduced oscillator strength due to the Coulomb screening effect.

More interestingly, the intensities of P_2 and P_3 increase rapidly until they dominate at higher doping regime. Previous studies have revealed the many-particle complexes within the same energy range (~ 50 meV below X_A) under a low doping regime. For example, several works have reported a five-particle structure called exciton-trion complexes in the W-based monolayer while they disappear rapidly with increasing electron doping [93–96, 104]. In addition, dark excitons or dark trions due to the spin-forbidden exciton are reported to exist within the same energy range, but still in the low doping regime [90, 92–97, 103, 104]. The only feature that extends to a higher doping regime is simply attributed to the double-negatively charged trion (X^{--}) [95, 96]. However, we do not believe such structure could still exist even after the trion states (T^- and S^-) with larger binding energy have dissociated in the high doping regime. Our PL mapping result is very different from previous reports that it clearly shows P_2 and P_3 increase continuously with electrons injection, and finally become the Fermi edge singularity, which confirms

their nature of being charged states. Moreover, they behave as trion fine structures split by an energy of 7 meV, similar to the triplet T^- and singlet S^- trion states but from different excitonic species. In our previous Chapter, we indicate that the lower-energy momentum-indirect excitons could contribute to the lower-energy emission structure in WS_2 monolayer. In addition, recent studies have both theoretically and experimentally revealed the existence of momentum-indirect excitons at Λ valley [110–112]. Therefore, we attribute the formation of P_2 and P_3 to the charged momentum-indirect Λ valley excitons. In the following, we shall discuss in detail the possible mechanism of how the electron Fermi sea facilitates the formation of different charged valley excitons.

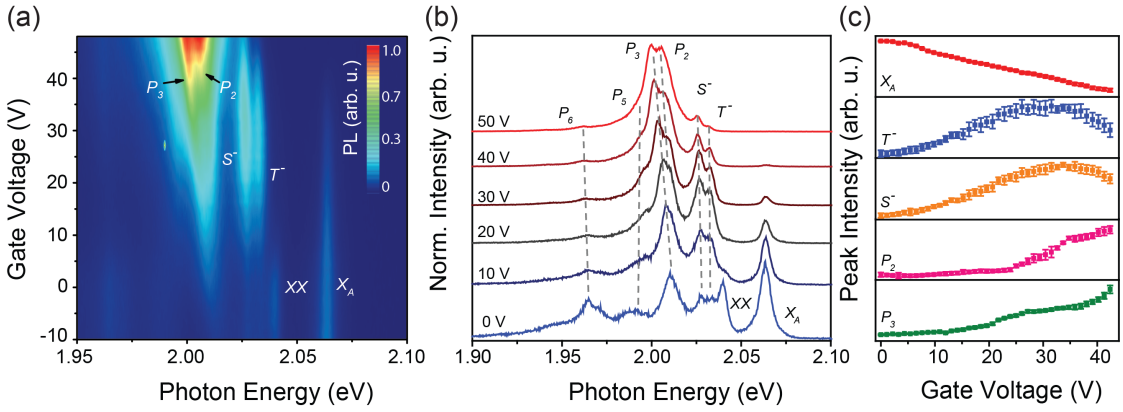

Figure 5.7: Gate-dependent PL spectra. (a) PL spectra at 15 K as a function of gate voltage, with a 532 nm laser excitation. The color represents the PL intensity. The excitonic features are labeled according to the fitting results in Figure 5.4(a), among which the P_1 is identified as the biexciton emission. (b) Selected PL spectra at several gate voltages. The dashed lines show the evolution of individual peaks. (c) The integrated intensities of individual peaks as a function of gate voltage, extracted from the fitting results. The vertical dashed lines mark out the voltages that correspond to the highest intensity of T^- and S^- at ∼30 V and ∼35 V, respectively.

5.5 Formation of Charged Indirect-Valley Excitons Assisted by Fermi Electrons

In the Chapter 4, we have demonstrated the possible formation and relaxation pathways of momentum-direct excitons at Γ-valley and momentum-indirect excitons at Λ-valley, where the lowest-energy band is momentum-indirect Λ-band [111]. As a result, most of the excitons should occupy the Λ-band. Moreover, we suggest that the Λ-valley excitons could contribute to the emission of P_2 and P_3 in the PL spectrum of WS_2 monolayer. However, due to its momentum-indirect nature, the oscillator strength of Λ-valley

excitons is very small that limits their optical yield under a low-doping regime, which is confirmed by the PL spectra in Figure 5.4(a). While the Fermi level of WS_2 monolayer at elevated electron densities is lifted into the conduction band, the two-dimensional electron gas, that could act as quasiparticles with a well-defined energy and wavevector, will interact with excitons through Coulomb interactions [113, 114].

The previous work by Tuan *et al.* [114] explains the similar structure (in the energy range of P_2 and P_3 in our case) to the exciton-plasmon quasiparticle due to intervalley (K-$K^{'}$) Coulomb excitations. However, it does not fully apply to the state-of-art studies including our and other results. For example, the exciton-plasmon quasiparticle picture could not explain the fine structure of P_2 and P_3 features. Secondly, the indirect excitons that they associate to form the exciton-plasmon quasiparticle come from the opposite K valleys [113, 114], while recent experimental work in [112] directly visualized the momentum-forbidden Λ-valley excitons in WSe_2 monolayer that dominates the exciton population via a time, momentum and energy-resolved ARPES technique. Based on the mentioned facts, we associate P_1 and P_2 to the charged Λ-valley trions and propose the mechanism of charge-assisted recombination process.

Figure 5.8 shows the formation of charged momentum-direct K-K and momentum-indirect Λ-K excitons at elevated electron densities. The formation of charged exciton states benefits from the Fermi electron gas in the conduction band that interact with both direct- and indirect-excitons through Coulomb interactions.

The Coulomb potential of the Fermi electron gas could work as two parts through electrons cross the Fermi edge, that is, the long-range part and the short-range part [114, 115]. The energy dispersion of the long-range part is given by

$$E_l(k) = \sqrt{\frac{2e^2 E_F k}{\epsilon(k)}}, \tag{5.6}$$

where e is the unit charge, k the wavevector of the collective Fermi excitation, the Fermi energy $E_F = \pi\hbar^2 n/2m_e e^2$ and the static dielectric coefficient $\epsilon(k)$ [114].

The long-range Coulomb potential is almost independent of the electronic band structure due to its much longer wavelength than the lattice constant, which only leads to intravalley processes (with small momentum change). As a result, it leads to the screening of the electron-hole attraction, the reduced exciton oscillator strength and the renormalization of the band gap. Moreover, the intravalley Coulomb interaction could prevent the formation of trion states due to the screening effects. When the system is

under a weak long-range interaction, the excitons can bind with Fermi electrons to form trions. As shown in Figure 5.8(b), the singlet state is formed with one of the Fermi electrons binding to a direct exciton. While for the triplet state (see Figure 5.8(c)), the intervalley electron-hole exchange interaction (denoted by σ) between the direct excitons at K valley and the Fermi electron in $K^{'}$ valley with the same spin reduces its binding energy by 7 meV, compared with the singlet state [100–102]. The enhancement for the singlet and triplet intensity happens when E_F is below $\sim$34 meV (for $V_g \leq 35$ V in Figure 5.7), which is comparable to the spin-split conduction band with $\Delta_{CB} \sim 30$ meV [16, 17]. At the even higher Fermi energy, the binding energy of charged direct exciton states could no longer hold the binding of the Fermi electrons, thus leading to their dissociation.

On the other hand, the short range Coulomb potential work through electrons between valleys [113, 114], which is treated as shortwave plasmons with the energy dispersion of :

$$E_s(q) = \Delta_{CB} + (1 + \frac{3}{\alpha}\tilde{\epsilon}_q + \frac{\alpha}{3}E_F) \tag{5.7}$$

where $\alpha = (K_0 a_s)^{-1} \sim 0.1$, and $\tilde{\epsilon}_q = \hbar^2(K_0 - q)^2/2m_e$. The $K_0 = 4\pi/3a$ here denotes the wave number that connects $K/K^{'}$ valleys (a $\sim$ 3.3 Å is the lattice constant) and $a_s = \hbar^2\epsilon_{ML}/e^2m_e$ is the effective Bohr radius. However, the situation for the $K/K^{'}$ indirect excitons needs to be adjusted in our case. Figure 5.8(d) shows the configuration of a Λ-valley exciton, that consists of a Λ-valley electron and a K-valley hole. Similarly, two charged states of the Λ-valley excitons could be formed with the assistance of the electrons dressed by the Fermi sea. Figure 5.8(e) gives the configuration for P_3, that is the Λ-valley exciton bind with the Fermi electron in K valley with the opposite spin (called Λ-singlet), as shown in Figure 5.8(b). In the photon emission process, the Fermi electron provides the momentum mismatch required by $\Delta q = q_e^{\Lambda} - q_h^{K} = \Lambda = 2\pi/3a$. Therefore, the α and $\tilde{\epsilon}_q$ in Equation 5.7 need to be adjusted as $\alpha = (\Lambda a_s)^{-1} \sim 0.05$ and $\tilde{\epsilon}_q = \hbar^2(\Lambda - q)^2/2m_e$, accordingly. Moreover, as shown in Figure 5.8(f), the Fermi electron with the same spin as the indirect Λ-valley excitons (called Λ-triplet) could experience the exchange interaction δ among themselves, which introduces an energy lift compared with the configuration in Figure 5.8(e). The induced energy splitting between Λ-singlet and Λ-triplet state is $\sim$7 meV, which is comparable to $\sim$6 meV between S^- and T^- for charged direct excitons (see Table 5.1). It is noted that, as stated in [114], the intervalley Coulomb potential does not come from individual electrons in the Fermi

sea, since the Fermi wavevector k_F that can characterize the individual Fermi electrons is more than 1 order of magnitude smaller than K_0 even at $n_e \sim 10^{13}$ cm^{-2}. Instead, it arises from the collective excitation of the Fermi gas (called plasmon), which is an independent degree of freedom in the electronic system.

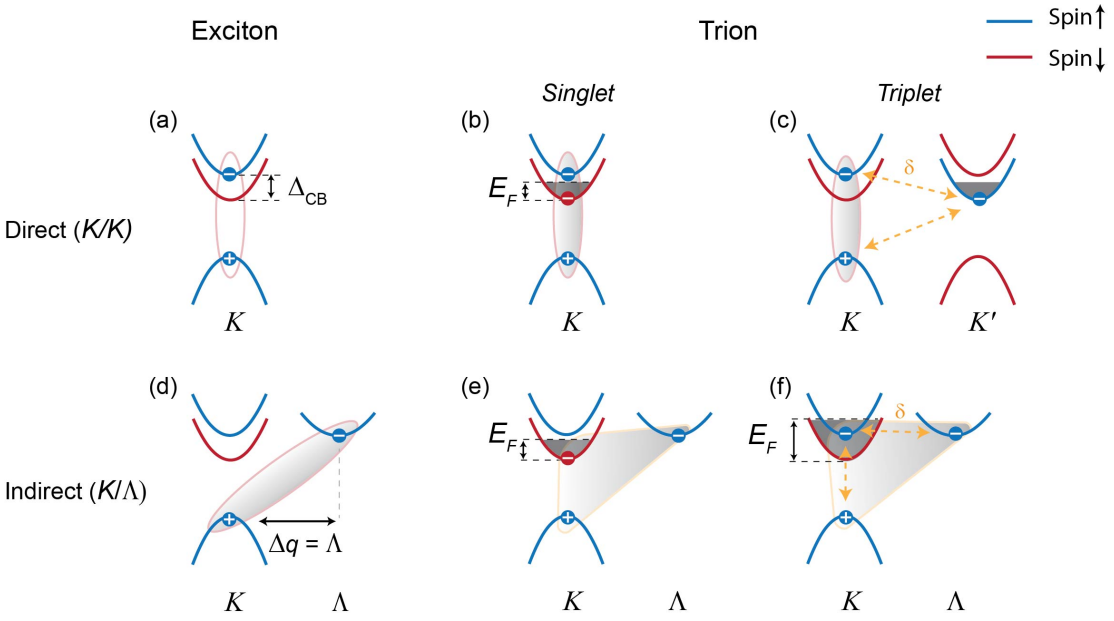

Figure 5.8: The formation of charged momentum-direct K-K (Γ-) excitons and momentum-indirect K-Λ (Λ-valley) excitons at elevated intensities. (a) The direct K/K exciton. The first K denotes the valley that the hole resides in, while the latter one denotes the valley that the electron resides in. The conduction band splitting Δ_{CB} ~30 meV [16, 17]. (b) The singlet state of the charged direct exciton that interacts with a Fermi electron in the spin-unlike conduction band at K valley. (c) The triplet state of the charged direct exciton that interacts with a Fermi electron in the spin-like conduction band at $K^{'}$ valley. (d) The indirect Λ/K exciton, consisting of a Λ-valley electron and a K-valley hole. The momentum mismatch between the electron and hole is $\Delta q = q_e - q_h = \Lambda = K/2$. (e) The singlet state of the charged direct exciton that interacts with a Fermi electron in the spin-unlike conduction band at K valley. (f) The triplet state of the charged indirect exciton that interacts with a Fermi electron in the spin-like conduction band at K valley.

5.6 Coulomb Screening Effect of A Two-dimensional Electron Gas

At higher gate voltage ($V_g = 60V$), a single peak feature replaces all the charged states as shown in Figure 5.9.

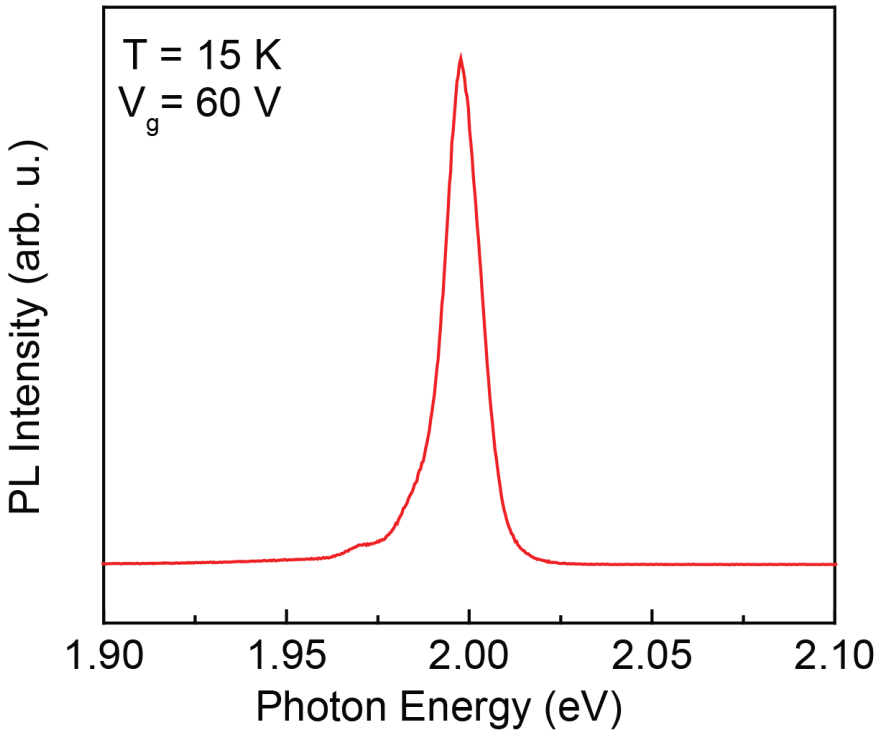

Figure 5.9: PL spectrum of WS_2 at 60 V, showing a single emission feature at high electron doping.

To demonstrate the evolution of the PL spectra with the change of doping density, we shall discuss the Coulomb screening effect of a 2D electron gas. In a parabolic band dispersion, the 2D statically screened Coulomb potential is given by $V_s(q, \omega = 0) = \frac{2\pi e^2}{\epsilon}\frac{1}{q+q_s}$, where q is the screening wavevector. q_s is the Tomas-screening wave number, given by $q_s = \frac{2g_v}{a_B}$ where g_v denotes the valley degeneracy and $a_B = \frac{\epsilon\hbar^2}{me^2}$ the electron Bohr radius.

Here we discuss two doping regimes where the excitons could interact with the Fermi sea differently. The difference reflects on the screening effect of the 2D Fermi sea on the excitons, which strongly depends on the density of the 2D electron gas. The Coulomb screening effect could be divided into intravalley (with small screening wavevector q 0) and intervalley parts (with $q \neq 0$) as shown in Figure 5.10. The screening potential V_s scales with the inversed screening wavevector $\frac{1}{q}$ at large q value.

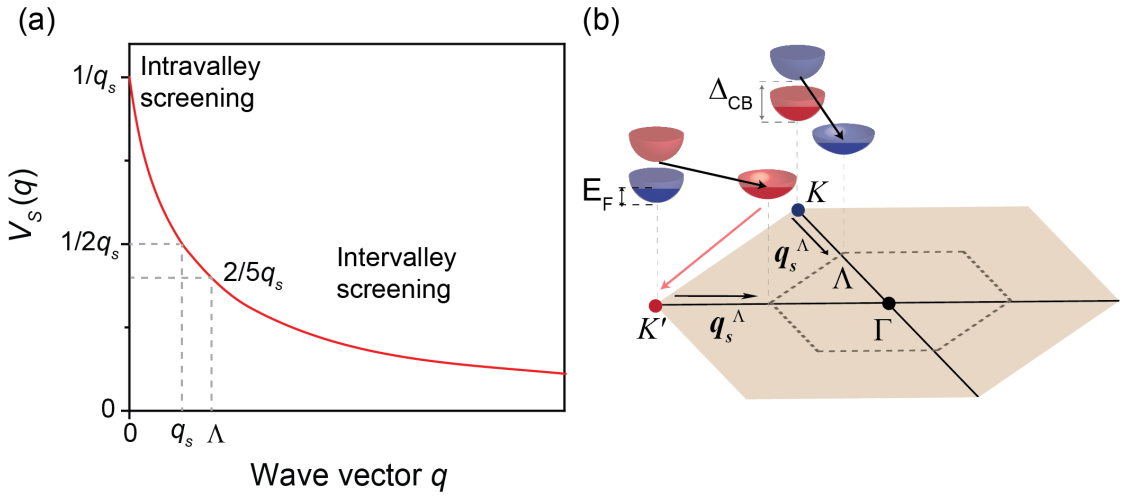

Figure 5.10: Coulomb screening effect of a two-dimensional electron gas (a) Intravalley and intervalley Coulomb screening potential at elevated electron intensities. (b) Intervalley scattering of electrons between K and Λ valleys. The conduction band edges at K and Λ are plotted in the hexagonal Brillouin zone while the valence band is omitted. The black arrow denotes the intervalley screening wavevector, while the red arrow denotes the intervalley radiative recombination process.

In the low-doping regime, the Fermi-polaron (or trion) picture is valid. The intravalley screening effect is weak and the intervalley screening is negligible. In this case, the attractive Coulomb interaction between the excitons and Fermi electrons could still exist, so as to form the bound exciton-Fermi electron complex for both direct and indirect-excitons, as a result of which we can observe the multiple charged states in Figure 5.7(a).

In the high-doping regime, the intravalley screening effect becomes stronger and the intervalley screening is not negligible (see Figure 5.10(a)). The strong intravalley screening potential will screen the attractive Coulomb interaction between the excitons and Fermi electrons, breaking the binding of the exciton-Fermi electron complex (charged states). At the same time, the emission from the excitons with small momentums are quenched due to reduced oscillator strength and binding energy. The enhanced intervalley screening potential facilitates the scattering of electrons between different valleys, which drives the electrons at Λ-valley to move to K-valley and radiatively recombine with the K-valley holes as shown in Figure 5.10(b). Due to the screened intravalley transition, this intervalley transition gives the only visible emission feature in the PL spectrum at high doping regime (see Figure 5.9). In this case, instead of discussing interaction between excitons and Fermi sea, we shall just discuss the interactions among the electrons. The collective excitation of the electrons could form plasmons at high doping regime. The

dressing of the photo-excited electrons by the Fermi sea could be then described by the plasmon picture. It needs to be pointed out that there are different terms used to describe the interaction between excitons and Fermi sea, which basically discusses the same physical phenomena.

5.7 Power Law of the Charged Indirect-Valley Excitons and Exciton-Plasmon Quasi-particles

Up to now, I have demonstrated the formation and emission process of charged indirect-valley excitons. The photoexcited electron-hole pairs could interact with Fermi electrons, either individually or collectively, depending on the strength of long-range Coulomb potential. For a weak long-range Coulomb potential regime (much below the Fermi edge singularity), the indirect excitons tend to bind with individual electrons to form charged states, during which various power laws of their emission observed in W-based monolayers could be predicted by a simple model. For simplicity, we only consider the direct bright excitons, momentum-indirect Λ-excitons and their charged states, ignoring the spin-forbidden dark excitons and their possible charge states. Their existence does not change the conclusion here.

We first define the notations as follows: the density of photoexcited electron-hole pairs n is proportional to the excitation power by $n = n_e = n_h = \beta P_{exc}$ where β denotes the absorption coefficient; The Fermi electrons density n_F; The direct exciton population n_{X_Γ} and indirect exciton population n_{X_Λ}; The corresponding charged states $n_{X_\Gamma^-}$ and $n_{X_\Lambda^-}$ (we do not distinguish between the triplet and singlet state). Due to the total hole density conservation, they must satisfy:

$$n_{X_\Gamma} + n_{X_\Lambda} + n_{X_\Gamma^-} + n_{X_\Lambda^-} = n_h = n \tag{5.8}$$

The population of excitons and their charged states are governed by the Saha equation [25]:

$$\frac{n_{X_\Gamma} n_F}{n_{X_\Gamma^-}} = A_1 k_B T exp(-\frac{E_{T1}}{k_B T}) = n_{A1} \tag{5.9}$$

$$\frac{n_{X_\Lambda} n_F}{n_{X_\Lambda^-}} = A_2 k_B T exp(-\frac{E_{T2}}{k_B T}) = n_{A2} \tag{5.10}$$

where k_B is the Boltzmann constant; $A_1, A_2 = \frac{4M_{X_\Gamma,X_\Lambda}m_e}{\pi\hbar^2 M_{X_\Gamma^-,X_\Lambda^-}} \approx 6.18 \times 10^{11}\frac{1}{cm^2 meV}$; E_{T1} and E_{T2} are the trion binding energy for X_Γ^- and X_Λ^-, respectively.

The exciton population of n_{X_Γ} and n_{X_Λ} under the thermal equilibrium should obey the Boltzmann distribution:

$$n_{X_\Gamma}/n_{X_\Lambda} = exp(-\frac{\Delta_{\Gamma\Lambda}}{k_B T}) \tag{5.11}$$

where $\Delta_{\Gamma\Lambda}$ meV is the energy splitting between the bright exciton X_Γ and momentum-indirect X_Λ excitons. Thus, the population of the X_Λ^- is:

$$n_{X_\Lambda^-} = \left(\frac{n_{A2}(1+exp(-\frac{\Delta_{\Gamma\Lambda}}{k_B T}))}{n_F} + \frac{n_{A2}exp(-\frac{\Delta_{\Gamma\Lambda}}{k_B T})}{n_{A1}} + 1\right)^{-1} . n \tag{5.12}$$

Due to the involving of the Fermi electrons in the formation and recombination process of trions, the emission intensity of X_Λ^- should also consider the change of Fermi electrons with the power excitation. It is noted in our power dependent PL spectra that the trion binding energy (take the triplet T^- for example) increases with the increase of excitation power, as shown in Figure 5.11.

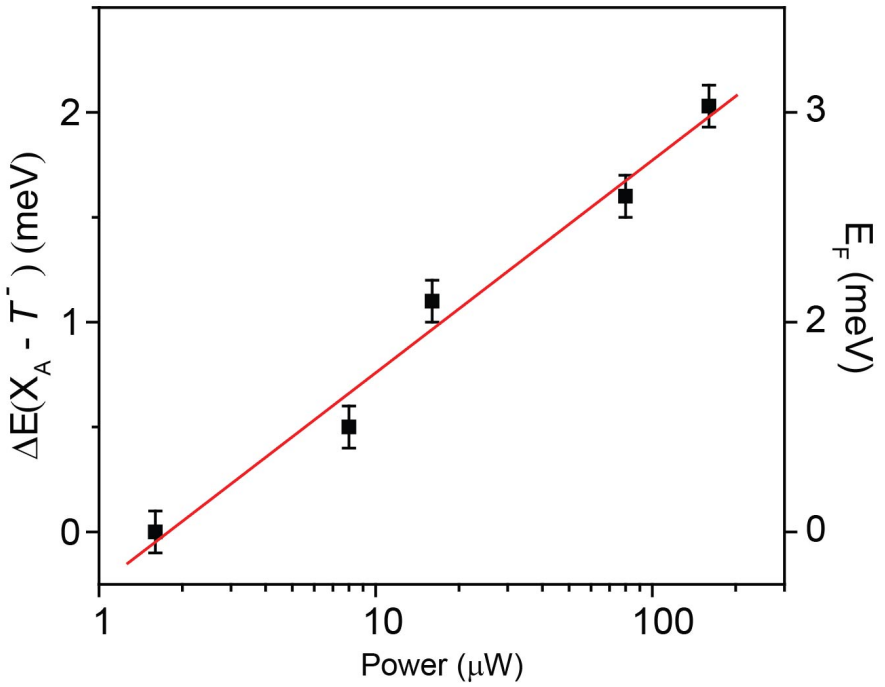

Figure 5.11: Excitation power induced Fermi energy change deduced from the energy splitting between X_A and T^-. When the excitation power increases ten times, the triplet binding energy increases ~1 meV, which corresponds to an increase of the quasi-Fermi energy by ~1.5 meV .

We find that when the excitation power increases ten times, the triplet binding energy increases ∼1 meV, which corresponds to an increase of the quasi-Fermi energy by ∼1.5 meV ($E_F = 1.5 log_{10} P_{exc}$) according to Equation 5.5. Thus, we can expect a relationship between the photo-induced doping density and excitation power by

$$n_F = \gamma log_{10} P_{exc}, \tag{5.13}$$

where γ is the coefficient of photoinduced electron doping density as the excitation power increases that is set as a free parameter. In addition, we assume the initial doping in our sample is nearly zero due to the very weak trion emission with low power excitation in the PL spectra. Such photoinduced doping could arise from the excitation of defect states at hBN/WS_2 that acts as donors to inject electrons into the WS_2 conduction band.

Therefore, the emission intensity of X_Λ^- could be estimated from Equation 5.12 and 5.13 as:

$$I_{X_\Lambda^-} \propto n_{X_\Lambda^-} \propto \left(\frac{n_{A2}(1 + exp(-\frac{\Delta_{\Gamma\Lambda}}{k_B T}))}{\gamma log_{10} P_{exc}} + \frac{n_{A2} exp(-\frac{\Delta_{\Gamma\Lambda}}{k_B T})}{n_{A1}} + 1 \right)^{-1} . P_{exc} \tag{5.14}$$

To model the power dependence behaviour, the binding energy of X_Γ^- and X_Λ^- are assumed to be equal by 30 meV, from which we can estimate the $\Delta_{\Gamma\Lambda}$ to be 15 meV according to energy difference between T^- and P_2. The modelling results are shown in Figure 5.12

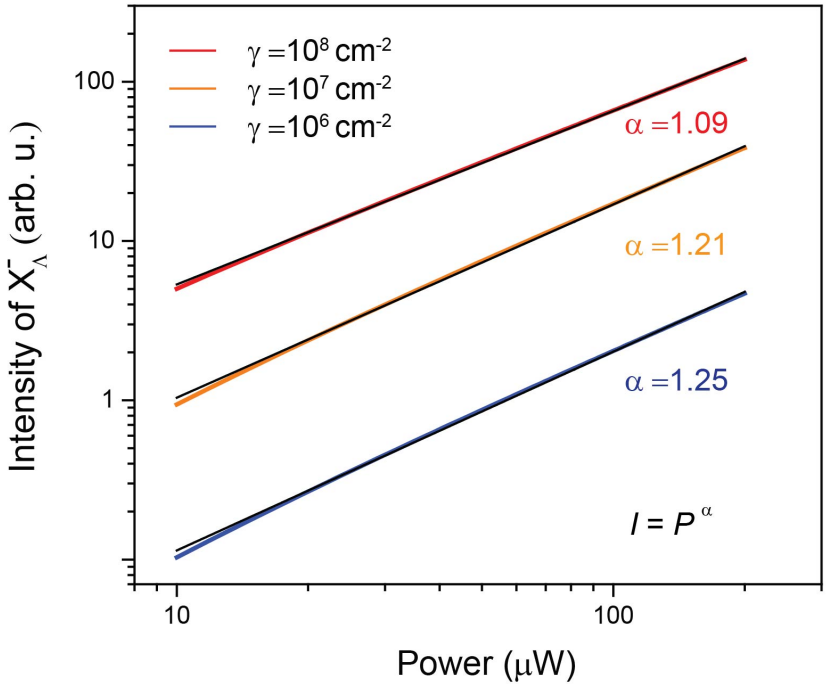

Figure 5.12: Modelling X_Λ^- intensity as a function of excitation power for different γ. The power law of α is found to vary from 1.09 to 1.25 as γ changes from 10^8 cm^{-1} to 10^6 cm^{-1}, indicating the important role of photoinduced doping in power dependent behaviour.

From the model, the power law of α is found to vary from 1.09 to 1.25 as γ changes from 10^8 cm^{-1} to 10^6 cm^{-1} which indicates the important role of photoinduced doping in power dependent behaviour. Such superlinear behaviour has been observed in our result and also commonly reported in many studies [38, 74].

While near the Fermi edge singularity, the emission has a linear power dependence with $\alpha = 1.04$ as shown in Figure 5.13. It exhibits an exciton-like recombination behaviour similar to the neutral direct exciton (X_A), while the emission of trions (or charged exciton states) usually shows a superlinear power dependence. In this sense, the change of the PL emission, from with a superlinear to a linear power dependence, might indicate a transition from that the excitons binds with Fermi electrons (as trions) to that excitons interact with the collective excitation of Fermi electrons as loosely bound electron-hole pairs (exciton-plasmon).

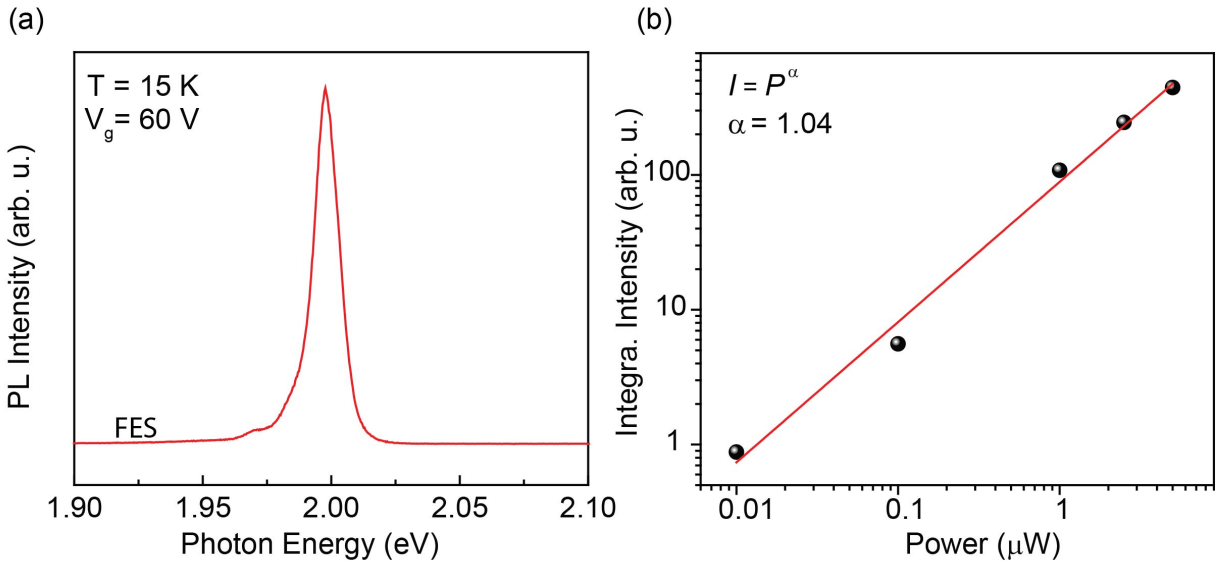

Figure 5.13: Power law of the Fermi edge singularity at $V_g = 60$ V. (a) The PL spectrum of the Fermi edge singularity. (b) The power law of Fermi edge singularity is fitted as 1.04, which reveals a linear exciton-like behaviour.

5.8 Conclusion

By fabricating a high-quality WS_2 monolayer device with ultra-narrow emission linewidth, we revolve fine structures of different charged exciton states, among which P_2 and P_3 are attributed to the charged indirect Λ-valley excitons. In addition, *via* electrostatic doping, we observe the evolution of PL spectra from a relatively neutral state to the Fermi edge singularity, where the existence of photoexcited electron-hole pairs changes from as charged states to exciton-plasmon quasiparticles. In a low-doping regime, the long range Coulomb potential from the Fermi gas is too weak to screen the Coulomb attraction among charged particles so that the charged states can exist. While above the Fermi edge singularity with a highly-dense Fermi gas, the strong long range Coulomb potential will screen the attraction of charge states and direct excitons, while the photoexcited electron-hole pairs interacts with the Fermi sea through intervalley short-range Coulomb potential. The Fermi edge singularity may indicate a transition from the fermion-like particles to boson-like particles, where it will be very interesting to study the interaction between photoexcited electron-hole pairs and highly-dense Fermi gas in the TMDs monolayers.

Chapter 6

Valley Zeeman Effect of Excitonic States in TMDs Monolayers

In group-VIB transition metal dichalcogenides (TMDs) monolayers, there are two inequivalent but energy-degenerate band edges in the K and $K^{'}$ valleys at the adjacent corners of the hexagonal Brillouin zone due to the broken inversion symmetry and time-reversal symmetry [5]. The valley index could be as a pseudospin, like the real spin, which gives rise to the valley-dependent optical selection rule [22, 116, 117] and valley Hall effect [118]. As a result, the valley pseudospin of TMDs monolayers enables the magnetic manipulation of their electronic band structures via the valley magnetic moment, leading to a valley Zeeman effect [119–121]. In this Chapter, by performing polarization-resolved magneto-photoluminescence measurements on the hBN-encapsulated WS_2 and MoS_2 monolayer, we reveal the observation of the valley Zeeman splitting and magnetic tuning of polarization for different charged valley excitons. The different magnetic response (valley Zeeman energy splitting) between WS_2 and MoS_2 monolayer arises from their distinct band configurations and valley magnetic moments of the electrons and holes that form the excitonic states. Therefore, by looking into the magnetic response of the excitonic states, we are able to access the information of their valley and spin properties. Our findings will advance the understanding of optical and electronic properties of TMDs monolayers in the magnetic field.

6.1 Magnetic-field-dependent and Polarization-resolved PL Spectra in WS_2 Monolayer

Figure 6.1 shows the PL spectrum with a 2 mW 532 nm excitation at 5 K, from which we can resolve three peaks. The triplet (T^-) and singlet (S^-) trion are resolved at 2.029 eV and 2.023 eV. The singlet-like charged indirect Λ-valley exciton (labeled by S^-_Λ) is resolved at 2.006 eV. Due to the high power excitation, the doping density is increased in the monolayer, leading to the enhancement of emission intensity from S^-_Λ, while its triplet-like counterpart could not be resolved.

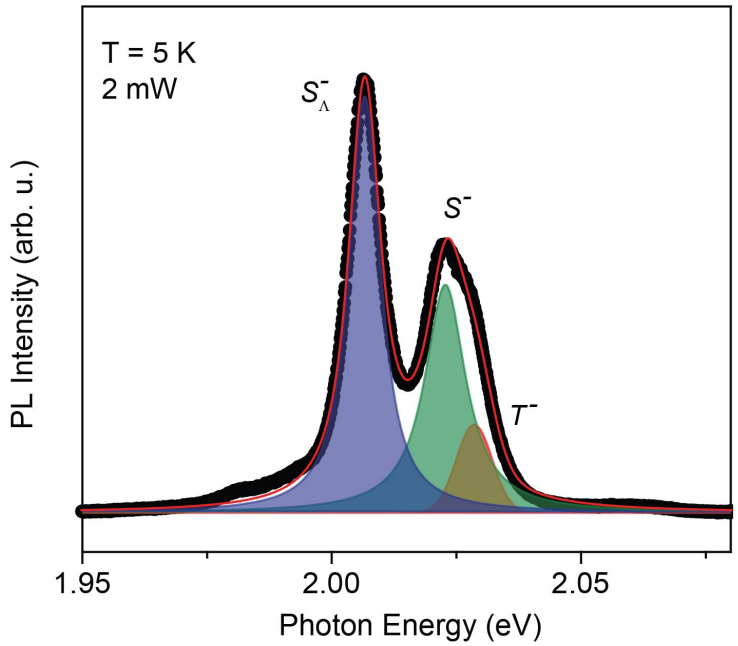

Figure 6.1: Photoluminescence spectrum of WS_2 monolayer with high excitation power. To enhance the intensity of charged indirect-Λ-valley exciton, a high power (2 mW) 532 nm excitation was used to excite the sample. The spectrum is best fitted with three Voigt functions. The energies of the triplet (T^-) and the singlet (S^-) trion are resolved at 2.029 eV and 2.023 eV. The singlet-like charged indirect Λ-valley exciton (S^-_Λ) is resolved at 2.006 eV, while its triplet-like counterpart could not be resolved with such high excitation.

By performing the polarization-resolved photoluminescence measurements with the high power excitation in a magnetic field perpendicular to the 2D plane of WS_2 monolayer, we investigated the valley Zeeman splitting and valley polarization for charged direct and indirect excitons.

Figure 6.2(a) shows the polarization-resolved PL spectra at selected magnetic field

strength. The spectra are taken with a σ^- excitation and detected with σ^- and σ^+, respectively. The spectra are best fitted with Voigt functions and the energy positions of T^-, S^- and S^-_Λ components are indicated by the arrows. With the increase of magnetic field B, the σ^- and σ^+ components are split, with σ^- shifting to higher energy and σ^+ shifting to lower energy relative to the zero field. Figure 6.2(b) shows the peak energies for T^-, S^- and S^-_Λ components as a function of magnetic field. The energy splitting for three components are extracted in Figure 6.2(c). The energy splitting could be fitted with a linear relationship given by

$$\Delta E = E_{\sigma^+} - E_{\sigma^-} = g_S \mu_B B, \tag{6.1}$$

where $\mu_B \approx 58$ μeV/T is the Bohr magneton and g_S is the spectroscopic g-factor of the emitting state [74]. From the fitting with the above equation, we obtain the g-factors as $g_S(T^-)$ = -3.7 $\pm$ 0.2, $g_S(S^-)$ = -3.8 $\pm$ 0.1, $g_S(S^-_\Lambda)$ = -3.6 $\pm$ 0.1. In the following we shall discuss the different components that contribute to the g_S-factors.

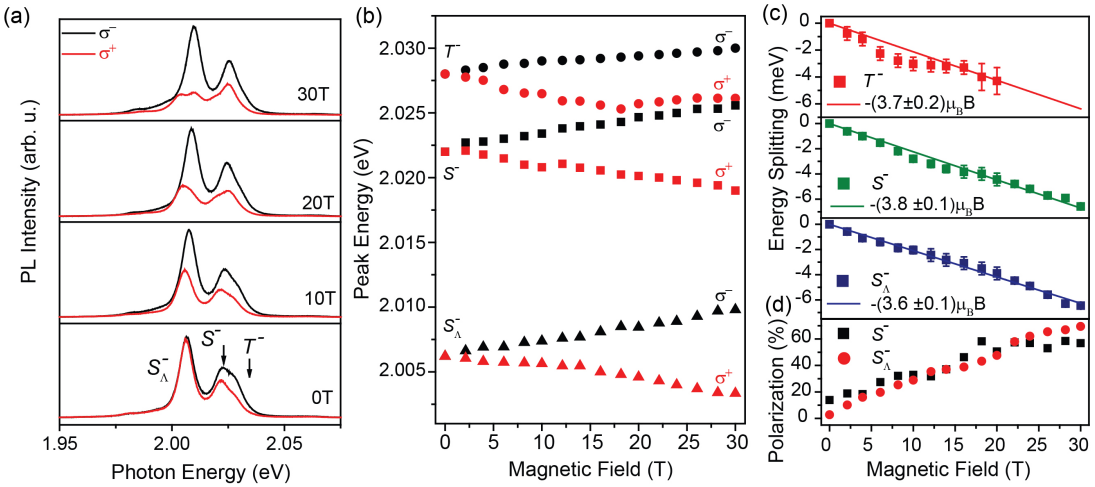

Figure 6.2: Valley Zeeman splitting and magnetic tuning of valley polarization for charged direct and indirect exciton states in WS_2 monolayer. Polarization-resolved PL spectra at selected magnetic field for σ^- detection and σ^+ detection. (b) Extracted peak energies for T^-, S^- and S^-_Λ components as a function of magnetic field. (c) Extracted energy splitting as a function of the magnetic field. The spectroscopic g_S factors are extracted from the linear fitting. (d) Valley polarization for S^- and S^-_Λ as a function of the magnetic field.

6.2 Valley Zeeman Splitting of Charged Valley Excitons

The magnetic moment of TMDs monolayers could be divided into two parts: (i) the bare magnetic moment ($g\mu_B\mathbf{S}$) that is linked to the real electron spin $\mathbf{S}$; (ii) the orbital magnetic moment [119, 120]. Furthermore, the orbital magnetic moment is composed of the valley magnetic moment from the lattice structure and the atomic orbital magnetic moment [119, 120]. The valley magnetic moment comes from the two inequivalent but energy-degenerate K and $K^{'}$ valleys, which have orbital contributions to the magnetic moment with equal magnitude but opposite direction due to the time-reversal symmetry [5, 119, 120].

A trion in TMDs monolayers is considered as a valley exciton plus an excess electron in the conduction band. Therefore, the magnetic moment of a trion will inherit the excitonic magnetic moment plus the contribution from the excess electron. Figure 6.3(a) shows the schematic diagram of valley Zeeman effect for a singlet S^- trion, from which we can explain the magnetic-field induced energy splitting of the S^- and T^- observed in Figure 6.2 and gain information about the orbital moments in different valleys. The dashed and solid lines represent the conduction and valence band edges without and with positive magnetic field B, with the blue and red denoting the spin up and down, respectively. To facilitate the clarification, we shall first discuss the magnetic moment of valley excitons and then the part from the excess electron in the lower-energy conduction band for WS_2 monolayer.

Since the interband transition conserves electron spins, the Zeeman shift of the band edges in the K and $K^{'}$ valley from the real spin ($\Delta_s = 2s_z\mu_B B$ denoted by black arrows) does not contribute to the energy splitting. Instead, the energy splitting arises from the combination of the magnetic moment from atomic d-orbitals in the band edges [122] and the valley magnetic moment. For the atomic orbital magnetic moment, the valence band edges mainly consist of d-orbital with m= 2 for K valley and -2 for $K^{'}$ valley, while the conduction band edges are mainly d-orbitals with m= 0 [119, 122]. Therefore, it leads to zero shift for the conduction band but a shift of $\Delta_a = 2\tau\mu_B B$ for the valence band edge where $\tau = \pm 1$ is the valley index for the K/$K^{'}$ valley.

The valley magnetic moment induced Zeeman shift is $\Delta_v = m_\tau B$ (denoted by green arrows) with $m_\tau = L_{z,j,i}\tau\mu_B$, where $L_{z,j,i}$ is the j-valley ($j = K, \Lambda$) g-factor for band i ($i = c, v$). The valley magnetic moments for electrons and holes are different due to their different effective masses [119, 120, 122], thus leading to a valley Zeeman shift in K

valley by $\tau\Delta L_{z,K}\mu_B B$, where $\Delta L_{z,K} = L_{z,K,c} - L_{z,K,v}$. Therefore, the valley-dependent linear shift of an exciton is given by $-\tau\Delta(B)/2$, where $\Delta(B) = 2(2 - \Delta L_{z,K})\mu_B B$ is the valley Zeeman splitting [119]. Then we consider the trion magnetic moment which includes a contribution from the excess electron. For a S^- trion as shown in Figure 6.3(a), the excess electron is located in the lower-energy conduction band that has the same valley index but opposite spin with the exciton part. It contributes an additional energy splitting in the magnetic field due to the orbit-valley coupling, with $g^{'}\mu_B B/2$, where $g^{'} = 2(L_{z,K,c} - 1)$. Since the excess electron has opposite spin and valley index for the S^- and T^-, their energy splitting, therefore, have opposite sign for $g^{'}$, which is given as,

$$\begin{aligned} \text{For } S^- \text{ state : } |\Delta E| &= \Delta(B) + g^{'}\mu_B B \\ &= [2(2 - (L_{z,K,c} - L_{z,K,v})) + 2|L_{z,K,c} - 1|]\mu_B B \end{aligned} \tag{6.2}$$

$$\begin{aligned} \text{For } T^- \text{ state : } |\Delta E| &= \Delta(B) - |g^{'}|\mu_B B \\ &= [2(2 - (L_{z,K,c} - L_{z,K,v})) - 2|L_{z,K,c} - 1|]\mu_B B \end{aligned} \tag{6.3}$$

The spectroscopic g-factor obtained in Figure 6.2(c), we get $|g_S|$ = 3.7 $\pm$ 0.2 for T^- and $|g_S|$ = 3.8 $\pm$ 0.1 for S^-. According to the two equations above, the K-valley g-factors for the conduction and valence band edges can be obtained with $|L_{z,K,c}|$ = 1.0 $\pm$ 0.1 and $|L_{z,K,v}|$ = 0.9 $\pm$ 0.1.

Similarly, the indirect-valley trion S^-_Λ experiences the valley Zeeman splitting but with the electron in the Λ band as shown in Figure 6.3(b). Since the conduction band edge at Λ is also mainly composed of d-orbitals with m = 0, its atomic magnetic moment is still zero [122], while only the Λ-valley g-factor for the conduction band should be replaced by $L_{z,\Lambda,c}$, thus giving rise to an energy splitting for S^-_Λ state by:

$$\begin{aligned} |\Delta E| &= \Delta(B) + |g^{'}|\mu_B B \\ &= [2(2 - (L_{z,\Lambda,c} - L_{z,K,v})) + 2|L_{z,K,c} - 1|]\mu_B B \end{aligned} \tag{6.4}$$

The $|g_S|$ for S^-_Λ is 3.6 $\pm$ 0.1, from which we can estimate Λ-valley g factor for the conduction band $|L_{z,\Lambda,c}|$ = 1.1 $\pm$ 0.3. In summary, the valley g-factors of the band edges in different valleys are given in Table 6.1.

Table 6.1: Valley g-factors of the band edges in different valleys for WS_2 monolayer

Valley g-factors	$L_{z,K,c}$	$L_{z,K,v}$	$L_{z,\Lambda,c}$
	1.0 ± 0.1	0.9 ± 0.1	1.1 ± 0.3

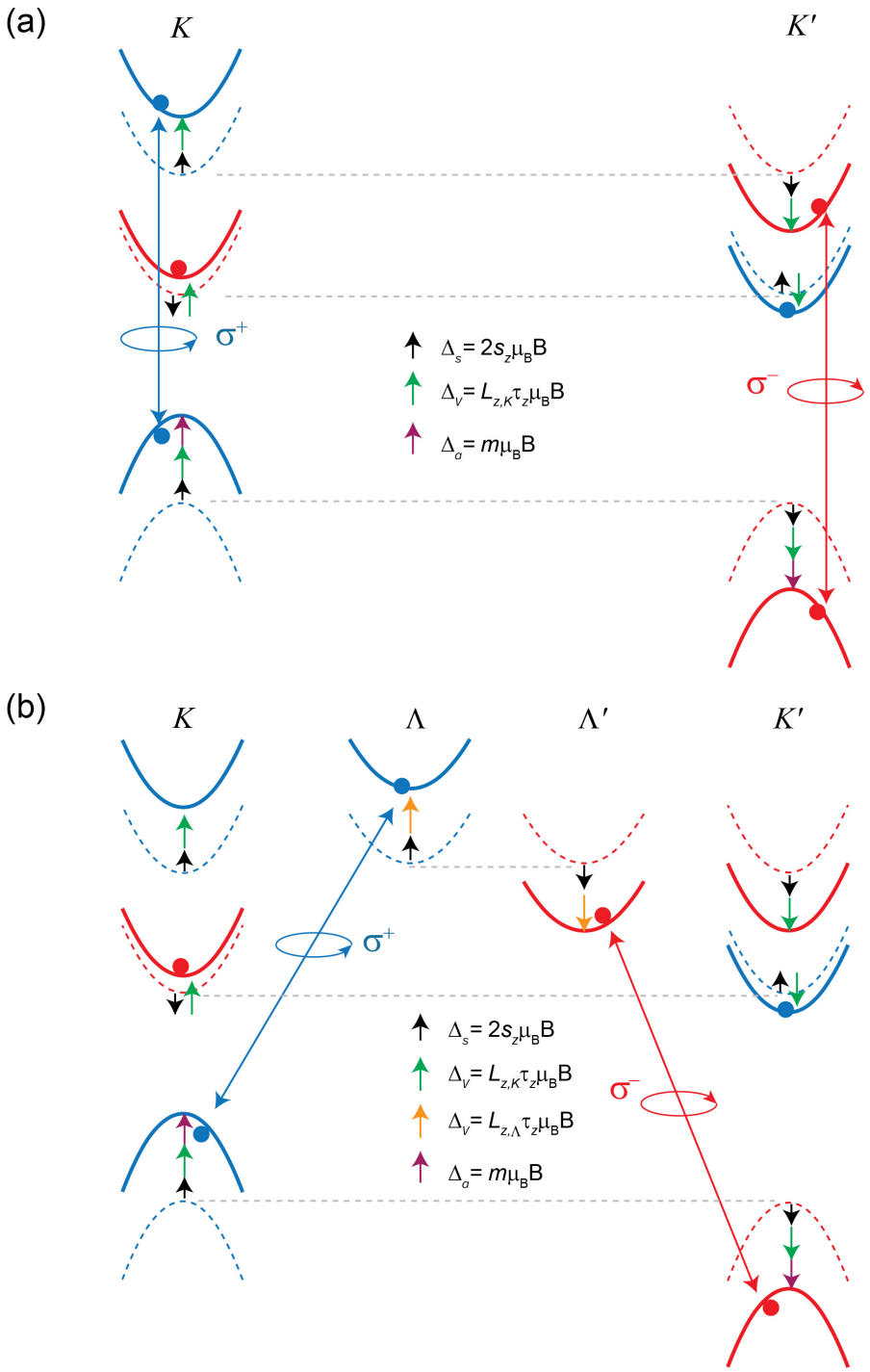

Figure 6.3: Valley Zeeman splitting for (a) charged direct excitons S^-, and for (b) charged indirect excitons S^-_Λ. The energy level diagrams show the different contributions to the valley Zeeman shifts (black arrows for spin magnetic moment, green for K valley magnetic moment, orange for Λ valley magnetic moment). Moreover, the magnetic moment of the valence band edges has a contribution from the atomic orbital with $m = 2$ (purple arrows), which has opposite sign in the K and K' valleys.

6.3 Magnetic Tuning of Valley Polarization for Charged Excitons in WS_2 Monolayer

In addition to the spectral splitting due to the increased magnetic field, an enhancement of valley polarization for S^- and S^-_Λ is also observed in Figure 6.2(d). A simple model could be used to explain this behaviour. Figure 6.4 shows the energy level diagram for a S^- state.

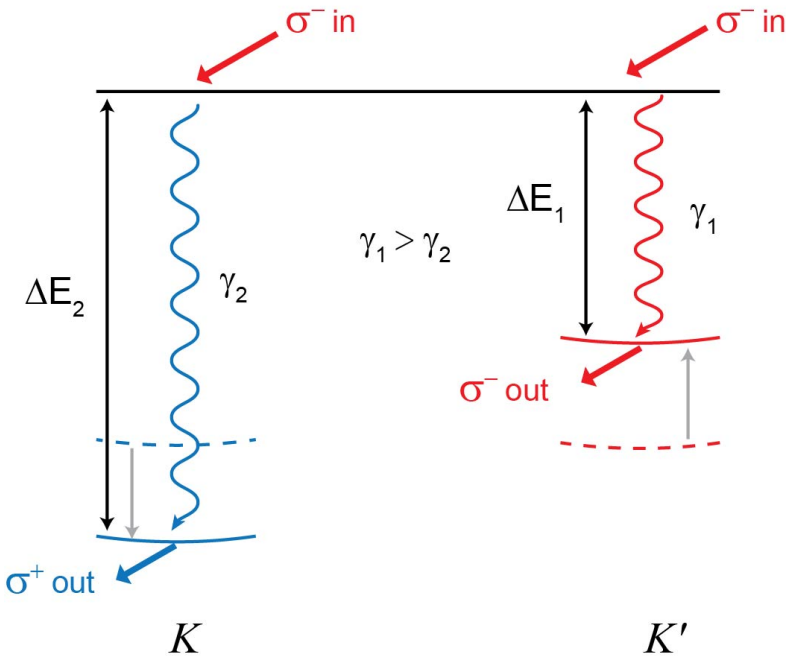

Figure 6.4: Magnetic tuning of valley polarization for charged excitons. The energy level diagrams show the band shifts of a singlet S^- trion due to the valley Zeeman effect. The solid (dashed) blue and red curves denote the band with (without) magnetic field for S^- state in K and $K^{'}$ valleys, respectively. The γ_1 and γ_2 denote the valley-conserving (the red wavy arrow) and valley-flipping relaxation rate (the blue wavy arrow), respectively. The grey arrows denote the valley Zeeman shifts of the bands. ΔE_1 and ΔE_2 represents the energy relaxation "path" for σ^- and σ^+ emission.

For the photoexcited carriers created by σ^- excitation, we define a valley-conserving relaxation rate γ_1 and a valley-flipping relaxation rate γ_2. Due to the stronger σ^- emission at zero-field, γ_1 is believed to be larger than γ_2. As the magnetic field increases, the induced valley Zeeman shift (grey arrows) lifts the energy degeneracy for the K and $K^{'}$ valley, with K-valley band lifting to higher energy (solid red curve) and $K^{'}$-valley band down to lower energy (solid blue curve). The energy relaxation "path" $\Delta E_1 = E_{exc} - E_{\sigma^-}$ decreases while $\Delta E_2 = E_{exc} - E_{\sigma^+}$ increases with the increase of the magnetic field.

Therefore, σ^- emission will become more efficient due to shorter relaxation path ΔE_1 as the magnetic field increases, leading to an enhanced valley polarization. The explanation could apply to the S_Λ^- as well.

6.4 Magnetic Brightening of Dark Excitons in MoS_2 Monolayer

Apart from the WS_2 monolayer, we also investigate the hBN-encapsulated MoS_2 monolayer as a comparison. Interestingly, the magnetic response of excitonic structures in MoS_2 monolayer shows some difference compared to WS_2 monolayer.

Figure 6.5 shows the PL mapping as a function of the magnetic field with the σ^- excitation and σ^- detection, from which the neutral exciton X_A and trion feature can be clearly observed. To resolve the detailed spectral components, the PL spectra at 0 T and 30 T are sorted out and best fitted with Voigt functions as shown in Figure 6.5(b). At 0 T, the spectrum shows three features: the neutral exciton X_A at 1.940 eV (red peak), a high-energy trion feature T^- at 1.920 eV (green peak) and a low-energy trion feature S^- at 1.907 eV (blue peak).

At cryogenic temperatures, electrons are relaxed in the conduction band minimum of either the spin-down state in the $K^{'}$ valley or the spin-up state in the K valley for MoS_2 monolayer [123, 124]. On the contrary with the WS_2 monolayer, the lower conduction band edges of MoS_2 monolayer have the same spin with the valence band edges at the K and $K^{'}$ valley, giving rise to the lower-energy bright exciton X_A [5, 7, 124]. The negatively charged trions are characterized based on the spin of the two electrons, leading to the intervalley singlet S^- and intravalley triplet trion T^- as shown in Figure 6.6 (a) and (b), respectively. The different phase space of the two extra electrons leads to different energies for two states. It is noted that the constituent electrons have identical valley and spin index only for T^- in MoX_2. Therefore, the repulsive exchange interaction between conduction band electrons is expected to be strongest for T^-, which may also explain the weak emission intensity of the T^- state in MoS_2 monolayer.

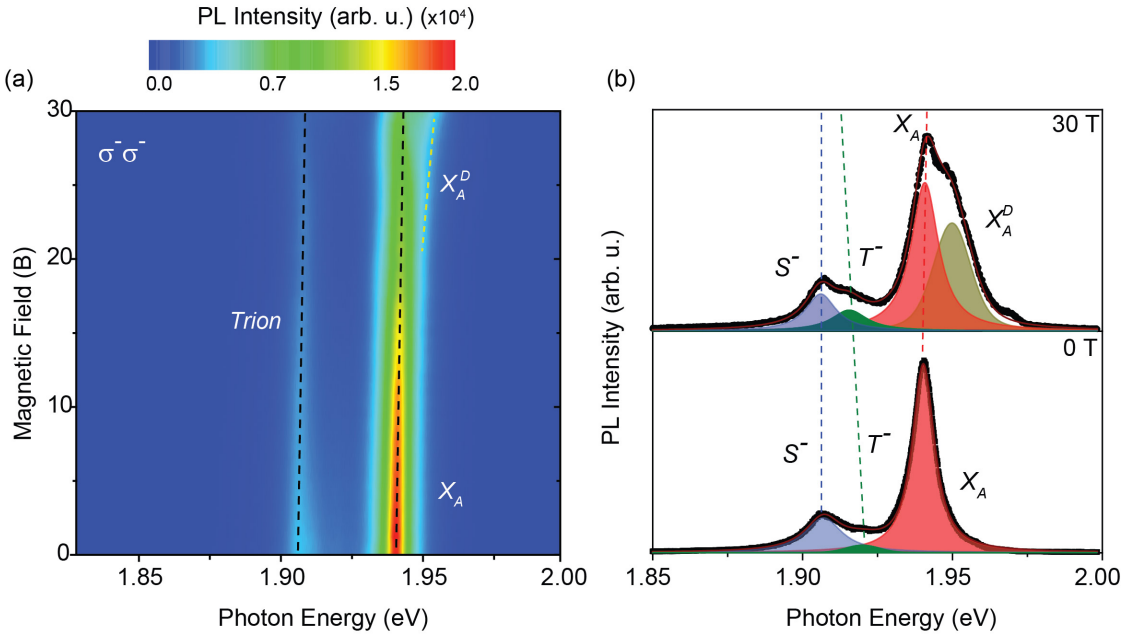

Figure 6.5: Magnetic-field-dependent PL spectra of MoS_2 monolayer. (a) PL mapping of MoS_2 monolayer at 5 K as a function of the magnetic field. The spectra are collected in a σ^-/σ^- configuration. (b) The spectra at 0 T and 30 T are best fitted with Voigt functions. Three features, namely neutral exciton X_A, higher-energy triplet trion T^- and lower-energy singlet trion S^-, are resolved at 0 T while an additional feature X_A^D appears at 30 T, which is attributed to the spin-forbidden dark exciton A.

When the magnetic field goes to 30 T, the X_A shows a clear blue-shift due to the valley Zeeman effect while the trions show slightly different trends. Interestingly, a new spectral feature arises at 1.949 eV when the field is above ∼20 T, indicating a new type of transition due to the strong magnetic field. Considering the band structure of MoS_2 monolayer as shown in Figure 6.6(c), this transition is attributed to the higher-energy spin-forbidden dark exciton. The reason is that, first, the calculated bright-dark splitting for A-exciton ground state due to the spin-split conduction band edge at K/K' valley is estimated to be few meV [7, 124], which matches with the energy difference of X_A and X_A^D (9 meV) in terms of order of magnitude. Secondly, it is possible that the strong magnetic field induces a brightening of the transition for dark state X_A^D. In principle, the spin-unlike transition is not allowed for an optically-bright transition. However, as reported in many studies, dark states are widely observed in the PL spectra of BN-encapsulated WSe_2 monolayer [90–97, 104]. The possible mechanism is that local disorders break the symmetry of the spin-unlike transition, thus making it get some oscillator strength and emit light. In a vivid picture as depicted in Figure 6.6(d), the strong magnetic field could also alter the symmetry of the transition for X_A^D. Under a

magnetic field that points up, the spin of the electron in the upper-conduction band could be gradually aligned towards the field with the increase of the field strength (noted that the spin direction of an electron is opposite to that of its surrounding magnetic field). As a result, a part of the electron spin will share the same direction with the hole spin, which increases the oscillator strength and turns the transition bright.

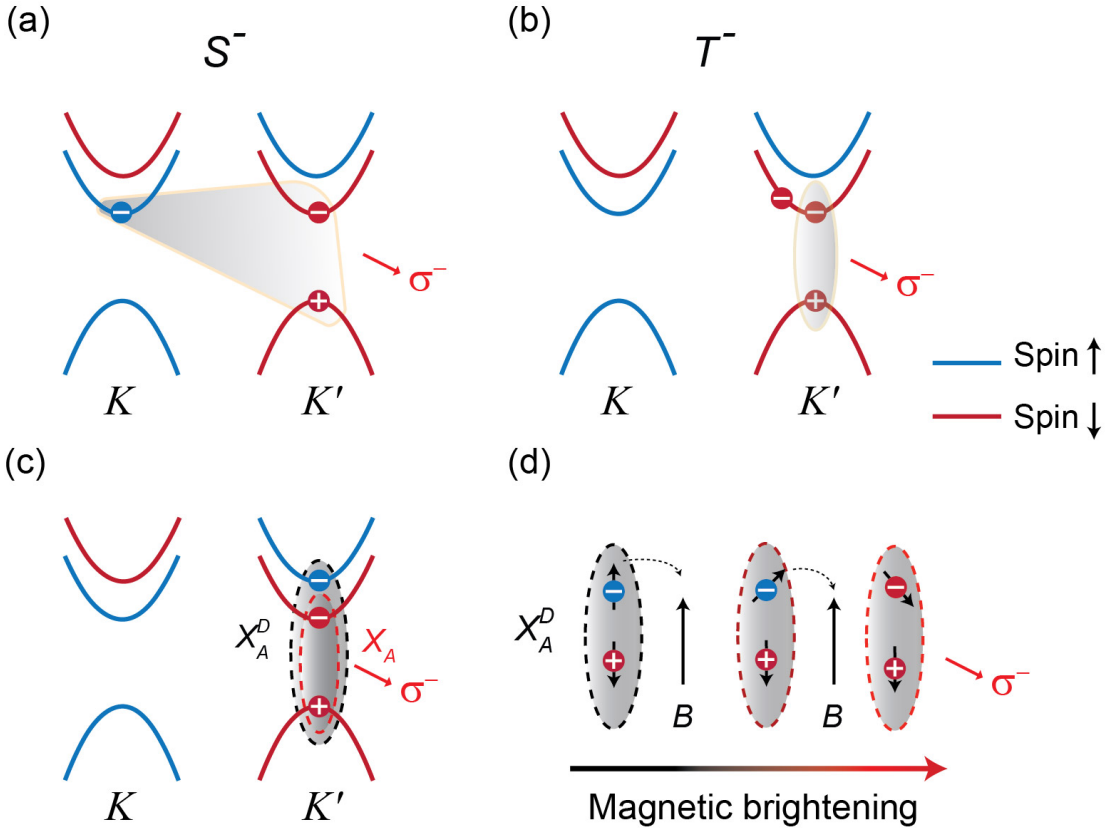

Figure 6.6: Spin and valley configurations of excitonic states in MoS_2 monolayer. (a) The singlet trion S^-. (b) The triplet trion T^-. (c) The bright exciton X_A and spin-forbidden dark exciton X_A^D. (d) The magnetic brightening of the X_A^D. The strong magnetic field could align the spin of the electron in the upper conduction band along the direction of the hole spin and turns the dark exciton bright.

On the contrary, X_A^D is not observed in σ^-/σ^+ configuration, as shown in Figure 6.7(b). Within the drawn scenario, it is understandable since the spin of the electron that X_A^D is composed of in the upper conduction band of the K valley is pointing down, which is already aligned along the magnetic field. Therefore, the magnetic field cannot turn the dark X_A^D state in the K valley bright.

6.5 Valley Zeeman Effect in MoS_2 Monolayer

In addition, we investigate the valley Zeeman effect in the hBN-encapsulated MoS_2 monolayer sample, as shown in Figure 6.7. The spectra in both σ^-/σ^- and σ^-/σ^+ configuration at different magnetic field are best fitted with Voigt functions, in which the energy shifts of different excitonic components are indicated by the colored-dashed lines. The peak energies of three excitonic states for σ^- and σ^+ components are extracted in Figure 6.7(c). Specifically, the magnetic field induced valley Zeeman splitting of the excitonic features are extracted from the fittings and given in Figure 6.7(d). By fitting the values with a linear equation, we get the spectroscopic g_S-factors with -(4.3$\pm$0.2) for X_A, -(2.9$\pm$0.2) for S^- and -(6.1$\pm$0.3) for T^-.

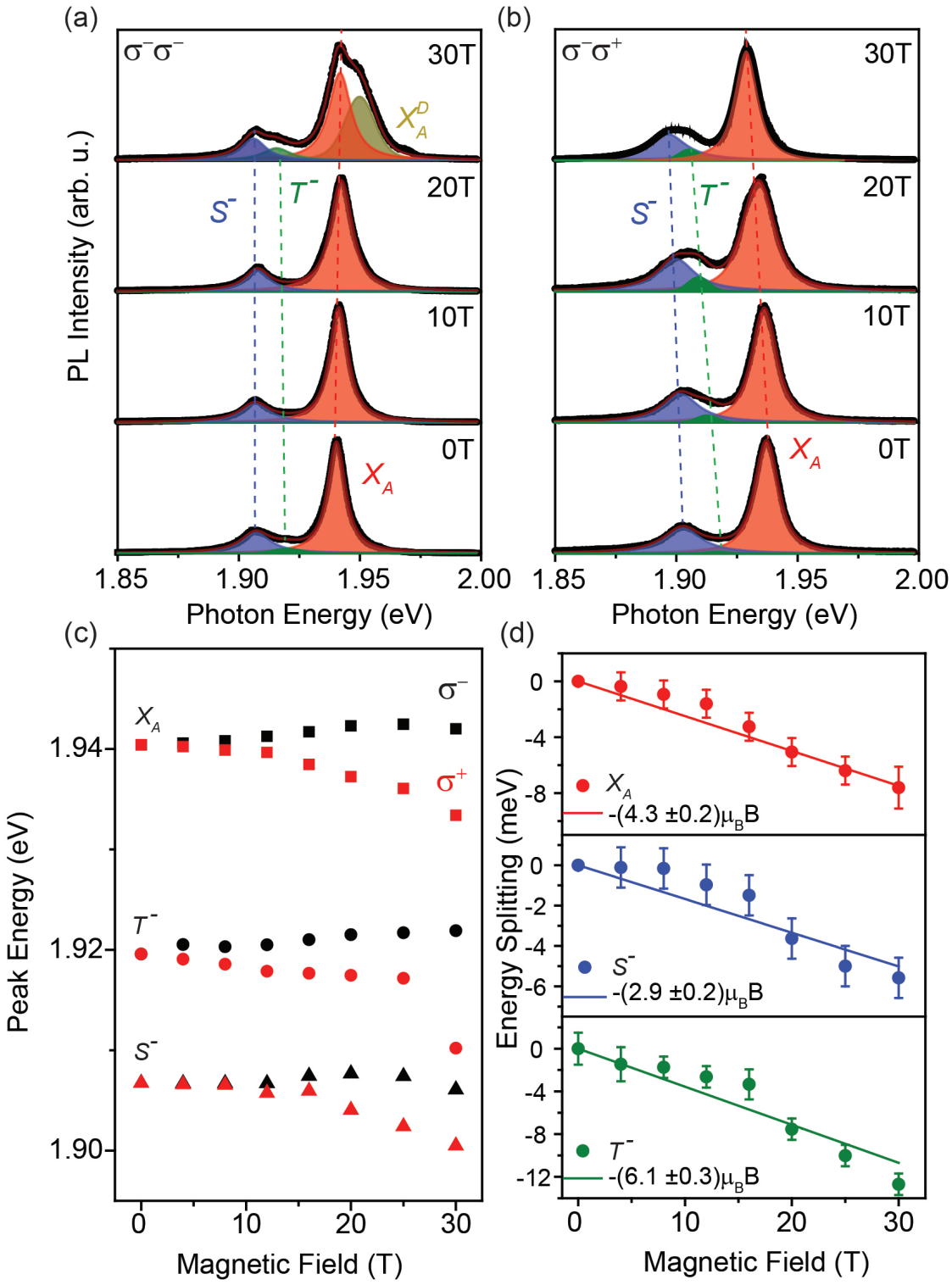

Figure 6.7: Valley Zeeman splitting of excitonic states in MoS_2 monolayer. PL spectra taken at different magnetic field strength with the configuration of σ^-/σ^- for (a) and σ^-/σ^+ for (b). (c) The extracted peak energies of three excitonic states for σ^- and σ^+ components. (d) The extracted energy splitting of the exciton and trions in MoS_2 monolayer as a function of the magnetic field.

As we discussed in the previous part for WS_2, the valley Zeeman splitting arises from three components: the electron spin induced magnetic moment ($g\mu_B \mathbf{S}$), valley magnetic

moment and the atomic orbital magnetic moment. Their associated g-factors contribute to the total spectroscopic g_S-factors obtained from the fitting results. By analyzing their possible combinations that determine the total g-factors, we are able to access the information of the individual components, especially the valley-related g-factors, which carries the essential information for the composition of the trion features. Figure 6.8 shows the schematic diagram of valley Zeeman splitting for a triplet trion T^-, from which we can write the total energy splitting of the trion states by considering the exciton valley Zeeman shift plus an electron contribution.

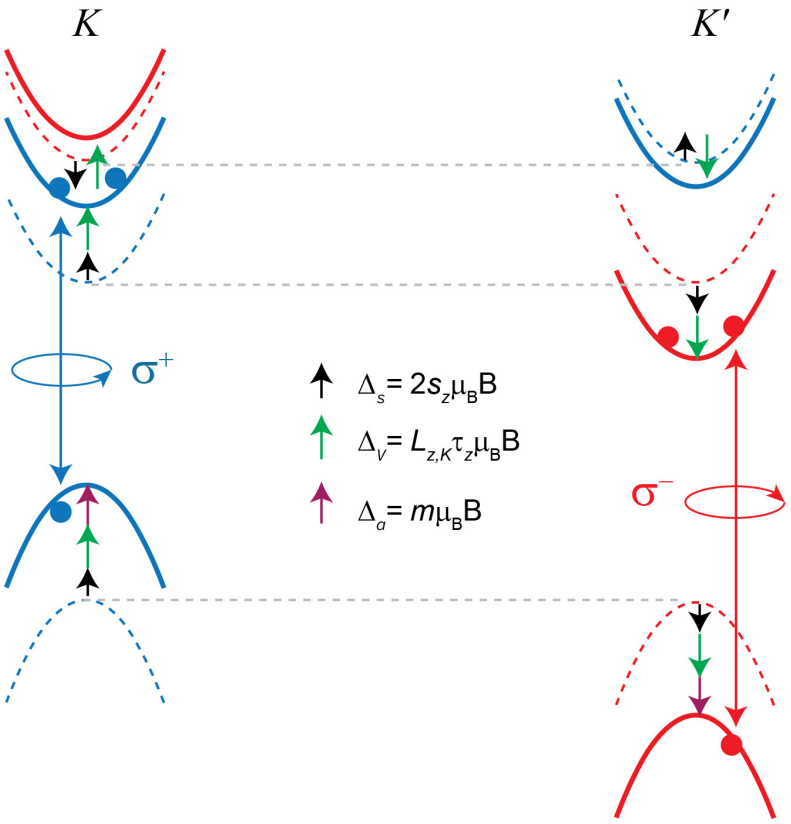

Figure 6.8: The schematic diagram of valley Zeeman effect for a triplet trion T^- in MoS_2 monolayer. The colored arrows indicate the different contributions to the total valley Zeeman shifts (black arrows for spin magnetic moment, green ones for K valley magnetic moment and purple ones for the atomic orbital magnetic moment with $m = 2$).

Since the additional electron that forms the T^- is assigned to be in the same valley of the exciton part, the valley Zeeman splitting for T^- is given by

$$\begin{aligned} |\Delta E| &= \Delta(B) + |g^{'}|\mu_B B \\ &= [2(2 - (L_{z,K,c} - L_{z,K,v})) + 2|L_{z,K,c} + 1|]\mu_B B \end{aligned} \tag{6.5}$$

For the S^- state, the extra electron is in the opposite valley to the exciton part. According

to the time-reversal symmetry, the energy splitting for S^- could be written as:

$$\begin{aligned} |\Delta E| &= \Delta(B) - |g^{'}|\mu_B B \\ &= [2(2 - (L_{z,K,c} - L_{z,K,v})) - 2|L_{z,K,c} + 1|]\mu_B B \end{aligned} \tag{6.6}$$

To evaluate the validity of the band configurations for T^- and S^-, we can associate the deduced total g-factors in Equation 6.5 and 6.6 with the experimentally obtained g_S-factors in Figure 6.7(d). Therefore, we get $|g(T^-)| = \Delta(B)/\mu_B B + |g^{'}| = 6.1 \pm 0.3$; $|g(S^-)| = \Delta(B)/\mu_B B - |g^{'}| = 2.9 \pm 0.2$. By solving two equations, we obtain the valley Zeeman splitting of exciton X_A by $g(X_A) = \Delta(B)/\mu_B B = 4.5 \pm 0.2$, which is equal to the spectroscopic g_S-factor value 4.3 $\pm$ 0.2 (see Figure 6.7(d)) within the reasonable error. The good agreement of the calculated $g(X_A)$ value with the spectroscopic value strongly suggests the validity of the assignment of band configurations for T^- and S^- as shown in Figure 6.6.

Similarly, we can further solve the Equation 6.5 and 6.6 so as to get the valley g-factors of the band edges at K/$K^{'}$ valley, which are extracted in Table 6.2.

Table 6.2: Valley g-factors of the band edges in different valleys for MoS_2 monolayer

Valley g-factors	$L_{z,K,c}$	$L_{z,K,v}$
	-0.2 $\pm$ 0.2	0.1 $\pm$ 0.1

By looking into the different magnetic response of excitonic states in WS_2 and MoS_2 monolayer, it is now clear to understand where the difference comes, that is, the different band configurations and valley magnetic moments of the constituent electrons and holes. The analysis we provide here could help us gain critical insights into the magnetic response of TMDs monolayers.

6.6 Conclusion

By performing polarization-resolved PL measurements on the hBN-encapsulated WS_2 and MoS_2 monolayer samples in the magnetic field up to 30 T, we observed the spectral energy splitting for different excitonic features. The energy splittings arise from different magnetic moment contributions including real spin magnetic moment, valley magnetic moment and atomic orbital magnetic moment. By analyzing their individual contributions to the total Zeeman-like energy shift, we extracted valley-dependent g-factors $L_{z,j,i}$ ($j = K, \Lambda, i = c, v$) for band edges in K and Λ (for WS_2 only) valleys. The difference of the magnetic response (valley Zeeman energy splitting) between WS_2 and MoS_2 monolayer arises from the different band configurations and valley magnetic moments of the electrons and holes that form the excitonic states. In turn, the magnetic response could help understand trion structures such as their compositions in terms of spin and valley configurations. Our results gain critical insights into the magneto-photoluminescence of different excitonic states especially trion species, leading towards a complete understanding of optical and electronic properties of TMDs monolayers in the magnetic field.

Chapter 7

Summary and Future Work

7.1 Summary

Recently, great efforts have been devoted to understand the optical properties of complex excitonic structures and many-body effects in TMDs monolayers. Particularly, the intrinsic PL spectrum of W-based monolayers (WS_2 and WSe_2) exhibit very rich features, while the lower-energy features still lack a full and complete understanding of their origins. Moreover, external techniques such as electrostatic doping and magnetic filed are often used to tune the excitonic structure and spin-valley properties, which helps gain insights into the unknown features. In this thesis:

(1). By using near-resonant excitation experiments, we have proved exciton-phonon scattering events with non-zero wavevector that provide strong evidences for the momentum-indirect nature of the optical bandgap in WS_2 monolayer. The scattering between carriers and zone-edge phonons creates excitons at different valleys, among which, the lowest-energy band is momentum-indirect. The low-energy emission features observed at low temperature could arise from momentum-indirect transitions. Our findings suggest the inherent bandgap nature of TMD monolayers could be indirect and highlight that more efforts are required for a complete understanding of the complex photoluminescence spectrum reported on W-based compounds.

(2). By fabricating a high-quality WS_2 monolayer device with ultra-narrow emission linewidth, we revolve lower-energy fine structures of charged exciton states, which are associated to the charged indirect Λ-valley excitons. In addition, via electrostatic doping, we observe the evolution of PL spectra from a relatively neutral state to the Fermi edge singularity, where the existence of photoexcited electron-hole pairs changes from as charged states to exciton-plasmon quasiparticles. In a low-doping regime, the long range Coulomb potential from the Fermi gas is too weak to screen the Coulomb attraction

among charged particles so that the charged states can exist. While above the Fermi edge singularity with a highly-dense Fermi gas, the strong long range Coulomb potential will screen the attraction of charge states and direct excitons, while the photoexcited electron-hole pairs interacts with the Fermi sea through intervalley short-range Coulomb potential. The Fermi edge singularity may indicate a transition from the fermion-like trions to exciton-plasmon quasiparticles.

(3). By performing the polarization-resolved PL measurements on the hBN-encapsulated WS_2 and MoS_2 monolayer samples in a magnetic field up to 30 T, we observed the spectral energy splitting for different excitonic complexes. The energy splittings arise from different magnetic moment contributions including real spin magnetic moment, valley magnetic moment and atomic orbital magnetic moment. By analyzing their individual contributions to the total Zeeman-like energy shift, we extracted valley-dependent g factors of band edges. In addition, the difference of the magnetic response (valley Zeeman energy splitting) between WS_2 and MoS_2 monolayer arises from the different band configurations and valley magnetic moments of the electrons and holes that form the excitonic states. Their different magnetic responses help us understand trion structures such as their compositions in terms of spin and valley configurations. Our results gain critical insights into the magneto-photoluminescence of different trion species in TMDs monolayers, leading towards a complete understanding of the optical and electronic properties of TMDs monolayers in the magnetic field.

7.2 Future Work

7.2.1 Excitons in a Highly Dense Fermi Gas

Our work has revealed how excitonic states evolve from trion states into another type of state which could be the exciton-plasmon quasiparticles as the Fermi electron density of the WS_2 monolayer increases. Besides, at a highly dense Fermi gas, the lattice structure could be strongly polarized, giving rise to the Fermi polarons. The different possibilities require further experiments to provide more evidence. After the photoexcitation, the photoexcited electron-hole pairs exhibit different behaviours compared to at the low doping regime. The spectroscopic techniques such as diffusion measurements allow us to optically study the interaction between photoexcited electron-hole pairs and the Fermi gas environment, which will provide further information on their coupling strength and so on. In addition, the Fermi polarons should be detected via angle-resolved photoemission spectroscopy (ARPES) as indicated in [9]. If combined with time, energy, momentum-resolved techniques [112], we shall be able to access information such as the formation and relaxation of photoexcited electron-hole pairs, their excited-state distribution and interaction with the Fermi gas and so on, which will provide more evidence for the origins of the complex excitonic states as we discuss in the thesis.

7.2.2 Moiré Excitons in Atomically-thin Hetero-/Homo- Bilayers via Magneto-Optical Photoluminescence

Atomically thin layers of group-VI transition metal dichalcogenides (TMDs) feature prominent exciton properties and spin-valley physics that make them ideal platforms for opto-valleytronic applications. However, limited by the picosecond timescale valley depolarization in monolayer TMDs, valley-functional optoelectronic application becomes difficult. Recently, the emergence of van der Waals (vdW) hetero-/homo-structures and lateral heterojunction between TMD monolayers provide a way to not only circumvent this limitation, but also enrich the valley-exciton physics. Interlayer excitons (IXs), formed from electrons and holes located in different layers have prolonged lifetime of nanoseconds due to the reduced overlapping of their wavefunctions. Although the intriguing valley properties can be translated to IXs, they can be controlled by the lattice mismatch and twisting angles between the constituent monolayers. At present,

the evolution of the valley- and spin-index changes and the formation of the Moiré minibands due to the Moiré potential remains poorly understood. Previous work as show strongly inverted valley polarization of IXs on the bilayers with controlled lattice mismatch and twisting angles, revealing the entire modification of spin-valley optical selection rules [125–127]. Therefore, we propose to investigate the characteristics of the exciton minibands, the valley-pseudospin- and spin-transfer of Moiré excitons by means of polarization-resolved photoluminescence measurements on twisted hetero-/homo-bilayers under a gate bias and in high magnetic fields. This complete set of experiments will provide a fundamental understanding of how twisted layers and the resulting Moiré patterns manipulate the electronic band-structure, spin- and valley-index in atomically-thin TMDs hetero-/homo-bilayers.

References

[1] M. Fox. *Optical properties of solids*. Oxford University Press, 2010, 2010.

[2] G. B. Liu, D. Xiao, Y. G. Yao, X. D. Xu, and W. Yao. Electronic structures and theoretical modelling of two-dimensional group-vib transition metal dichalcogenides. *Chem. Soc. Rev.*, 44(9):2643–2663, 2015.

[3] A. Splendiani, L. Sun, Y. B. Zhang, T. S. Li, J. Kim, C. Y. Chim, G. Galli, and F. Wang. Emerging photoluminescence in monolayer MoS_2. *Nano Lett.*, 10(4):1271–1275, 2010.

[4] K. F. Mak, C. G. Lee, J. Hone, J. Shan, and T. F. Heinz. Atomically thin MoS_2: a new direct-gap semiconductor. *Phys. Rev. Lett.*, 105(13):136805, 2010.

[5] D. Xiao, G. B. Liu, W. X. Feng, X. D. Xu, and W. Yao. Coupled spin and valley physics in monolayers of MoS_2 and other group-vi dichalcogenides. *Phys. Rev. Lett.*, 108(19):196802, 2012.

[6] A. Chernikov, T. C. Berkelbach, H. M. Hill, A. Rigosi, Y. L. Li, O. B. Aslan, D. R. Reichman, M. S. Hybertsen, and T. F. Heinz. Exciton binding energy and nonhydrogenic rydberg series in monolayer WS_2. *Phys. Rev. Lett.*, 113(7):076802, 2014.

[7] J.P. Echeverry, B. Urbaszek, T. Amand, X. Marie, and I.C. Gerber. Splitting between bright and dark excitons in transition metal dichalcogenide monolayers. *Phys. Rev. B*, 93(12):121107, 2016.

[8] J. S. Ross, S. F. Wu, H.Y. Yu, N. J. Ghimire, A. M. Jones, G. Aivazian, J. Q. Yan, D. G. Mandrus, D. Xiao, W. Yao, and X. D. Xu. Electrical control of neutral and charged excitons in a monolayer semiconductor. *Nat. Commun.*, 4:1474, 2013.

[9] M. G. Kang, S. W. Jung, W. J. Shin, Y. Sohn, S. H. Ryu, T. K. Kim, M. Hoesch, and K. S. Kim. Holstein polaron in a valley-degenerate two-dimensional semiconductor. *Nat. Mater.*, 17(8):676–680, 2018.

[10] J. M. Lu, O. Zheliuk, I. Leermakers, N. F. Q. Yuan, U. Zeitler, K. T. Law, and J. T. Ye. Evidence for two-dimensional ising superconductivity in gated MoS_2. *Science*, 350(6266):1353–1357, 2015.

[11] F. Cadiz, E. Courtade, C. Robert, G. Wang, Y. Shen, H. Cai, T. Taniguchi, K. Watanabe, H. Carrere, D. Lagarde, M. Manca, T. Amand, P. Renucci, S. Tongay, X. Marie, and B. Urbaszek. Excitonic linewidth approaching the homogeneous limit in MoS_2-based van der waals heterostructures. *Phys. Rev. X*, 7:021026, 2017.

[12] D. Kozawa, R. Kumar, A. Carvalho, K. K. Amara, W. J. Zhao, M. L. Wang, S. F.and Toh, R. M. Ribeiro, A. H. C. Neto, K. Matsuda, and G. Eda. Photocarrier relaxation pathway in two-dimensional semiconducting transition metal dichalcogenides. *Nat. Commun.*, 5(1):1–7, 2014.

[13] K. S. Novoselov and A. H. Castro Neto. Two-dimensional crystals-based heterostructures: materials with tailored properties. *Phys. Scr.*, 2012(T146):014006, 2012.

[14] A. Castellanos-Gomez, M. Buscema, R. Molenaar, V. Singh, L. Janssen, H. S. J. Van Der Zant, and G. A. Steele. Deterministic transfer of two-dimensional materials by all-dry viscoelastic stamping. *2D Materials*, 1(1):011002, 2014.

[15] Y. Hoshi, T. Kuroda, M. Okada, R. Moriya, S. Masubuchi, K. Watanabe, T. Taniguchi, R. Kitaura, and T. Machida. Suppression of exciton-exciton annihilation in tungsten disulfide monolayers encapsulated by hexagonal boron nitrides. *Phys. Rev. B*, 95(24):241403, 2017.

[16] Y. C. Cheng, Z. Y. Zhu, M. Tahir, and U. Schwingenschlögl. Spin-orbit–induced spin splittings in polar transition metal dichalcogenide monolayers. *EPL*, 102(5):57001, 2013.

[17] A. Kormányos, V. Zólyomi, N. D. Drummond, and G. Burkard. Spin-orbit coupling, quantum dots, and qubits in monolayer transition metal dichalcogenides. *Phys. Rev. X*, 4(1):011034, 2014.

[18] P. Y. Yu and M. Cardona. *Fundamentals of semiconductors: physics and materials properties*. Springer, 2010.

[19] A. H. Castro Neto, F. Guinea, N. M. R. Peres, K. S. Novoselov, and A. K. Geim. The electronic properties of graphene. *Rev. Mod. Phys*, 81:109–162, 2009.

[20] T. Jiang, H. R. Liu, D. Huang, S. Zhang, Y. G. Li, X. G. Gong, Y. R. Shen, W. T. Liu, and S. W. Wu. Valley and band structure engineering of folded MoS_2 bilayers. *Nat. Nanotechnol.*, 9(10):825–829, 2014.

[21] Z. Y. Zhu, Y. C. Cheng, and U. Schwingenschlögl. Giant spin-orbit-induced spin splitting in two-dimensional transition-metal dichalcogenide semiconductors. *Phys. Rev. B*, 84(15):153402, 2011.

[22] K. F. Mak, K. L. He, J. Shan, and T. F. Heinz. Control of valley polarization in monolayer MoS_2 by optical helicity. *Nat. Nanotechnol.*, 7(8):494, 2012.

[23] S. B. Nam, D. C. Reynolds, C. W. Litton, R. J. Almassy, T. C. Collins, and C. M. Wolfe. Free-exciton energy spectrum in GaAs. *Phys. Rev. B*, 13(2):761–767, 1976.

[24] X. X. Zhang, Y. M. You, S. Y. F. Zhao, and T. F. Heinz. Experimental evidence for dark excitons in monolayer WSe_2. *Phys. Rev. Lett.*, 115(25):257403, 2015.

[25] K. F. Mak, K. L. He, C.G. Lee, G. H. Lee, J. Hone, T. F. Heinz, and J. Shan. Tightly bound trions in monolayer MoS_2. *Nat. Mater.*, 12(3):207, 2013.

[26] G. Wang, I. C. Gerber, L. Bouet, D. Lagarde, A. Balocchi, M. Vidal, T. Amand, X. Marie, and B. Urbaszek. Exciton states in monolayer $MoSe_2$: impact on interband transitions. *2D Materials*, 2(4):045005, 2015.

[27] C. Ruppert, O. B. Aslan, and T. F. Heinz. Optical properties and band gap of single-and few-layer $MoTe_2$ crystals. *Nano Lett.*, 14(11):6231–6236, 2014.

[28] B. R. Zhu, X. Chen, and X. D. Cui. Exciton binding energy of monolayer WS_2. *Sci. Rep.*, 5:9218, 2015.

[29] G. Wang, X. Marie, I. Gerber, T. Amand, D. Lagarde, L. Bouet, M. Vidal, A. Balocchi, and B. Urbaszek. Giant enhancement of the optical second-harmonic emission of WSe_2 monolayers by laser excitation at exciton resonances. *Phys. Rev. Lett.*, 114(9):097403, 2015.

[30] K. S. Novoselov, A. K. Geim, S. V. Morozov, D. Jiang, Y. Zhang, S. V. Dubonos, I. V. Grigorieva, and A. A. Firsov. Electric field effect in atomically thin carbon films. *Science*, 306(5696):666–669, 2004.

[31] A. Ramasubramaniam. Large excitonic effects in monolayers of molybdenum and tungsten dichalcogenides. *Phys. Rev. B*, 86(11):115409, 2012.

[32] D. Y. Qiu, H. Felipe, and S. G. Louie. Optical spectrum of MoS_2: many-body effects and diversity of exciton states. *Phys. Rev. Lett.*, 111(21):216805, 2013.

[33] G. Berghäuser and E. Malic. Analytical approach to excitonic properties of MoS_2. *Phys. Rev. B*, 89(12):125309, 2014.

[34] K. L. He, N. Kumar, L. Zhao, Z. F. Wang, K. F. Mak, H. Zhao, and J. Shan. Tightly bound excitons in monolayer WSe_2. *Phys. Rev. Lett.*, 113(2):026803, 2014.

[35] M. M. Ugeda, A. J. Bradley, S. F. Shi, H. Felipe, Y. Zhang, D. Y. Qiu, W. Ruan, S. K. Mo, Z. Hussain, Z. X. Shen, F. Wang, Louie S. G., and M. F. Crommie. Giant bandgap renormalization and excitonic effects in a monolayer transition metal dichalcogenide semiconductor. *Nat. Mater.*, 13(12):1091, 2014.

[36] T. C. Berkelbach, M. S. Hybertsen, and D. R. Reichman. Theory of neutral and charged excitons in monolayer transition metal dichalcogenides. *Phys. Rev. B*, 88(4):045318, 2013.

[37] G. Plechinger, P. Nagler, J. Kraus, N. Paradiso, C. Strunk, C. Schüller, and T. Korn. Identification of excitons, trions and biexcitons in single-layer WS_2. *physica status solidi (RRL)*, 9(8):457–461, 2015.

[38] Y. M. You, X. X. Zhang, T. C. Berkelbach, M. S. Hybertsen, D. R. Reichman, and T. F. Heinz. Observation of biexcitons in monolayer WSe_2. *Nat. Phys.*, 11(6):477, 2015.

[39] A. Steinhoff, M. Florian, A. Singh, K. Tran, M. Kolarczik, S. Helmrich, A. W. Achtstein, U. Woggon, N. Owschimikow, F. Jahnke, and X. Q. Li. Biexciton fine structure in monolayer transition metal dichalcogenides. *Nat. Phys.*, 14(12):1199, 2018.

[40] X. D. Xu, W. Yao, D. Xiao, and T. F. Heinz. Spin and pseudospins in layered transition metal dichalcogenides. *Nat. Phys.*, 10(5):343, 2014.

[41] D. K. Zhang, D. W. Kidd, and K. Varga. Excited biexcitons in transition metal dichalcogenides. *Nano Lett.*, 15(10):7002–7005, 2015.

[42] M. Z. Mayers, T. C. Berkelbach, M. S. Hybertsen, and D. R. Reichman. Binding energies and spatial structures of small carrier complexes in monolayer transition-metal dichalcogenides via diffusion monte carlo. *Phys. Rev. B*, 92(16):161404, 2015.

[43] I. Kylänpää and H. P. Komsa. Binding energies of exciton complexes in transition metal dichalcogenide monolayers and effect of dielectric environment. *Phys. Rev. B*, 92(20):205418, 2015.

[44] M. Szyniszewski, E. Mostaani, N. D. Drummond, and V. I. Fal'Ko. Binding energies of trions and biexcitons in two-dimensional semiconductors from diffusion quantum monte carlo calculations. *Phys. Rev. B*, 95(8):081301, 2017.

[45] E. Mostaani, M. Szyniszewski, C. H. Price, R. Maezono, M. Danovich, R. J. Hunt, N. D. Drummond, and V. I. Fal'ko. Diffusion quantum monte carlo study of excitonic complexes in two-dimensional transition-metal dichalcogenides. *Phys. Rev. B*, 96(7):075431, 2017.

[46] M. Selig, G. Berghäuser, A. Raja, P. Nagler, C. Schüller, T. F. Heinz, T. Korn, A. Chernikov, E. Malic, and A. Knorr. Excitonic linewidth and coherence lifetime in monolayer transition metal dichalcogenides. *Nat. Commun.*, 7:13279, 2016.

[47] J. Lindlau, C. Robert, V. Funk, J. Förste, M. Förg, L. Colombier, A. Neumann, E. Courtade, S. Shree, T. Taniguchi, K. Watanabe, M. M. Glazov, X. Marie, B. Urbaszek, and A. Högele. Identifying optical signatures of momentum-dark excitons in transition metal dichalcogenide monolayers. *arXiv e-prints*, page arXiv:1710.00988, 2017.

[48] M. Feierabend, G. Berghäuser, A. Knorr, and E. Malic. Proposal for dark exciton based chemical sensors. *Nat. Commun.*, 8:14776, 2017.

[49] J. Lindlau, M. Selig, A. Neumann, L. Colombier, J. FÃűrste, V. Funk, M. FÃűrg, J. Kim, G. BerghÃďuser, T. Taniguchi, K. Watanabe, F. Wang, E. Malic, and A. HÃűgele. The role of momentum-dark excitons in the elementary optical response of bilayer WSe_2. *Nat. Commun.*, 9(1):2586, 2018.

[50] E. Malic, M. Selig, M. Feierabend, S. Brem, D. Christiansen, F. Wendler, A. Knorr, and G. Berghäuser. Dark excitons in transition metal dichalcogenides. *Phys. Rev. Mater.*, 2(1):014002, 2018.

[51] M. Selig, G. Berghäuser, M. Richter, R. Bratschitsch, A. Knorr, and E. Malic. Dark and bright exciton formation, thermalization, and photoluminescence in monolayer transition metal dichalcogenides. *2D Materials*, 5(3):035017, 2018.

[52] G. Berghäuser, P. Steinleitner, P. Merkl, R. Huber, A. Knorr, and E. Malic. Mapping of the dark exciton landscape in transition metal dichalcogenides. *Phys. Rev. B*, 98(2):020301, 2018.

[53] W. J. Zhao, Z. Ghorannevis, L. Q. Chu, M. L. Toh, C. Kloc, P. H. Tan, and G. Eda. Evolution of electronic structure in atomically thin sheets of WS_2 and WSe_2. *ACS Nano*, 7(1):791–797, 2012.

[54] A. Steinhoff, J.-H. Kim, F. Jahnke, M. RÃűsner, D.-S. Kim, C. Lee, G. H. Han, M. S. Jeong, T. O. Wehling, and C. Gies. Efficient excitonic photoluminescence in direct and indirect band gap monolayer MoS_2. *Nano Lett.*, 15(10):6841–6847, 2015.

[55] X. M. Dou, K. Ding, D. S. Jiang, X. F. Fan, and B. Q. Sun. Probing spin–orbit coupling and interlayer coupling in atomically thin molybdenum disulfide using hydrostatic pressure. *ACS Nano*, 10(1):1619–1624, 2016.

[56] Y. Y. Zhao, X. Luo, H. Li, J. Zhang, P. T. Araujo, C. K. Gan, J. Wu, H. Zhang, S. Y. Quek, M. S. Dresselhaus, and Q. H. Xiong. Interlayer breathing and shear modes in few-trilayer MoS_2 and WSe_2. *Nano Lett.*, 13(3):1007–1015, 2013.

[57] X. Luo, Y. Y. Zhao, J. Zhang, M. L. Toh, C. Kloc, Q. H. Xiong, and S. Y. Quek. Effects of lower symmetry and dimensionality on raman spectra in two-dimensional WSe_2. *Phys. Rev. B*, 88(19):195313, 2013.

[58] X. Lu, M. I. B. Utama, J. H. Lin, X. Luo, Y. Y. Zhao, J. Zhang, S. T. Pantelides, W. Zhou, S. Y. Quek, and Q. H. Xiong. Rapid and nondestructive identification of polytypism and stacking sequences in few-layer molybdenum diselenide by raman spectroscopy. *Adv. Mater.*, 27(30):4502–4508, 2015.

[59] A. Berkdemir, H. R. GutiÃľrrez, A. R. Botello-MÃľndez, N. Perea-LÃşpez, A. L. ElÃŋas, C. I. Chia, B. Wang, V. H. Crespi, F. LÃşpez-UrÃŋas, J. C. Charlier, H. Terrones, and M. Terrones. Identification of individual and few layers of WS_2 using raman spectroscopy. *Sci. Rep.*, 3:1755, 2013.

[60] E. del Corro, A. Botello-MÃľndez, Y. Gillet, A. L. Elias, H. Terrones, S. Feng, C. Fantini, Daniel Rhodes, N. Pradhan, L. Balicas, X. Gonze, J.-C. Charlier, M. Terrones, and M. A. Pimenta. Atypical exciton–phonon interactions in WS_2 and WSe_2 monolayers revealed by resonance raman spectroscopy. *Nano Lett.*, 16(4):2363–2368, 2016.

[61] M. R. Molas, K. Nogajewski, M. Potemski, and A. Babiński. Raman scattering excitation spectroscopy of monolayer WS_2. *Sci. Rep.*, 7(1):5036, 2017.

[62] A. Molina-Sanchez and L. Wirtz. Phonons in single-layer and few-layer MoS_2 and WS_2. *Phys. Rev. B*, 84(15):155413, 2011.

[63] C. Robert, D. Lagarde, F. Cadiz, G. Wang, B. Lassagne, T. Amand, A. Balocchi, P. Renucci, S. Tongay, B. Urbaszek, and X. Marie. Exciton radiative lifetime in transition metal dichalcogenide monolayers. *Phys. Rev. B*, 93(20):205423, 2016.

[64] G. Moody, C. Kavir Dass, K. Hao, C. H. Chen, L. J. Li, A. Singh, K. Tran, G. Clark, X. D. Xu, G. BerghÃďuser, E. Malic, A. Knorr, and X. Q. Li. Intrinsic homogeneous linewidth and broadening mechanisms of excitons in monolayer transition metal dichalcogenides. *Nat. Commun.*, 6:8315, 2015.

[65] M. Palummo, M. Bernardi, and J. C. Grossman. Exciton radiative lifetimes in two-dimensional transition metal dichalcogenides. *Nano Lett.*, 15(5):2794–2800, 2015.

[66] Z. H. Jin, X. D. Li, J. T. Mullen, and K. W. Kim. Intrinsic transport properties of electrons and holes in monolayer transition-metal dichalcogenides. *Phys. Rev. B*, 90(4):045422, 2014.

[67] F. A. Rasmussen and K. S. Thygesen. Computational 2d materials database: electronic structure of transition-metal dichalcogenides and oxides. *J. Phys. Chem. C*, 119(23):13169–13183, 2015.

[68] W. J. Zhao, R. M. Ribeiro, M. L. Toh, A. Carvalho, C. Kloc, A. H. Castro Neto, and G. Eda. Origin of indirect optical transitions in few-layer MoS_2, WS_2, and WSe_2. *Nano Lett.*, 13(11):5627–5634, 2013.

[69] B. R. Carvalho, Y. X. Wang, S. Mignuzzi, D. Roy, M. Terrones, C. Fantini, V. H. Crespi, L. M. Malard, and M. A. Pimenta. Intervalley scattering by acoustic phonons in two-dimensional MoS_2 revealed by double-resonance raman spectroscopy. *Nat. Commun.*, 8:14670, 2017.

[70] M. R. Molas, C. Faugeras, A. O. Slobodeniuk, K. Nogajewski, M. Bartos, D. M. Basko, and M. Potemski. Brightening of dark excitons in monolayers of semiconducting transition metal dichalcogenides. *2D Materials*, 4(2):021003, 2017.

[71] X. X. Zhang, T. Cao, Z. G. Lu, Y. C. Lin, F. Zhang, Y. Wang, Z. Q. Li, J. C. Hone, J. A. Robinson, D. Smirnov, S. G. Louie, and T. F. Heinz. Magnetic brightening and control of dark excitons in monolayer WSe_2. *Nat. Nanotechnol.*, 12(9):883, 2017.

[72] Y. Zhou, G. Scuri, D. S. Wild, A. A. High, A. Dibos, L. A. Jauregui, C. Shu, K. De Greve, K. Pistunova, A. Y. Joe, T. Taniguchi, K. Watanabe, P. Kim, M. D. Lukin, and H. K. Park. Probing dark excitons in atomically thin semiconductors via near-field coupling to surface plasmon polaritons. *Nat. Nanotechnol.*, 12(9):856, 2017.

[73] M. Koperski, M. R. Molas, A. Arora, K. Nogajewski, A. O. Slobodeniuk, C. Faugeras, and M. Potemski. Optical properties of atomically thin transition metal dichalcogenides: observations and puzzles. *Nanophotonics*, 6(6):1289–1308, 2017.

[74] P. Nagler, M. V. Ballottin, A. A. Mitioglu, M. V. Durnev, T. Taniguchi, K. Watanabe, A. Chernikov, C. Schüller, M. M. Glazov, P. C. M. Christianen, and T. Korn. Zeeman splitting and inverted polarization of biexciton emission in monolayer WS_2. *Phys. Rev. Lett.*, 121:057402, 2018.

[75] A. Srivastava, M. Sidler, A. V. Allain, D. S. Lembke, A. Kis, and A. Imamoğlu. Optically active quantum dots in monolayer WSe_2. *Nat. Nanotechnol.*, 10(6):491, 2015.

[76] M. Koperski, K. Nogajewski, A. Arora, V. Cherkez, P. Mallet, J.-Y. Veuillen, J. Marcus, P. Kossacki, and M. Potemski. Single photon emitters in exfoliated WSe_2 structures. *Nat. Nanotechnol.*, 10(6):503–506, 2015.

[77] Y. M. He, G. Clark, J. R. Schaibley, Y. He, M. C. Chen, Y. J. Wei, X. Ding, Q. Zhang, W. Yao, X. D. Xu, C. Y. Lu, and J. W. Pan. Single quantum emitters in monolayer semiconductors. *Nat. Nanotechnol.*, 10(6):497–502, 2015.

[78] H. N. Dery and Y. Song. Polarization analysis of excitons in monolayer and bilayer transition-metal dichalcogenides. *Phys. Rev. B*, 92:125431, 2015.

[79] A. Raja, A. Chaves, J. Yu, G. Arefe, H. M. Hill, A. F. Rigosi, T. C. Berkelbach, P. Nagler, C. SchÃijller, T. Korn, C. Nuckolls, J. Hone, L. E. Brus, T. F. Heinz, D. R. Reichman, and A. Chernikov. Coulomb engineering of the bandgap and excitons in two-dimensional materials. *Nat. Commun*, 8(1):1–7, 2017.

[80] N. N. Mao, Y. F. Chen, D. M. Liu, J. Zhang, and L. M. Xie. Solvatochromic effect on the photoluminescence of MoS_2 monolayers. *Small*, 9(8):1312–1315, 2013.

[81] D. Sercombe, S. Schwarz, O. Del Pozo-Zamudio, F. Liu, B. J. Robinson, E. A. Chekhovich, I. I. Tartakovskii, O. Kolosov, and A. I. Tartakovskii. Optical investigation of the natural electron doping in thin MoS_2 films deposited on dielectric substrates. *Sci. Rep.*, 3:3489, 2013.

[82] M. Buscema, G. A. Steele, H. S. J. van der Zant, and A. Castellanos-Gomez. The effect of the substrate on the raman and photoluminescence emission of single-layer MoS_2. *Nano Res.*, 7(4):561–571, 2014.

[83] N. Scheuschner, O. Ochedowski, A. M. Kaulitz, R. Gillen, M. Schleberger, and J. Maultzsch. Photoluminescence of freestanding single-and few-layer MoS_2. *Phys. Rev. B*, 89(12):125406, 2014.

[84] B. Chakraborty, A. Bera, D. V. S. Muthu, S. Bhowmick, U. V. Waghmare, and A. K. Sood. Symmetry-dependent phonon renormalization in monolayer MoS_2 transistor. *Phys. Rev. B*, 85(16):161403, 2012.

[85] J. H. Chen, C. Jang, S. D. Xiao, M. Ishigami, and M. S. Fuhrer. Intrinsic and extrinsic performance limits of graphene devices on SiO_2. *Nat. Nanotechnol*, 3(4):206, 2008.

[86] J. H. Seol, I. Jo, A. L. Moore, L. Lindsay, Z. H. Aitken, M. T. Pettes, X. S. Li, Z. Yao, R. Huang, D. Broido, N. Mingo, R. S. Ruoff, and L. Shi. Two-dimensional phonon transport in supported graphene. *Science*, 328(5975):213–216, 2010.

[87] B. Qiu and X. L. Ruan. Reduction of spectral phonon relaxation times from suspended to supported graphene. *Appl. Phys. Lett.*, 100(19):193101, 2012.

[88] J. C. Kim, D. R. Wake, and J. P. Wolfe. Thermodynamics of biexcitons in a gaas quantum well. *Phys. Rev. B*, 50(20):15099–15107, 1994.

[89] S. Sanguinetti, D. Colombo, M. Guzzi, E. Grilli, M. Gurioli, L. Seravalli, P. Frigeri, and S. Franchi. Carrier thermodynamics in InAs/$In_xGa_{1-x}As$ quantum dots. *Phys. Rev. B*, 74(20):205302, 2006.

[90] E. Liu, J. van Baren, Z. G. Lu, M. M. Altaiary, T. Taniguchi, K. Watanabe, D. Smirnov, and C. H. Lui. Gate tunable dark trions in monolayer WSe_2. *Phys. Rev. Lett.*, 123(2):027401, 2019.

[91] E. Liu, J. van Baren, T. Taniguchi, K. Watanabe, Y. C. Chang, and C. H. Lui. Valley-selective chiral phonon replicas of dark excitons and trions in monolayer WSe_2. *Phys. Rev. Res.*, 1(3):032007, 2019.

[92] M. H. He, P. Rivera, D. Van Tuan, N. P. Wilson, M. Yang, T. Taniguchi, K. Watanabe, J. Q. Yan, D. G. Mandrus, H. Y. Yu, H. Dery, W. Yao, and X. D. Xu. Valley phonons and exciton complexes in a monolayer semiconductor. *Nat. Commun.*, 11(1):1–7, 2020.

[93] Z. P. Li, T. M. Wang, Z. G. Lu, C. H. Jin, Y. W. Chen, Y. Z. Meng, Z. Lian, T. Taniguchi, K. Watanabe, S. B. Zhang, D. Smirnov, and S. F. Shi. Revealing the biexciton and trion-exciton complexes in bn encapsulated WSe_2. *Nat. Commun.*, 9(1):1–7, 2018.

[94] S. Y. Chen, T. Goldstein, T. Taniguchi, K. Watanabe, and J. Yan. Coulomb-bound four-and five-particle intervalley states in an atomically-thin semiconductor. *Nat. Commun.*, 9(1):1–8, 2018.

[95] M. Barbone, A. R. P. Montblanch, D. M. Kara, C. Palacios-Berraquero, A. R. Cadore, D. De Fazio, B. Pingault, E. Mostaani, H. Li, B. Chen, K. Watanabe,

T. Taniguchi, S. Tongay, G. Wang, A. C. Ferrari, and M. Atatüre. Charge-tuneable biexciton complexes in monolayer WSe_2. *Nat. Commun.*, 9(1):1–6, 2018.

[96] M. Paur, A. J. Molina-Mendoza, R. Bratschitsch, K. Watanabe, T. Taniguchi, and T. Mueller. Electroluminescence from multi-particle exciton complexes in transition metal dichalcogenide semiconductors. *Nat. Commun.*, 10(1):1–7, 2019.

[97] Z. P. Li, T. M. Wang, C. H. Jin, Z. G. Lu, Z. Lian, Y. Z. Meng, M. Blei, S. Y. Gao, T. Taniguchi, K. Watanabe, T. H. Ren, S. Tongay, L. Yang, D. Smirnov, T. Cao, and S. F. Shi. Emerging photoluminescence from the dark-exciton phonon replica in monolayer WSe_2. *Nat. Commun.*, 10(1):1–7, 2019.

[98] L. V. Keldysh. Coulomb interaction in thin semiconductor and semimetal films. *Soviet Journal of Experimental and Theoretical Physics Letters*, 29:658, 1979.

[99] W. T. Hsu, J. M. Quan, C. Y. Wang, L. S. Lu, M. Campbell, W. H. Chang, L. J. Li, X. Q. Li, and C. K. Shih. Dielectric impact on exciton binding energy and quasiparticle bandgap in monolayer WS_2 and WSe_2. *2D Materials*, 6(2):025028, 2019.

[100] H. Y. Yu, G. B. Liu, P. Gong, X. D. Xu, and W. Yao. Dirac cones and dirac saddle points of bright excitons in monolayer transition metal dichalcogenides. *Nat. Commun.*, 5(1):1–7, 2014.

[101] G. Plechinger, P. Nagler, A. Arora, R. Schmidt, A. Chernikov, A. G. Del Águila, P. C. M. Christianen, R. Bratschitsch, C. Schüller, and T. Korn. Trion fine structure and coupled spin–valley dynamics in monolayer tungsten disulfide. *Nat. Commun.*, 7(1):1–9, 2016.

[102] D. Vaclavkova, J. Wyzula, K. Nogajewski, M. Bartos, A. O. Slobodeniuk, C. Faugeras, M. Potemski, and M. R. Molas. Singlet and triplet trions in WS_2 monolayer encapsulated in hexagonal boron nitride. *Nanotechnology*, 29(32):325705, 2018.

[103] E. Liu, J. van Baren, C. T. Liang, T. Taniguchi, K. Watanabe, N. M. Gabor, Y. C. Chang, and C. H. Lui. Multipath optical recombination of intervalley dark excitons and trions in monolayer WSe_2. *Phys. Rev. Lett.*, 124(19):196802, 2020.

[104] Z. L. Ye, L. Waldecker, E. Y Ma, D. Rhodes, A. Antony, B. Kim, X. X. Zhang, M. D. Deng, Y. X. Jiang, Z. G. Lu, D. Smirnov, K. Watanabe, T. Taniguchi, J. Hone, and T. F. Heinz. Efficient generation of neutral and charged biexcitons in encapsulated WSe_2 monolayers. *Nat. Commun.*, 9(1):1–6, 2018.

[105] A. Chernikov, A. M. Van Der Zande, H. M. Hill, A. F. Rigosi, A. Velauthapillai, J. Hone, and T. F. Heinz. Electrical tuning of exciton binding energies in monolayer WS_2. *Phys. Rev. Lett.*, 115(12):126802, 2015.

[106] P. Hawrylak. Optical properties of a two-dimensional electron gas: Evolution of spectra from excitons to fermi-edge singularities. *Phys. Rev. B*, 44(8):3821, 1991.

[107] S. A. Brown, Jeff F. Young, J. A. Brum, P. Hawrylak, and Z. Wasilewski. Evolution of the interband absorption threshold with the density of a two-dimensional electron gas. *Phys. Rev. B*, 54(16):R11082–R11085, 1996.

[108] V. Huard, R. T. Cox, K. Saminadayar, A. Arnoult, and S. Tatarenko. Bound states in optical absorption of semiconductor quantum wells containing a two-dimensional electron gas. *Phys. Rev. Lett.*, 84(1):187–190, 2000.

[109] A. A. Mitioglu, P. Plochocka, J. N. Jadczak, W. Escoffier, G. L. J. A. Rikken, L. Kulyuk, and D. K. Maude. Optical manipulation of the exciton charge state in single-layer tungsten disulfide. *Phys. Rev. B*, 88(24):245403, 2013.

[110] S. Brem, A. Ekman, D. Christiansen, F. Katsch, M. Selig, C. Robert, X. Marie, B. Urbaszek, A. Knorr, and E. Malic. Phonon-assisted photoluminescence from indirect excitons in monolayers of transition-metal dichalcogenides. *Nano Lett.*, 20(4):2849–2856, 2020.

[111] D. Bao, A. G. del Águila, T. H. Do, S. Liu, J. J. Pei, and Q. H. Xiong. Probing momentum-indirect excitons by near-resonance photoluminescence excitation spectroscopy in WS_2 monolayer. *2D Materials*, 2020.

[112] J. Madéo, M. K. L. Man, C. Sahoo, M. Campbell, V. Pareek, E. L. Wong, A. Al-Mahboob, N. S. Chan, A. Karmakar, B. M. K. Mariserla, X. Q. Li, T. F. Heinz, T. Cao, and K. M. Dani. Directly visualizing the momentum-forbidden dark excitons and their dynamics in atomically thin semiconductors. *Science*, 370(6521):1199–1204, 2020.

[113] H. Dery. Theory of intervalley coulomb interactions in monolayer transition-metal dichalcogenides. *Phys. Rev. B*, 94(7):075421, 2016.

[114] D. Van Tuan, B. Scharf, I. Žutić, and H. Dery. Marrying excitons and plasmons in monolayer transition-metal dichalcogenides. *Phys. Rev. X*, 7(4):041040, 2017.

[115] D. Pines. Collective energy losses in solids. *Rev. Mod. Phys.*, 28(3):184, 1956.

[116] H. L. Zeng, J. F. Dai, W. Yao, D. Xiao, and X. D. Cui. Valley polarization in MoS_2 monolayers by optical pumping. *Nat. Nanotechnol.*, 7(8):490, 2012.

[117] T. Cao, G. Wang, W. P. Han, H. Q. Ye, C. R. Zhu, J. R. Shi, Q. Niu, P. H. Tan, E. g. Wang, B. L. Liu, and F. Ji. Valley-selective circular dichroism of monolayer molybdenum disulphide. *Nat. Commun.*, 3:887, 2012.

[118] K. F. Mak, K. L. McGill, J. Park, and P. L. McEuen. The valley hall effect in MoS_2 transistors. *Science*, 344(6191):1489–1492, 2014.

[119] G. Aivazian, Z. R. Gong, A. M. Jones, R. L. Chu, J. Q. Yan, D. G. Mandrus, C. W. Zhang, D. Cobden, W. Yao, and X. D. Xu. Magnetic control of valley pseudospin in monolayer WSe_2. *Nat. Phys.*, 11(2):148–152, 2015.

[120] A. Srivastava, M. Sidler, A. V. Allain, D. S. Lembke, A. Kis, and A. ImamoÄ§lu. Valley zeeman effect in elementary optical excitations of monolayer WSe_2. *Nat. Phys.*, 11(2):141–147, 2015.

[121] D. MacNeill, C. Heikes, K. F. Mak, Z. Anderson, A. Kormányos, V. Zólyomi, J. Park, and D. C. Ralph. Breaking of valley degeneracy by magnetic field in monolayer $MoSe_2$. *Phys. Rev. Lett.*, 114(3):037401, 2015.

[122] G. B. Liu, W. Y. Shan, Y. G. Yao, W. Yao, and D. Xiao. Three-band tight-binding model for monolayers of group-vib transition metal dichalcogenides. *Phys. Rev. B*, 88(8):085433, 2013.

[123] R. Tempelaar and T. C. Berkelbach. Many-body simulation of two-dimensional electronic spectroscopy of excitons and trions in monolayer transition metal dichalcogenides. *Nat. Commun.*, 10(1):1–7, 2019.

[124] J. G. Roch, G. Froehlicher, N. Leisgang, P. Makk, K. Watanabe, T. Taniguchi, and R. J. Warburton. Spin-polarized electrons in monolayer MoS_2. *Nat. Nano.*, 14(5):432–436, 2019.

[125] A. K. Geim and I. V. Grigorieva. Van der waals heterostructures. *Nature*, 499(7459):419–425, 2013.

[126] W. T. Hsu, L. S. Lu, P. H. Wu, M. H. Lee, P. J. Chen, P. Y. Wu, Y. C. Chou, H. T. Jeng, L. J. Li, M. W. Chu, and W. H. Chang. Negative circular polarization emissions from $WSe_2/MoSe_2$ commensurate heterobilayers. *Nat. Commun.*, 9(1):1–7, 2018.

[127] C. H. Jin, E. C. Regan, A. M. Yan, M. I. B. Utama, D. Q. Wang, S. H. Zhao, Y. Qin, S. J. Yang, Z. R. Zheng, S. Y. Shi, K. Watanabe, T. Taniguchi, S. Tongay, A. Zettl, and F. Wang. Observation of moiré excitons in WSe_2/WS_2 heterostructure superlattices. *Nature*, 567(7746):76–80, 2019.

List of Publications

1, Di Bao*, Andrés Granados del Águila*, T. Thu Ha Do, Sheng Liu, Jiajie Pei, and Qihua Xiong. "Probing momentum-indirect excitons by near-resonance photoluminescence excitation spectroscopy in WS_2 monolayer." **2D Materials 7.3** (2020): 031002.

2, Wang, Jun, Rui Su, Jun Xing, **Di Bao,** Carole Diederichs, Sheng Liu, Timothy CH Liew, Zhanghai Chen, and Qihua Xiong. "Room temperature coherently coupled exciton-polaritons in two-dimensional organic-inorganic perovskite." **ACS nano 12.8** (2018): 8382-8389.